Charles University in Prague
Faculty of Mathematics and Physics

DOCTORAL THESIS

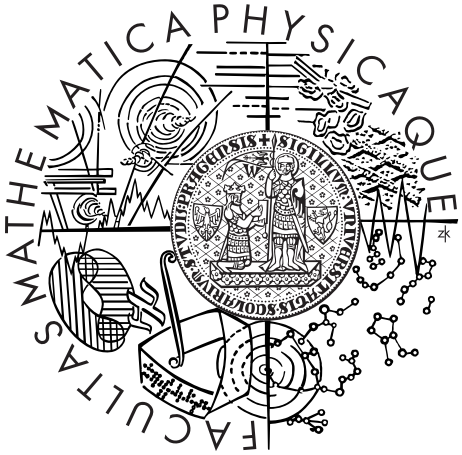

Vojtěch Pleskot

Measurement of the inclusive jet cross-section with the ATLAS detector

Institute of Particle and Nuclear Physics

Supervisor of the doctoral thesis: Doc. RNDr. Tomáš Davídek, PhD.
Study programme: Physics
Specialization: Subnuclear physics

Prague 2015

I would like to thank a lot my excellent supervisor Tomáš Davídek for his guidance and for his helpful attitude. He introduced me to the experimental particle physics and to the software tools used in the field, especially Linux and ROOT. He also introduced me to the Tile Calorimeter working group and explained to me many things related to this detector. He was always ready to help me with various aspects of my work. I appreciate his diligence and thoroughness.

I am very grateful to my precious collegue Esteban Fullana with whom I worked on the ATLAS inclusive jet cross-section measurement. His fantastic guidance included long hours of discussions about the measurement, physics, software tools and numerous technical aspects. He also helped me a lot with my qualification task for the ATLAS authorship. I appreciate his helpfulness, kindness, patience and endless support.

I would also like to thank Chris Meyer who gave me a lot of code for the inclusive jet cross-section measurement. He also passed me much experimental know-how. I thank my CERN collegues Shima Shimizu, Bogdan Malaescu, Pavel Starovoitov, Tancredi Carli, Eugen Ertel and Alexander Solodkov for fruitfull collaboration and discussions on various topics. I would like to thank Rupert Leitner, Jiří Dolejší, Jiří Hořejší, Michal Malinský, Pavel Cejnar, Alexander Kupčo, Martin Spousta and Oldřich Kepka for very interesting discussions about physics. I am grateful to my schoolmates and friends Jana Faltová, Martin Rybář, Radek Žlebčík, Daniel Scheirich, Pavel Řezníček and Zbyněk Drásal for their versatile help.

Last but not least I must thank my parents and my wife for their fantastic universal support without which I would not be able to study physics. I am extremely grateful to them.

I declare that I carried out this doctoral thesis independently, and only with the cited sources, literature and other professional sources.

I understand that my work relates to the rights and obligations under the Act No. 121/2000 Coll., the Copyright Act, as amended, in particular the fact that the Charles University in Prague has the right to conclude a license agreement on the use of this work as a school work pursuant to Section 60 paragraph 1 of the Copyright Act.

In Prague, 20th April 2015 Vojtěch Pleskot

Název práce: Měření účinného průřezu inkluzivní produkce jetů detektorem ATLAS

Autor: Vojtěch Pleskot

Katedra: Ústav částicové a jaderné fyziky (ÚČJF)

Vedoucí dizertační práce: Doc. RNDr. Tomáš Davídek, PhD., ÚČJF

Email vedoucího: davidek@ipnp.troja.mff.cuni.cz

Abstrakt: LHC je urychlovač částic postavený v Evropské organizaci pro jaderný výzkum (CERN). Urychluje protony na nejvyšší člověkem dosažené energie. Experiment ATLAS zaznamenává data o srážkách těchto protonů. V nich často vznikají jety neboli kolimované výtrysky hadronů. Tato dizertační práce představuje nejnovější měření účinného průřezu inkluzivní produkce jetů experimentem ATLAS. Použitá data byla nabrána v roce 2011 ve srážkách protonů o těžišťové energii 7 TeV. Kalorimetr je pro rekonstrukci jetů nejdůležitější částí detektoru ATLAS. V průběhu nabírání dat bylo kvůli problémům odstaveno několik částí (modulů) hadronového kalorimetru. Tyto nefunkční moduly mají značný dopad na měření energie jetů. Dizertační práce popisuje testy dvou různých druhů softwarových korekcí k energii jetů ovlivněných tímto problémem.

Klíčová slova: ATLAS, jet, QCD, účinný průřez, hadronový kalorimetr

Title: Measurement of the inclusive jet cross-section with the ATLAS detector

Author: Vojtěch Pleskot

Department: Institute of Particle and Nuclear Physics (IPNP)

Supervisor: Doc. RNDr. Tomáš Davídek, PhD., IPNP

Supervisor's e-mail address: davidek@ipnp.troja.mff.cuni.cz

Abstract: The Large Hadron Collider is an accelerator based in the European Organization for Nuclear Research (CERN). It accelerates protons to the highest energies ever reached by the mankind. The ATLAS experiment records data from the proton-proton collisions. Common objects born in the collisions are jets, i.e. collimated bursts of hadrons. This thesis presents the newest ATLAS measurement of the inclusive jet cross-section. The data sample used was recorded in 2011 at 7 TeV centre-of-mass energy. Calorimeter is the most important part of ATLAS for the jet reconstruction. During the data taking, the hadronic calorimeter faced several failures of its components, modules. These non-operating parts have important impact on the jet energy measurement. The thesis describes tests of two available software corrections of the affected jet energies.

Keywords: ATLAS, jet, QCD, cross-section, hadronic calorimeter

Contents

Introduction

This thesis is based on data recorded in 2011 by the ATLAS experiment at the Large Hadron Collider (LHC) built in the European Organization for Nuclear Research (CERN). LHC is proton-proton accelerator. It is designed to accelerate protons up to the energy of 7 TeV and make them collide at 14 TeV of centre-of-mass energy. The designed instantaneous luminosity is 10^{34} cm^{-2} s^{-1} [1].

The main part of this thesis describes the author's contribution to the inclusive jet cross-section measurement in proton-proton collisions at 7 TeV centre-of-mass energy. Jets are collimated "rays" of particles (mainly hadrons) originating from fragmentation of high-energetic partons (quarks, gluons) produced in the collisions. Since the strong interaction is responsible for the production and fragmentation of partons the theory that aims to describe those effects is quantum chromodynamics (QCD).[1] Therefore, the inclusive jet cross-section measurement provides a test of QCD. The measurement can also be used to constrain parton distribution functions (PDFs) of proton.

The ATLAS detector is divided into several subsystems, each of them is used for the detection of different types of particles. The purpose of the hadronic calorimeter is to absorb hadrons and to measure their energy. Therefore, it is very important part of ATLAS for the jet measurements. But no device is always fully working. In 2011 several pieces (modules) of the hadronic calorimeter were non-operational. The energies of jets affected by the modules are corrected at the software level. There are two available correction procedures. A part of this thesis describes a test of their performance.

ATLAS is a huge collaboration with more than 3000 people. The work is split among specialized groups. Some of them take care about the hardware, its checks and maintenance. Others study the detector performance on physics objects. Dedicated groups focus on physics measurements and analyses. Within the groups, people extensively share knowledge and tools.

The work on the inclusive jet cross-section was done within the Standard Model (SM) physics group. There are ∼20 people participating in the SM measurements with high-transverse momenta jets in the group. The work focusing on the jet energy corrections was done within the JetEtMiss performance group. This group studies the reconstruction of jets and missing transverse energy $E_{\mathrm{T}}^{\mathrm{miss}}$. The thesis only describes parts with a significant author's contribution.

The thesis is split into four chapters. The first one briefly discusses the current theoretical background. The second one gives an overview of the ATLAS experiment with emphasis on the calorimetric system which is the most important part for the jet measurements. In the third chapter, the test of the two jet energy corrections is described. The inclusive jet cross-section measurement is the topic of the fourth chapter.

[1] In the high-p_{T} tail of the inclusive jet spectra radiative electroweak corrections start to be important as well.

1. Theoretical background

The current experimental results in the field of elementary particles are very well described by a theory called Standard Model (SM) within the framework of the quantum field theory. Present chapter provides a brief introduction to this theory with emphasis on the strong interaction. It is mainly based on [2, 3, 4, 5]. Other sources are cited in the text.

1.1 Standard model

SM is $\mathrm{SU(3)_{colour}} \times \mathrm{SU(2)_L} \times \mathrm{U(1)}_Y$ renormalizable gauge theory with spontaneous symmetry breaking performed by the Higgs mechanism. In the SM, there are three families of fermions interacting through the exchange of vector bosons and a scalar Higgs boson. A Higgs boson compatible with the SM prediction has recently been discovered at the LHC [6, 7].

The spontaneously broken $\mathrm{SU(2)_L} \times \mathrm{U(1)}_Y$ part describes electroweak interactions. The $\mathrm{SU(3)_{colour}}$ part is called quantum chromodynamics (QCD) and it describes the strong interaction. Gravity is not included in the SM but its effects are experimentally inaccessible in the physics of elementary particles. Also, the observations like dark matter and dark energy or the abundance of matter over anti-matter are not incorporated in the SM.

1.2 Introduction to QCD

QCD is the current theory of the strong interaction between colour-charged quarks and gluons. Quarks and gluons are identified with partons introduced by R. Feynman. QCD is gauge theory with $\mathrm{SU(3)_{colour}}$ internal symmetry. Gluons are the corresponding gauge bosons. QCD explains both the effects of quark confinement in hadrons and asymptotic freedom. Structure of hadrons is described by parton distribution functions (PDFs) which have the meaning of a probability to find a given parton carrying a momentum fraction x of the parent hadron. PDFs are not calculable from the first principles and have to be measured.

A typical interaction of two hadrons is split into several parts factorized from each other. Its heart is the interaction between two partons carrying fractions x_1, x_2 of momenta of the colliding hadrons. The cross-section of this so-called hard-scattering (HS) process is described by perturbatively calculable matrix elements. The hard scale on which the cross-section depends is usually called renormalization scale. The HS cross-section is convoluted with PDFs because the information on the incoming partons momenta is experimentally inaccessible. PDFs depend on the factorization scale μ_F at which the HS and the radiations from incoming partons factorize. Evolution of PDFs in μ_F is determined by the DGLAP formalism, still in the regime of perturbative QCD (pQCD).

Another separate part of the hadron-hadron interaction is the Underlying Event (UE) that describes interactions of partons not entering the HS. Since the knowledge of QCD in this soft regime is not solid enough, yet, phenomenological models have to be employed to describe the UE.

Finally, the outgoing colour-charged partons fragment into colourless hadrons that are the observable particles. The hadronization occurs at much lower scale than the HS. Therefore, it falls into the domain of non-perturbative QCD. There are attempts to calculate theoretical predictions for the soft processes within the framework of lattice QCD. However, the predictions are not available, yet, and phenomenological models have to be used.

1.3 QCD Lagrangian density

The QCD Lagrangian density can be written as

$$\mathcal{L}_{\mathrm{QCD}} = -\frac{1}{4} F^a_{\mu\nu} F^{a\,\mu\nu} + \sum_q \left(i \bar{\Psi}_q \gamma^\mu \partial_\mu \Psi_q - m_q \bar{\Psi}_q \Psi_q + g_{\mathrm{S}} \bar{\Psi}_q \gamma^\mu T^a \Psi_q A^a_\mu \right) \quad (1.1)$$

where the summation runs over all quark flavours q. Ψ_q is a vector with three components Ψ^i_q, each of them represents a quark field with colour i. A^a_μ stands for a gluon field with colour a related to the $\mathrm{SU}(3)_{\mathrm{colour}}$ generator T^a. There are 8 such gluon fields in QCD. Quarks are massive fermions with spin 1/2 and gluons are massless vector bosons. In Eq. (1.1), $F^a_{\mu\nu}$ is an antisymmetric tensor related to the gluon fields A^a_μ in a similar (but generalized) way as the electromagnetic tensor is related to the photon field:

$$F^a_{\mu\nu} = \partial_\mu A^a_\nu - \partial_\nu A^a_\mu + g_{\mathrm{S}} f_{abc} A^b_\mu A^c_\nu. \quad (1.2)$$

Here, f_{abc} are the structure constants of the $\mathrm{SU}(3)_{\mathrm{colour}}$ group.

One can easily check that the Lagrangian density (1.1) stays invariant under a local $\mathrm{SU}(3)_{\mathrm{colour}}$ transformation of the form

$$\begin{aligned} \Psi_q &\rightarrow \Psi'_q = S\Psi_q \\ A_\mu &\rightarrow A'_\mu = S A_\mu S^{-1} - \frac{1}{i g_{\mathrm{S}}} S \partial_\mu S^{-1} \\ S &= \exp(i\omega^a(x) T^a) \end{aligned} \quad (1.3)$$

where $A_\mu = A^a_\mu T^a$ and $\omega^a(x)$ are some functions of x.

1.4 Strong coupling α_{S}

Since QCD is based on the full (unbroken) $\mathrm{SU}(3)_{\mathrm{colour}}$ internal symmetry, it only contains one free parameter that has to be determined experimentally. This parameter is the coupling

$$\alpha_{\mathrm{S}} \equiv \frac{g^2_{\mathrm{S}}}{4\pi} \quad (1.4)$$

that quantifies the strength of the interaction. It appears in the first and the last term in Eq. (1.1). The sum of all terms containing α_{S} is usually called an interaction Lagrangian density, $\mathcal{L}_{\mathrm{I}}$. The coupling α_{S} is also used as an expansion

parameter in the Dyson series of the S-matrix, the evolution operator of a system under study:

$$\begin{aligned} S_{fi} &= \left\langle f \middle| T \exp\left(-i \int_{-\infty}^{\infty} \mathrm{d}t H_{\mathrm{I}}(t)\right) \middle| i \right\rangle \\ &= \left\langle f \middle| 1 + i\left(\int \mathrm{d}^4x \mathcal{L}_{\mathrm{I}}(x)\right) + \frac{i^2}{2} T\left(\int \mathrm{d}^4x \mathrm{d}^4y \mathcal{L}_{\mathrm{I}}(x)\mathcal{L}_{\mathrm{I}}(y)\right) \middle| i \right\rangle + \dots \end{aligned} \tag{1.5}$$

Here, S_{fi} is the S-matrix element describing the system evolution from an initial state $|i\rangle$ to a final state $|f\rangle$. T stands for a time-ordered product and $H_{\mathrm{I}}(t)$ is the interaction Hamiltonian of the system written in the interaction (Dirac) picture.[1]

The series is asymptotic and has zero radius of convergence. It means that it approaches the exact result S_{fi} up to some finite order of the expansion only. The next terms behave such that the sum deviates from S_{fi} more and more. The whole series (1.5) is divergent. In the following text, the word "convergence" will be used in the above meaning, i.e. convergence of a finite number of terms.

The structure of different terms in expansions of the S-matrix elements is conveniently described by Feynman diagrams. Diagrams related to the higher-order terms contain closed loops made up of particle propagators (virtual particles).[2] In the loops, one should integrate over all possible values of the virtual particles momenta, from zero to infinity. At a fixed order calculation, this integration often leads to divergences of process amplitudes. There are two different types of such divergences:

- Infrared (IR) divergences arising from the integration over small momenta of virtual particles with zero mass. Their treatment for two special cases is described in Sec. 1.5 and 1.6.
- Ultraviolet (UV) divergences coming from the integration over large momenta of virtual particles. They are treated with the use of the renormalization technique.

1.4.1 Renormalization and UV divergences

As stated above, the source of UV divergences is integration over large momenta of virtual particles enclosed in loops of higher-order Feynman diagrams. Large momentum is equivalent to a short distance. Therefore, the appearance of UV divergences indicates limited validity of the quantum field theory description of physics at very short distances. The situation is similar to that in classical continuum description of e.g. fluid dynamics (see [8] for justification). There, the

[1] Usually, the interaction Hamiltonian

$$H_{\mathrm{I}} = -\int \mathrm{d}^3x \mathcal{L}_{\mathrm{I}} \tag{1.6}$$

This relation holds in QCD. Note that the interaction Lagrangian density $\mathcal{L}_{\mathrm{I}}$ is written in the Dirac picture. In this picture, operators evolve in time according to the free Hamiltonian (without interaction terms); on the other hand, the evolution of physical states is fully determined by the interaction Hamiltonian.

[2] Propagator is a function that describes evolution of a free particle between two space-time points. It is defined as a vacuum expectation value of a time-ordered product of two fields related to one particle evaluated in two different space-time points.

description fails at short distances, at the atomic scales. However, it is valid at much larger distances; it is influenced by the atomic-scale physics through a certain number of parameters. For example, viscosity or speed of sound describe large distance phenomena but they can only be determined from the knowledge of the short distance ones.

In analogy, quantum field theory that describes short distance phenomena is influenced by an unknown physics of very short distances. The underlying physics enter in the effective quantum field theory description in the form of some parameters. The parameters can only be determined experimentally because the physics at the very short scales is unknown. The surprising observation is that a renormalizable quantum field theory is independent of the very short (cut-off) scale. Renormalization is a mathematical procedure that provides an effective description of quantum physics. It is usually used for three main purposes:

- It provides matching of theoretical predictions to experiment.
- It eliminates the theory dependence on the cut-off scale.
- It speeds-up the convergence of the Dyson series (1.5).

Let us briefly demonstrate how the renormalization procedure works. The amplitude $\mathcal{M}$ of a QCD process will serve as an example. In principle, it is possible to compute $\mathcal{M}$ up to any order of the Dyson series. Let us calculate it up to the second non-trivial order (the so-called next-to-leading order, NLO), here. The result $\mathcal{M}^{\mathrm{NLO}}$ looks like

$$\mathcal{M}^{\mathrm{NLO}} = \bar{\mathcal{M}}^{\mathrm{LO}}\, \alpha_{\mathrm{S}}^{0} \left(1 + \alpha_{\mathrm{S}}^{0} c_1(s,t,u)\right) \tag{1.7}$$

where $\bar{\mathcal{M}}^{\mathrm{LO}}$ stands for the amplitude calculated in the leading order (LO) from which the dependence on α_{S}^{0} is removed. The strong coupling α_{S}^{0} is written with the superscript 0 to indicate that it coincides with the bare one (before renormalization) that is implicitly present in Eq. (1.5). The function c_1 depends on momenta of the interacting particles and this dependence is expressed in the form of Mandelstam invariants s, t, u. This function is calculated with the use of Feynman diagrams. However, the diagrams contain loops and they are divergent if α_{S}^{0} is considered as a finite parameter.

The first step of the renormalization procedure is to regularize $\mathcal{M}^{\mathrm{NLO}}$. Regularization is a mathematical method whose goal is to push a divergence into a finite number of isolated terms. These terms depend on an introduced UV cut-off scale. In the simplest case, the cut-off is just the upper limit of the divergent integrals over virtual particles momenta. In the dimensional regularization, it has the meaning of extra space-time dimensions.[3] The divergence is restored in the limit of the momentum cut-off going to infinity or the extra space-time dimension parameter going to zero. After regularization, Eq. (1.7) reads:

$$\mathcal{M}^{\mathrm{NLO}} = \bar{\mathcal{M}}^{\mathrm{LO}}\, \alpha_{\mathrm{S}}^{0} \left(1 + \alpha_{\mathrm{S}}^{0} c_1^{\mathrm{div}}(s,t,u,\mu_{\mathrm{reg}},\mu_{\mathrm{R}}) + \alpha_{\mathrm{S}}^{0} c_1^{\mathrm{fin}}(s,t,u,\mu_{\mathrm{R}})\right) \tag{1.8}$$

[3] In the dimensional regularization, the number of space-time dimensions considered is usually $4 - 2\epsilon$ where ϵ stands for the cut-off scale. The simple momentum cut-off is often called Λ.

where c_1^{div} is the divergent term(s), i.e. $|c_1^{\mathrm{div}}| \to \infty$ for the cut-off scale μ_{reg} going to zero in the case of the dimensional regularization or to infinity in the case of the momentum cut-off. The function c_1^{fin} is finite and it does not depend on μ_{reg}. Notice the emergence of an additional scale μ_{R} that appears in both c_1^{div} and c_1^{fin}. It is an inevitable consequence of the regularization. The new scale μ_{R} is arbitrary and $\mathcal{M}^{\mathrm{NLO}}$ in (1.8) does not depend on its value. Eq. (1.8) can now be rewritten as

$$\mathcal{M}^{\mathrm{NLO}} = \bar{\mathcal{M}}^{\mathrm{LO}}\, \alpha_{\mathrm{S}}^0 \left(1 + \alpha_{\mathrm{S}}^0 c_1^{\mathrm{div}}(s,t,u,\mu_{\mathrm{reg}},\mu_{\mathrm{R}})\right)\left(1 + \alpha_{\mathrm{S}}^0 c_1^{\mathrm{fin}}(s,t,u,\mu_{\mathrm{R}})\right) \tag{1.9}$$

where the terms $\mathcal{O}\left((\alpha_{\mathrm{S}}^0)^3\right)$ have been neglected. Notice that this step made $\mathcal{M}^{\mathrm{NLO}}$ depend on μ_{R}. However, this dependence is of the order $\mathcal{O}\left((\alpha_{\mathrm{S}}^0)^3\right)$.

Having the result (1.9) at hands, the physical coupling can be defined as

$$\alpha_{\mathrm{S}}(\mu_{\mathrm{R}}) = \alpha_{\mathrm{S}}^0 \left(1 + \alpha_{\mathrm{S}}^0 c_1^{\mathrm{div}}(s,t,u,\mu_{\mathrm{reg}},\mu_{\mathrm{R}})\right). \tag{1.10}$$

Neglecting the terms $\mathcal{O}\left((\alpha_{\mathrm{S}}^0)^3\right)$, Eq. (1.9) can finally be rewritten as

$$\mathcal{M}^{\mathrm{NLO}} = \bar{\mathcal{M}}^{\mathrm{LO}}\, \alpha_{\mathrm{S}}(\mu_{\mathrm{R}}) \left(1 + \alpha_{\mathrm{S}}(\mu_{\mathrm{R}}) c_1^{\mathrm{fin}}(s,t,u,\mu_{\mathrm{R}})\right) \tag{1.11}$$

The important point is that $\alpha_{\mathrm{S}}(\mu_{\mathrm{R}})$ in Eq. (1.10) does not depend on μ_{reg}. Therefore, $\mathcal{M}^{\mathrm{NLO}}$ is also free of this cut-off scale. The independence of $\alpha_{\mathrm{S}}(\mu_{\mathrm{R}})$ on μ_{reg} is demonstrated by taking the derivative of Eq. (1.10) with respect to $\ln \mu_{\mathrm{R}}$. It yields

$$\frac{\mathrm{d}\alpha_{\mathrm{S}}(\mu_{\mathrm{R}})}{\mathrm{d}\ln(\mu_{\mathrm{R}})} = \beta_0 \left(\alpha_{\mathrm{S}}^0\right)^2 = \beta_0 \alpha_{\mathrm{S}}^2 + \mathcal{O}\left((\alpha_{\mathrm{S}}^0)^3\right) \tag{1.12}$$

where

$$\beta_0 = -(11 N_{\mathrm{C}} - 2 n_{\mathrm{f}})/6\pi \tag{1.13}$$

In the last expression, $N_{\mathrm{C}} = 3$ is the number of colours in QCD and n_{f} is the number of considered quark flavours. The Eq. (1.12) has an easy solution

$$\alpha_{\mathrm{S}}(\mu_{\mathrm{R}}) = \frac{-1}{\beta_0 \ln \frac{\mu_{\mathrm{R}}}{\Lambda}} \tag{1.14}$$

The parameter Λ has the meaning of a scale at which the perturbation theory is no longer valid at NLO.

Eq. (1.12) describes the evolution of the strong coupling α_{S} with a scale μ_{R}. The scale is an artifact of the regularization procedure, see Eq. (1.7) and (1.8). However, it turns out that it is advantageous to set μ_{R} differently for different processes. A good choice is usually $\mu_{\mathrm{R}} = \sqrt{Q^2}$ where Q^2 is the transferred momentum squared. This choice can speed up the convergence of (1.5) by decreasing the size of the coefficient function c_1^{fin} in (1.11) and the higher-order functions c_i^{fin}.

Since the number of quark flavours is definitely lower than 17, the constant β_0 is negative in QCD. As a consequence, the strong coupling decreases with increasing μ_{R} (typical energy scale of the studied process). The limit $\alpha_{\mathrm{S}}(\mu_{\mathrm{R}}) \longrightarrow 0$ for $\mu_{\mathrm{R}} \to \infty$ is called asymptotic freedom. QCD is a non-interacting theory in this energy regime. On the other hand, at low energies, $\alpha_{\mathrm{S}}(\mu_{\mathrm{R}})$ increases and

QCD becomes a strongly interacting theory. Therefore, QCD is a good adept for a description of the confinement of quarks and gluons in hadrons.

Note that the separation of the function c_1 into c_1^{div} and c_1^{fin} is arbitrary. It is possible to include any finite function in c_1^{div}, thus changing both c_1^{fin} and $\alpha_{\mathrm{S}}(\mu_{\mathrm{R}})$. The choice of the function c_1^{div} defines the so-called renormalization scheme.

An important question is the physical meaning of the coupling $\alpha_{\mathrm{S}}(\mu_{\mathrm{R}})$. Its value at a chosen scale must be determined experimentally. It can have the meaning of an amplitude of a selected process if one uses a renormalization scheme where c_1^{fin} is fully absorbed in c_1^{div} and thus $\mathcal{M}^{\mathrm{NLO}} = \bar{\mathcal{M}}^{\mathrm{LO}}\,\alpha_{\mathrm{S}}(\mu_{\mathrm{R}})$. Now, the theoretical prediction for any physical observable is expressed in terms of another one that was chosen for the $\alpha_{\mathrm{S}}(\mu_{\mathrm{R}})$ determination. In this sense the renormalization provides matching of theoretical predictions to experiment.

1.5 Parton distribution functions

The PDFs are of non-perturbative origin and cannot be calculated from the QCD principles at the moment. They must be determined experimentally. At a low factorization scale $\mu^2_{\mathrm{F},0} \sim 1\ \mathrm{GeV}^2$ (in the non-perturbative regime) some functional form is chosen; it contains several free parameters. The parameters must be fitted with the use of experimental data. The functional form describes the PDF dependence on the variable x at the initial scale $\mu^2_{\mathrm{F},0}$. x has the meaning of the hadron momentum fraction carried by a given parton. The PDFs do not only depend on x, they also depend on the factorization scale μ_{F}. This fact represents the famous Bjorken scaling violation which is one of the important successes of QCD. The μ_{F} dependence is described by DGLAP evolution equations. Their derivation relies on several important ingredients that will be briefly summarized. As an example, the deep inelastic scattering process of an electron on a proton $ep \to e +$ anything will be considered.

First of all, it is essential to recall that the zero gluon mass leads to singularities in cross-sections of processes involving a parallel gluon emission. Especially, the cross-section of the process $\gamma^* q \to qg$ has a singularity if the outgoing gluon p_{T} goes to zero:

$$\frac{\mathrm{d}\hat{\sigma}}{\mathrm{d}p_{\mathrm{T}}^2}(\gamma^* q \to qg) \overset{p_{\mathrm{T}}\to 0}{\approx} e_q^2 \hat{\sigma}_0 \frac{1}{p_{\mathrm{T}}^2} \frac{\alpha_{\mathrm{S}}}{2\pi} P_{qq}(z) \tag{1.15}$$

where e_q is the quark electric charge in units of the positron charge, $\hat{\sigma}_0 = 4\pi^2\alpha/\hat{s}$, $\hat{s}$ is the centre-of-mass energy of the $\gamma^* q$ system. $P_{qq}(z)$ is the quark-quark branching function that is closely related to the probability density of quarks inside a mother quark; the daughter quarks carry a momentum fraction z of their mother. This singular term comes from the process in Fig. 1.1a.

Second important thing is to realize that multiple parallel gluon emissions significantly increase cross-sections and compete with the suppression arising from the high power of α_{S}. It is therefore important to incoherently sum the contributions of all the processes with emitted gluons, see Fig. 1.1b. The leading term of a process involving n emitted parallel gluons is proportional to

$$\frac{1}{n!}\alpha_{\mathrm{S}}^n \log^n\left(\frac{\mu_{\mathrm{F}}^2}{\mu^2_{\text{cut-off}}}\right) \tag{1.16}$$

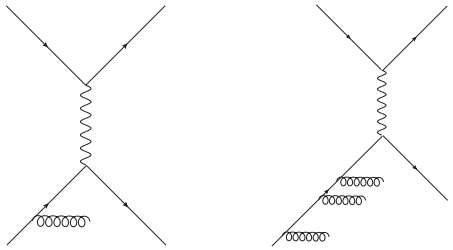

(a) (b)

Figure 1.1: Deep inelastic scattering process. Dominant one-gluon (a) and multi-gluon (b) emission Feynman diagrams in the limit of the gluons p_{T} close to zero.

where $\mu_{\text{cut-off}}$ is the low boundary in the integral over the emitted gluons p_{T}. This is the so-called leading-logarithm (LL). It must be stressed that each diagram is strongly ordered in p_{T} of the emitted gluons, i.e. the first emitted gluon has the lowest p_{T}, the second one has a larger p_{T} and so on up to the last emitted gluon (just before the HS).

The LLs are resummed with the use of the DGLAP equation:

$$\frac{\mathrm{d}q(x,\mu_{\mathrm{F}})}{\mathrm{d}\log(\mu_{\mathrm{F}}^2)} = \frac{\alpha_{\mathrm{S}}(\mu_{\mathrm{F}}^2)}{2\pi}\int_x^1 P_{qq}\left(\frac{x}{y}\right) q(y,\mu_{\mathrm{F}})\frac{\mathrm{d}y}{y} \tag{1.17}$$

The important point is that there is no longer any trace of the cut-off scale $\mu_{\text{cut-off}}$ in the renormalized quark distribution function $q(x,\mu_{\mathrm{F}})$. It means that the parallel logarithms are gone, they have been resummed. This equation describes the μ_{F}-evolution of the quark parton distribution function.

It should be emphasized that the DGLAP evolution equations are based on the limit $p_{\mathrm{T}} \to 0$, i.e. they resum the parallel logarithms. However, it is a common practice to set the factorization scale μ_{F} equal to the renormalization scale of the hard process, μ_{R}. Thus one enters the kinematic regime where the contribution from Fig. 1.1 no longer dominates the complete matrix element. On the other hand, this choice is usually well motivated. For instance, ($\mu_{\mathrm{F}} = \mu_{\mathrm{R}}$, μ_{R}) might be a saddle point of the theoretical prediction in the (μ_{F}, μ_{R}) plane. In such case, the μ_{F}, μ_{R} scales variation yields minimal theoretical uncertainty.

All the discussion above was mainly illustrative. Its generalization can be found elsewhere [3]. For example, it is important to include all the possible QCD processes which results in the branching functions P_{gq}, the quark-gluon branching function, P_{qg} and P_{gg}. They have analogical meaning to P_{qq}. They reflect the fact that a quark can split into a gluon-quark pair and a gluon can split into a quark or a gluon pair. Of course, all the quark and anti-quark flavours have an associate PDF as well as gluons. This leads to a system of coupled DGLAP equations describing the evolution of all the PDFs:

$$\begin{aligned}
\frac{\mathrm{d}q_i(x,\mu_{\mathrm{F}})}{\mathrm{d}\log(\mu_{\mathrm{F}}^2)} &= \frac{\alpha_{\mathrm{S}}(\mu_{\mathrm{F}}^2)}{2\pi}\int_x^1 P_{qq}\left(\frac{x}{y}\right) q_i(y,\mu_{\mathrm{F}}) + P_{qg}\left(\frac{x}{y}\right) g(y,\mu_{\mathrm{F}})\frac{\mathrm{d}y}{y} \\
\frac{\mathrm{d}\bar{q}_i(x,\mu_{\mathrm{F}})}{\mathrm{d}\log(\mu_{\mathrm{F}}^2)} &= \frac{\alpha_{\mathrm{S}}(\mu_{\mathrm{F}}^2)}{2\pi}\int_x^1 P_{qq}\left(\frac{x}{y}\right) \bar{q}_i(y,\mu_{\mathrm{F}}) + P_{qg}\left(\frac{x}{y}\right) g(y,\mu_{\mathrm{F}})\frac{\mathrm{d}y}{y} \\
\frac{\mathrm{d}g(x,\mu_{\mathrm{F}})}{\mathrm{d}\log(\mu_{\mathrm{F}}^2)} &= \frac{\alpha_{\mathrm{S}}(\mu_{\mathrm{F}}^2)}{2\pi}\int_x^1 P_{gg}\left(\frac{x}{y}\right) g(y,\mu_{\mathrm{F}}) + \sum_i P_{gq}\left(\frac{x}{y}\right)\left(q_i(y,\mu_{\mathrm{F}}) + \bar{q}_i(y,\mu_{\mathrm{F}})\right)\frac{\mathrm{d}y}{y}
\end{aligned} \tag{1.18}$$

The current state of art is to resum parallel logarithms up to the next-to-next-to-leading logarithm (NNLL), i.e. to consider terms like

$$\alpha_{\mathrm{S}}^{n} \log^{n-2}(\mu_{\mathrm{F}}^2/\mu_{\text{cut-off}}^2). \tag{1.19}$$

Nevertheless, the description of this extension is far from the scope of this thesis.

With the use of PDFs, a formula for a QCD theoretical prediction for a cross-section of a general process $AB \to cd$ can be written. Here, A, B are colliding hadrons and c, d are final state partons; $f_{a/A}(x, \mu_{\mathrm{F}})$ denotes the PDF of a parton a inside a hadron A. The symbols $\hat{\sigma}$ and $\hat{s}, \hat{t}, \hat{u}$ stand for the parton-level quantities: the cross section of a process $ab \to cd$ and the corresponding Mandelstam invariants.

$$\sigma = \sum_{a,b} \int \mathrm{d}x_1 \mathrm{d}x_2 f_{a/A}(x_1, \mu_{\mathrm{F}}) f_{b/B}(x_2, \mu_{\mathrm{F}}) \hat{\sigma}_{ab\to cd}(\hat{s}, \hat{t}, \hat{u}, \mu_{\mathrm{R}}, x_1, x_2, \mu_{\mathrm{F}}) \tag{1.20}$$

1.6 Jets

The HS process describes interaction between partons and there are partons in the final state of the HS as well. However, partons are not experimentally observable because they quickly fragment to hadrons. Some observable must be defined to provide a connection between the detectable hadrons and the underlying partons. Such observable is jet. Moreover, partons are problematic "observable" even at the theoretical level due to the zero gluon mass that leads to divergences in some matrix elements. Jet must be defined in such a way that it cures this problem.

Let us demonstrate the second problem on the well-known example of the hadron production in the e^+e^- collisions via the process $e^+e^- \to q\bar{q}g$. The corresponding tree-level Feynman diagrams are in Fig. 1.2. The corresponding

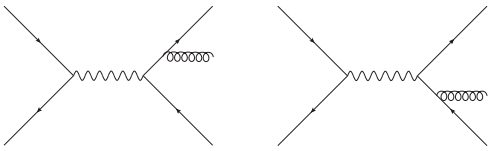

(a) (b)

Figure 1.2: Leading-order Feynman diagrams of the process $e^+e^- \to q\bar{q}g$.

cross-section diverges in the so-called soft or collinear limit, i.e. if the gluon is either very soft or emitted in a direction very close to the direction of the (anti-)quark. The divergence can be regularized by e.g. introduction of a non-zero gluon mass. It is apparent that the final states $q\bar{q}g$ and $q\bar{q}$ are experimentally indistinguishable if the gluon has nearly zero energy or if it is parallel to the (anti-)quark. The partons are not a good observable because in the soft or collinear limit, it is impossible to observe all of them. The jet must be defined in such a way that it consists of one parton above a given threshold imposed on some variable (given by e.g. experimental resolution) and of two partons (quark and gluon) below the threshold. The variable used for the separation of the two cases can be e.g. invariant mass of the gluon and the quark. This variable is very small in both the soft and the collinear limit. Below the threshold on the invariant

mass, the final states $q\bar{q}g$ and $q\bar{q}$ are indistinguishable, they are called degenerate. Therefore, the cross sections corresponding to both final states should be added. In this case, the divergent terms coming from the $q\bar{q}g$ contribution get cancelled by divergent terms coming from the interference of the Feynman diagrams in Fig. 1.3a and Fig. 1.3b, 1.3c, 1.3d. This is guaranteed by the Kinoshita-Lee-Nauenberg (KLN) theorem.

The KLN theorem is even more general. It guarantees the cancellation of the soft and collinear singularities by incoherently adding the contributions from final states that are degenerate with the studied process.

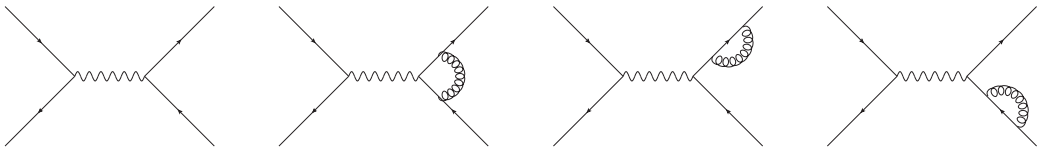

Figure 1.3: Leading-order (a) and next-to-leading order (b, c, d) Feynman diagrams of the process $e^+e^- \to q\bar{q}$.

1.6.1 Jet algorithms

The definition of a jet must reflect the basic requirements mentioned above. It has to allow variable parton content depending on the event topology and the parton (four-)momenta. It must also be suitable for other types of objects like e.g. stable particles or clusters of energy deposits in the calorimeter.

Jets are identified with the use of jet algorithms. A jet algorithm takes as input a collection of all the objects in an event final state. It clusters them into jets and determines the jet four-momenta on the basis of the constituting object ones. Two important classes are the cone and the sequential jet algorithms.

Typical problems of jet algorithms are soft and collinear instability and irregularity of geometrical jet boundaries. The first problem refers to the fact that addition of a soft object (parton, particle...) to an event might significantly change the clustered jet collection. Algorithms with this property are called soft-unsafe. In a similar way, the collinear-unsafe jet algorithms might change the jet collection if a final-state object is split into two. For certain algorithms, the addition of soft particles into the event can result in a significant change of the jet boundaries. Such behaviour can yield problems like e.g. more difficult jet calibration or large sensitivity to the UE. It can also make the comparison of data with theory difficult or even impossible.

There are essentially two ways how to determine the jet four-momenta: energy and four-momentum recombination schemes. The former sums all transverse energies of constituting objects and assumes the jet to be massless; the jet direction is then calculated as a transverse-energy-weighted sum of the constituent directions. The latter sums the four-momenta of the constituents which yields massive jets.

The ATLAS Collaboration uses the anti-k_{t} [9] jet clustering algorithm with the four-momentum recombination scheme.

1.6.2 Anti-k_{t} jet algorithm

As discussed in Sec. 1.5, QCD yields a very high probability for a parton to branch into two partons. The Eq. (1.15) demonstrates this fact for the case of a gluon emission from a quark. This behaviour results in a high number of partons in the final state of QCD processes. In general, the goal of a jet algorithm is to undo the parton branchings and to retrieve the "original" partons coming out from the HS.

The idea of the k_{t} jet algorithm [10] is to successively merge momenta of partons that have the largest probability to originate from a common mother parton. This probability is closely related to the measure of the parton distance, d_{ij}, that is evaluated for each parton pair (partons i and j) in an event and in each iteration of the algorithm. It is computed as

$$d_{ij} = \min\left(p_{\mathrm{T},\,i}^2,\ p_{\mathrm{T},\,j}^2\right)\frac{\Delta R_{ij}^2}{R^2} \tag{1.21}$$

where R is a parameter that defines the jet algorithm and ΔR_{ij} is the distance of partons i and j in the $\eta - \phi$ plane (see Sec. 2.2.1 for its definition). The smaller d_{ij} the larger is the probability for the parton pair to originate from a common mother parton. Complementary to d_{ij}, a parton-beam distance for parton i is defined as

$$d_{i\mathrm{B}} = p_{\mathrm{T},\,i}^2 \tag{1.22}$$

If the smallest number among all d_{ij} and $d_{i\mathrm{B}}$ is d_{kl} then partons k and l are merged into one and the algorithm re-iterates. If the smallest number is $d_{k\mathrm{B}}$ then the object k is called a jet, it is removed from the list of partons and the algorithm re-iterates. Notice that the parameter R in Eq. (1.21) has the meaning of a minimal angular separation between two jets. It is often called jet radius. Given this jet definition, one should notice that the number of jets is not an infrared safe quantity because soft partons close to the beam are likely to form a jet. However, the number of jets above some p_{T} threshold is infrared safe. The k_{t} algorithm starts merging the softest partons that are the closest to each other. Thus, the k_{t} algorithm reflects both QCD sources of divergences: soft and collinear parton branching. It can be shown that k_{t} is a collinear and infrared safe jet algorithm. On the other hand, the algorithm inevitably leads to irregular jet boundaries (see Fig. 1.4a) which yields some theoretical and experimental problems.

All the following discussion will use particles instead of partons because effects of pile-up will be considered. The term pile-up refers to an effect that happens if several hadron-hadron interactions occur at the same time. In such case it is more natural to talk about particles than about partons because the additional interactions add particles to the event. From the point of view of the discussion, there is no conceptual change between the two because the distribution of particles in an event is driven by the distribution of the underlying partons. And any jet algorithm must work at the particle level as well as at the parton one.

First problem of the k_{t} algorithm is its performance in cases when the UE and/or pile-up contributions are considered. Both UE and pile-up add soft particles to the event. The k_{t} algorithm treats these particles as being of the QCD branching nature. It means that the addition of UE and pile-up results in a

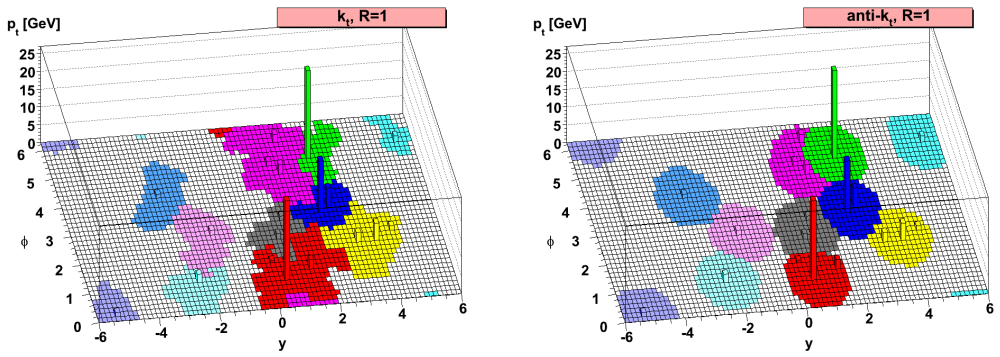

(a) (b)

Figure 1.4

significant change of the jet boundaries. Another problem is the so-called back reaction that refers to the fact that addition of soft particles (from either UE or pile-up) redistributes all the jet particle contents.

Due to these reasons it is advantageous to disfavour the effect of soft divergences in a jet algorithm. One way to do this is the anti-k_{t} algorithm. It works in a similar manner as the k_{t} one with an important exception: it defines the measure of the parton and the parton-beam distance differently:

$$\begin{aligned} d_{ij} &= \min\left(\frac{1}{p_{\mathrm{T},i}^2}, \frac{1}{p_{\mathrm{T},j}^2}\right)\frac{\Delta R_{ij}^2}{R^2} \\ d_{i\mathrm{B}} &= \frac{1}{p_{\mathrm{T},i}^2} \end{aligned} \tag{1.23}$$

This definition ensures that two soft particles are hardly ever to be merged; the algorithm prefers merging of a high-p_{T} particle with a collinear one. Due to this feature, anti-k_{t} yields circular jet boundaries, see Fig. 1.4b. As one can see from the figure, if two jets are close-by, one of them is circular and the other has a moon shape. Anti-k_{t} is a collinear and infrared safe jet algorithm. The parameter R that appears in the distance measure d_{ij} in Eq. (1.23) has a very illustrative interpretation. It is the radius of the jet cone in the $\eta - \phi$ plane.

Due to the rigid jet boundaries, anti-k_{t} suffers much less from the back reaction effect than k_{t}. It is still affected by the UE and pile-up but their contribution to the jet contents is more predictable. The response of the algorithm to the additional soft particles or the detector noise is linear which is not the case for k_{t}. This has a good impact on e.g. the algorithm efficiency that is defined, for a certain p_{T} range, as a fraction of the number of jets reconstructed at the detector level with respect to the particle level ones. Some other advantages of the anti-k_{t} jet algorithm are discussed in [9].

1.6.3 Relation between jet and parton properties

Strictly speaking, the identification of jets with outgoing partons holds in some special cases only. For example in the quark production processes on e^+e^- colliders. The general problem of hadron colliders is that diagrams related to the

radiation from the initial and final state partons can interfere. However, under special conditions one can still interpret jets as holders of the information on the outgoing partons. Basically, one has to avoid cases when the initial state radiation merges with an outgoing parton into one jet. This can be achieved if jets are very narrow. A narrow jet means that the jet radius R appearing in Eq. (1.21) or (1.23) is small. In the following discussion, this small-R limit will be exploited. Three effects with sizeable impact on the parton-jet relation are going to be mentioned in the discussion: parton radiation outside the jet cone, hadronization and UE. This section is based on results published in [11] and discussed in [12].

The first important theoretical result is the quantification of a parton radiation to the region outside the jet cone. As a consequence to this perturbative effect, the relative difference between the jet and the original parton p_{T} is:

$$\frac{\langle \delta p_{\mathrm{T}} \rangle_{\mathrm{pert}}}{p_{\mathrm{T}}} = \frac{\alpha_{\mathrm{S}}}{\pi} \ln R \times \begin{cases} 1.01 C_{\mathrm{F}}, & \text{quarks} \\ 0.94 C_{\mathrm{A}} + 0.07 n_{\mathrm{f}}, & \text{gluons} \end{cases} \tag{1.24}$$

where C_{F} and C_{A} are the corresponding colour factors (4/3 and 3 respectively) and n_{f} is the number of quark flavours. The R-dependence of the p_{T} radiated outside the jet cone is logarithmic. Notice also that on average the gluon-initiated jets lose more energy than the quark-initiated ones. The gluon jet losses due to the out-of-cone radiation are approximately twice as large as the quark jet ones.

The second source of the energy lost during the transition from a parton to the particle jet is the hadronization. This loss can also be evaluated quantitatively:

$$\langle \delta p_{\mathrm{T}} \rangle_{\mathrm{hadr}} = \frac{-0.4 \text{ GeV}}{R} \times \begin{cases} C_{\mathrm{F}}, & \text{quarks} \\ C_{\mathrm{A}}, & \text{gluons} \end{cases} \tag{1.25}$$

Notice the p_{T}-independence of the result and its $1/R$ functional form. This result is valid for anti-k_{t} jets.

Third source of the parton-jet energy discrepancy is the UE. In contrast to the out-of-cone gluon radiation and hadronization, UE increases the jet energy. Its contribution is proportional to the jet area which is πR^2 in the case of anti-k_{t} jets:

$$\langle \delta p_{\mathrm{T}} \rangle_{\mathrm{UE}} = 1.2 \text{ GeV} \times \pi R^2 \tag{1.26}$$

The constant of proportionality of about 1.2 GeV holds for proton-proton collisions at $\sqrt{s} = 7$ TeV. The jet area fluctuates for other jet algorithms and there is much more uncertainty in the $\langle \delta p_{\mathrm{T}} \rangle_{\mathrm{UE}}$ determination. On top of that, the UE contribution depends on the jet p_{T} for the jet algorithms other than anti-k_{t}.

2. LHC and the ATLAS experiment

2.1 LHC

LHC is a hadron accelerator that reaches unprecedented particle energies to explore physics in a new regime. It accelerates protons and heavy ions. It is built in a circular tunnel with circumference of ∼27 km. Particles circulate in opposite directions in two different beam pipes. The designed LHC energy is 7 TeV for protons and 2.8 TeV per nucleon for heavy ions. In order to reach so high particle energies on a ring of the given circumference, high magnetic field of 8.3 T is needed. This field is achieved with the use of the superconducting magnet technology.

The designed LHC instantaneous luminosity is 10^{34} cm^{-2} s^{-1} for protons and 10^{27} cm^{-2} s^{-1} for heavy ions. Protons circulate in 2808 bunches spaced by 25 ns for each proton beam. Nominally, each bunch contains 1.15×10^{11} protons. Bunches are grouped into trains that are separated by 320 ns. Due to the high instantaneous luminosity several pp interactions might occur in the same bunch crossing (event). This effect is called pile-up.

During the 2011 data taking period, the protons energy was 3.5 TeV yielding the centre-of-mass energy of 7 TeV. The peak instantaneous luminosity was 3.6×10^{33} cm^{-2} s^{-1} [13]. Not all the bunch positions were occupied and bunches were separated by 50 ns. The mean number of pp interactions per bunch crossing was ∼9.

On LHC, there are four interaction points where its two rings intersect. Around those points, four large particle detectors are built: ALICE, ATLAS, CMS and LHCb.

2.1.1 Data taking intervals

A basic unit of the data taking time is one run. A run is a continuous data taking unit that usually lasts several hours. Each run is split into intervals of ∼1 minute called luminosity blocks (lumiblocks). Runs are grouped into data taking periods. The 2011 7 TeV data used in the presented analysis consist of 10 periods: D, E,..., M.

2.2 ATLAS

The ATLAS detector [14] is a multipurpose experimental device. Its main goals are the search for the Higgs boson and for new physics. But many other interesting processes are studied in parallel.

The Higgs boson has been searched in a wide range of its masses and in several decay channels. Its discovery was based on the $H \to \gamma\gamma$ and $H \to ZZ^{(*)} \to 4l$ decay modes; l stands for an electron or a muon. Other channels are being carefully studied, such as the decays to W-bosons [15], τ-leptons [16] and b-

quarks [17]. The Higgs spin and parity was measured and it is consistent with the 0^+ prediction of the SM [18, 19].

The searches for new physics proceed in many different ways. A hot candidate is the supersymmetry [20, 21]. Production and decays of various supersymmetric particles like squarks and gluinos are probed [22]. $E_{\mathrm{T}}^{\mathrm{miss}}$ is an important feature of such events if R-parity is conserved because the lightest supersymmetric particle escapes the detector. Other new features and models are also being intensively studied [23], e.g. extra dimensions, microscopic black-holes, Technicolour models, gravitons, lepton flavour violation, four-fermion contact interactions, quark and lepton compositness, anomalous electroweak gauge boson couplings, Z' and W' bosons, new heavy quarks... No experimental evidence for new physics is available and the corresponding exclusion limits are set at the TeV scale.

ATLAS also performs many precision measurements within the SM. Physics of the top and bottom quarks is deeply studied. Weak gauge boson W and Z cross sections are measured as well as the jet and photon ones. Jet properties like shapes, mass and substructure are also measured. Soft QCD ATLAS program is very rich. It contains measurements of the event shapes, multi-parton interactions, charged-particle multiplicities, jet vetoes and azimuthal decorrelations and others.

ATLAS is also deeply involved in studies of the heavy-ion collisions. It came with an experimental evidence of the quark-gluon plasma [24]. The plasma properties are studied with the use of elliptic flow, i.e. angular correlations of particles produced in the heavy-ion collisions [25]. The temperature of the plasma can be estimated with the use of the J/ψ-yields centrality dependence [26]. Another interesting ATLAS result are the inclusive jet charged particle fragmentation functions [27].

To measure all the above observables, ATLAS must precisely reconstruct muons, photons, electrons and hadrons. These particles have very different properties. Therefore, ATLAS is divided into several parts as you can see in the Fig. 2.1. The device closest to the interaction point is the inner detector (ID). Its goal is to measure tracks and transverse momenta of charged particles and positions of primary and secondary vertices. The tracks of charged particles are bent in magnetic field generated by the central solenoidal magnet wound around the ID. The next part of ATLAS is the electromagnetic (EM) calorimeter system that is used to measure energy of particles. It is designed such that it fully absorbs EM showers. A complement to the EM calorimeter is the hadronic calorimeter. Its purpose is to measure energy of hadronic showers. It is especially important for precision measurement of jets and missing energy. Finally, the muon detector measures the momenta of muons by registering their tracks. In order to bend muon tracks a large toroidal magnet is used. This magnet winds all the cylinder of the ATLAS detector.

2.2.1 Coordinate system

The ATLAS coordinate system is Cartesian and right-handed. Its origin coincides with the interaction point. The x-axis of the system is parallel to the connecting line of the interaction point with the LHC ring centre. It points towards the centre. The y-axis is a vertical line that points from the interaction point to the

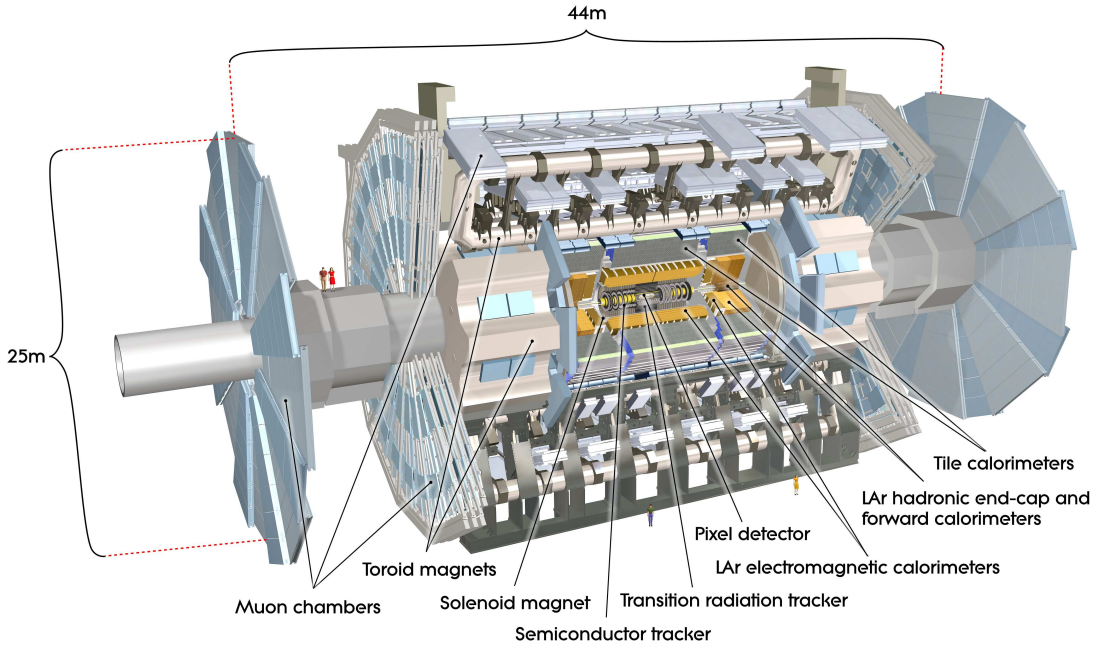

Figure 2.1: Schematic overview of the ATLAS detector and its main components. Figure provided by [28].

earth surface. The z-axis is parallel to the beam axis.

The spherical coordinates θ and ϕ are also frequently used on ATLAS. θ is the polar angle that is measured with respect to the positive z-axis. ϕ is the azimuthal angle measured with respect to the positive x-axis in the $x-y$ plane.

The pseudorapidity η is defined in the standard way as $\eta = -\ln\tan(\theta/2)$. It is a natural coordinate in High-Energy Physics (HEP) experiments. The distance ΔR in the $\eta-\phi$ plane is defined as $\Delta R = \sqrt{\Delta\eta^2 + \Delta\phi^2}$.

2.2.2 Inner detector

The ID measures tracks and transverse momenta of charged particles. The designed p_{T} resolution of tracks is $\sigma_{p_{\mathrm{T}}}/p_{\mathrm{T}} = 0.05\,\% \; p_{\mathrm{T}} \oplus 1\,\%$ where p_{T} is in GeV. The ID covers the region $|\eta| < 2.5$. It has full 2π coverage in the azimuthal angle. It is immersed in a magnetic field with $B = 2$ T generated by the central solenoid. For cooling, the solenoid is placed inside a cryostat. The ID consists of three parts: pixel detector, semiconductor tracker (SCT) and transition radiation tracker (TRT). Each of them has a barrel (central) and end-cap (more forward) parts.

The pixel detector is made from silicon and it has the highest granularity. In the barrel region, it achieves an accuracy of 10 μm in the $R-\phi$ direction and 115 μm in the z-direction. In end-cap, the accuracy is 10 μm ($R-\phi$) and 115 μm (R). The pixel detector consists of three layers (concentric cylinders) in the barrel part and four layers (disks perpendicular to the beam pipe) in the end-cap region.

The SCT is a silicon strip detector. It provides four space points for each track. In the barrel, it is formed by four concentric cylinders. Each cylinder consists of two layers of strip sensors. The layers have stereo strips shifted by

40 mrad to provide 2-D information. In the end-cap there are nine wheels with radially oriented stereo strips.

The TRT is formed by straw tubes filled with a xenon-based gas mixture that are parallel to the beam pipe (barrel) or radially-oriented (end-cap). It only provides coordinates in the $R - \phi$ plane. The number of hits per track is much larger ($\sim$36) than in the pixel detector or SCT. Therefore, it contributes significantly to the momentum measurement despite its lower spatial accuracy of 130 μm per straw.

2.2.3 Calorimeter system

The ATLAS calorimeter is composed of several subsystems with different characteristics. All of them are sampling calorimeters but they use different technologies and materials. Altogether, they cover the region $|\eta| < 4.9$ and they are symmetric along the azimuthal angle. They are designed to sufficiently absorb both EM and hadronic showers. The inner part, EM calorimeter, consists of barrel ($|\eta| < 1.475$) and end-cap ($1.375 < |\eta| < 3.2$) part. The hadronic calorimeter is located behind the EM one. Its central part is called Tile Calorimeter (TileCal) and covers the region ($|\eta| < 1.7$). The Hadronic End-Caps (HEC) span region $1.5 < |\eta| < 3.2$ and are located behind the EM end-caps. Finally, the Forward Calorimeter (FCal) is placed between the Hadronic End-Caps and the beam pipe. Its coverage is $3.1 < |\eta| < 4.9$. See Fig. 2.2 for a schematic overview of all the calorimeter system.

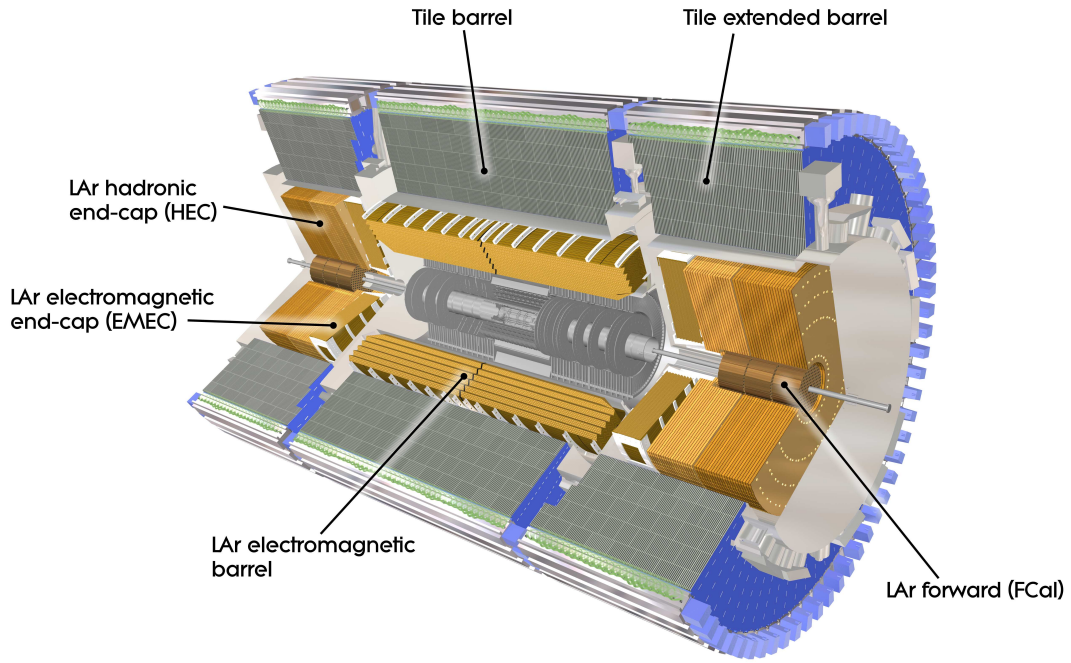

Figure 2.2: Schematic overview of the ATLAS calorimeter system. Figure provided by [28].

Liquid argon calorimeters

All the calorimeters except TileCal use the liquid argon (LAr) as the sensitive material. For the reason of cooling, they are placed in one barrel and two end-cap cryostats. Each cryostat consists of an inner cold and an outer warm vessel. The vessels have geometry of coaxial cylindrical tori with the axis given by the beam pipe. In the region between the two vessels, there is a vacuum for the reason of insulation.

The LAr calorimeters are located in the inner cold vessels of each cryostat. The analog signal from the calorimeters is brought through the insulation vacuum by feed-throughs to the front-end crates that are located on the outer surface of the cryostats. These crates contain the necessary read-out and calibration electronics, including the front-end boards (FEBs). The FEBs process and digitize the received analogue signal.

EM calorimeter

The EM calorimeter [29] uses lead as the absorber. The absorber and readout electrodes have accordion shape. This shape provides symmetry in the azimuthal angle, fast extraction of the signal and allows radial segmentation of the calorimeter. The barrel part is placed in the cryostat with the central solenoid. Each end-cap shares a cryostat with the Hadronic End-Cap and the Forward Calorimeters. In the region $|\eta| < 2.5$ ($2.5 < |\eta| < 3.2$) the EM calorimeter has three (two) layers in depth. Its $\Delta\eta \times \Delta\phi$ granularity is very fine: $\sim 0.025 \times 0.1$ (0.1×0.1) in the η region $|\eta| < 2.5$ ($2.5 < |\eta| < 3.2$). Besides other things it allows precise determination of photons direction. The thickness of the EM calorimeter is large assuring good containment of the EM showers. It is higher than 22 (24) radiation lengths X_0 in the barrel (end-caps), see Fig. 2.3. The designed energy resolution of both barrel and end-caps is $\sigma_E/E = 10\,\%/\sqrt{E} \oplus 0.7\,\%$ where E is in GeV.

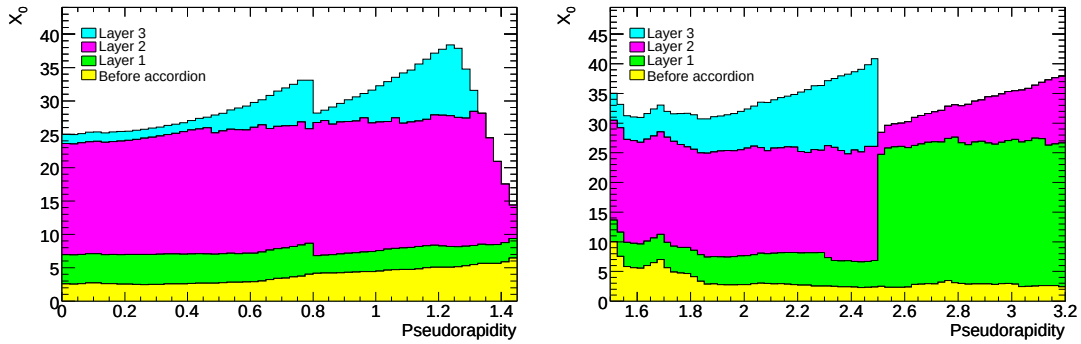

(a) (b)

Figure 2.3: The cumulative amount of material in the EM calorimeter as a function of η expressed in units of the radiation length X_0. The yellow area shows the amount of material before the first layer of the calorimeter.

Readout electrodes are made of kapton and are located in gaps between the accordion-shaped absorbers. The size of the drift gap on each side of the electrode (2.1 mm) together with the operating voltage (2000 V) determine the total drift time which is $\sim$450 ns. Passage of a charged particle through the gap ionizes the

liquid argon and results in an electric pulse of a triangular shape in time. This signal is further amplified, shaped, sampled and digitized. The readout electrodes are not always optimally placed in the gap. Thus, a typical signal is usually longer than the drift time (∼600 ns).

Hadronic End-Caps

HEC is sampling calorimeter that uses copper as the absorber. It consists of two wheels (front and rear wheel) on each side of the ATLAS detector. Each wheel consists of 32 wedge-shaped identical modules assuring the azimuthal symmetry and has two layers in depths. The $\Delta\eta \times \Delta\phi$ granularity of the HEC is 0.1×0.1 (0.2×0.2) in the region $1.5 < |\eta| < 2.5$ ($2.5 < |\eta| < 3.2$). The total thickness of HEC together with the EM end-caps in terms of the interaction length λ is 10λ, see Fig. 2.4. The designed energy resolution is $\sigma_E/E = 50\,\%/\sqrt{E} \oplus 3\,\%$ where E is in GeV.

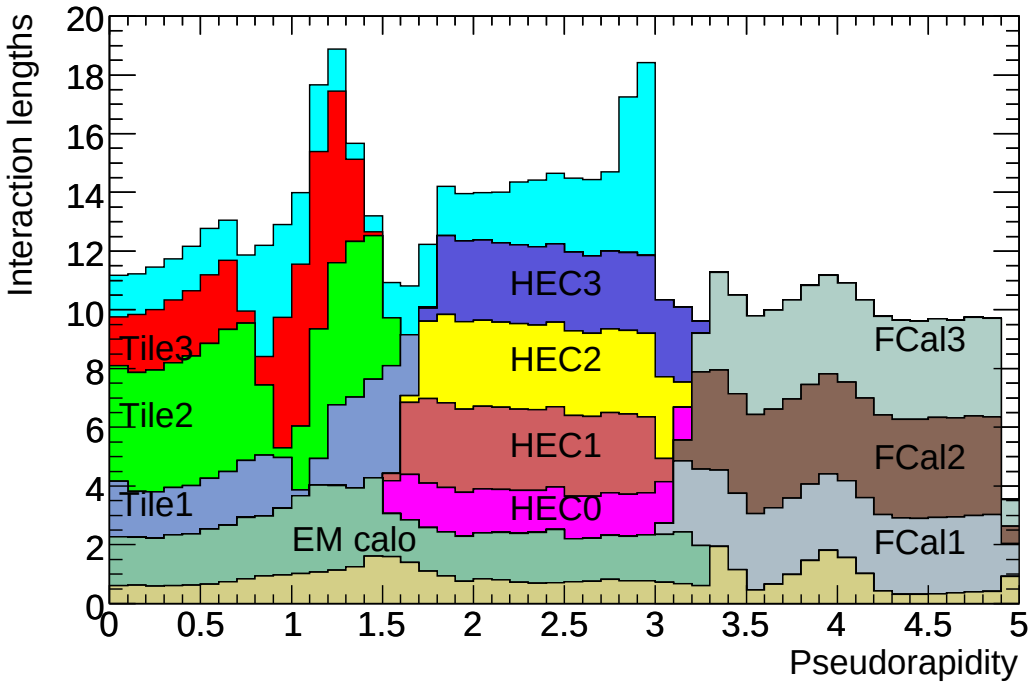

Figure 2.4: The cumulative amount of material in the ATLAS calorimeter system as a function of η expressed in units of the interaction length λ. The beige (light blue) area shows the amount of material before the EM calorimeter (before the first active layer of the muon spectrometer).

The HEC modules are made of copper plates perpendicular to the beam axis. Readout kapton electrodes are located in gaps between the plates. The electrodes layout resulting in 1.8 mm drift zones together with the 1800 V voltage applied yield a typical drift time of 430 ns.

Forward Calorimeters

FCal is the calorimeter that covers the high-$|\eta|$ region. It has two identical parts, one on each ATLAS side. Each part is subdivided into one EM module FCal1

and two hadronic modules FCal2, FCal3. The absorber is copper in FCal1 and tungsten in FCal2 and FCal3. Each module is a metal matrix with regularly spaced longitudinal channels consisting of concentric rods and tubes with liquid argon between them. The total thickness of FCal is 10λ, the designed energy resolution is $\sigma_E/E = 100\,\%/\sqrt{E} \oplus 10\,\%$ where E is in GeV.

Tile Calorimeter

TileCal [30, 31] uses iron as the absorber and plastic scintillator as the sensitive material. Its thickness is 7.4λ; the total calorimeter thickness in the barrel region is 9.7λ. The designed energy resolution of TileCal is $\sigma_E/E = 50\,\%/\sqrt{E} \oplus 3\,\%$ where E is in GeV.

The calorimeter consists of three cylindrical parts: long barrel (LB) covering the region $|\eta| < 1.0$ and one extended barrel (EB) on each side of ATLAS (EBA and EBC). Extended barrels cover the region $0.8 < |\eta| < 1.7$. Each cylinder consists of 64 wedge-shaped modules and is symmetric in the azimuthal angle.

In the region $0.8 < |\eta| < 1.2$, there is a gap between LB and EB. In order to include as much sensitive volume as possible there are special cells in the gap. The cells of Intermediate Tile Calorimeter (ITC) are located on the outer radius front surface of EB and cover the region $0.8 < |\eta| < 1.0$. Some of them have reduced volume. The gap scintillators are located on the inner radius front surface of EB, below the ITC, and cover the region $1.0 < |\eta| < 1.2$. They consist of one scintillator plate each.

Readout electronics is located in the outer part of each module. It is placed in drawers sliding into structural steel girders that are designed to tie modules and to close the magnetic field of the central solenoid. Each LB (EB) module is read-out by two (one) drawers. Therefore, from the readout point of view, LB is split at $\eta = 0$ into two subparts LBA and LBC. TileCal is thus formed by four so-called partitions: LBA, LBC, EBA, EBC. Each drawer has its own Low Voltage Power Supply (LVPS) that is located in an extension of its girder. TileCal High Voltage (HV) power supplies are located in an external cavern. One HV channel leads to each drawer where the HV is further distributed and controlled.

A TileCal module is made of iron and plastic scintillator tiles alternating each other. The tiles are perpendicular to the beam pipe. In the radial direction, each module has three layers. The layers are further split in cells.

Charged particles passing through the scintillator produce the scintillation light. The light is collected by two wavelength-shifting fibers, one on each side of the tile. Fibers reading a cell from one side are connected to a photomultiplier tube (PMT). One cell has two associated PMTs, one on each side. This cell read-out improves uniformity of the cell response and provides redundancy.

A PMT converts the light signal into an electrical pulse. The pulse is further shaped and split into two branches, gains. In the high-gain (HG), resp. low-gain (LG) branch it is amplified by a factor of 32, resp. 0.5. Each 25 ns, the analog pulses in HG and LG are digitized separately by two different 10-bit analog-to-digital converters (ADCs). ADCs are located on digitizer boards (digitizers), 12 ADCs on each. One digitizer manages 6 channels; channel is all the readout chain associated with one side of a cell.

TileCal pulses are shaped to a common form. The length of a pulse is $\sim$175 ns. The stored information about a pulse are seven digitized samples. The energy

deposited in a cell is proportional to the pulse amplitude A. A is extracted from the seven samples S_i with the Optimal Filtering algorithm [32], i.e. as a weighted sum

$$A = \sum_{i=1}^{7} w_i S_i \tag{2.1}$$

where w_i are known weights.

If an event is preselected by the ATLAS trigger system (see below), the seven samples from each channel in a drawer are passed to the interface (IF) card. This card converts electric signal to the optical one and sends it to the Read-Out Driver (ROD). ROD processes the received data to a format required by the trigger system and sends it via Read-Out Link (ROL) to the Read-Out Buffer (ROB).

2.2.4 Muon System

The goal of the Muon System is to measure tracks and transverse momenta of muons that penetrate through all the detector. It is equipped with large toroidal magnets that bend the tracks. The magnetic field of $B = 0.5$ T ($B = 1$ T) is generated by the large barrel toroid (two end-cap magnets) in the region $|\eta| < 1.4$ ($1.6 < |\eta| < 2.7$). In the transition region $1.4 < |\eta| < 1.6$, muon tracks are bent by a combination of both barrel and end-cap fields. Each magnet consists of eight superconducting coils. Each barrel coil is located in an individual cryostat whereas the end-cap magnets are each placed in one large cryostat.

The muon tracks are measured in the so-called muon chambers arranged in three layers. They are grouped in cylinders in the barrel region and wheels perpendicular to the beam pipe in the end-cap region. The relative alignment of the chambers is provided by the optical alignment systems. Precision track measurement in the bending direction is performed with Monitored Drift Tubes ($0 < |\eta| < 2$) and Cathode Strip Chambers ($2 < |\eta| < 2.7$).

The trigger system for the muon spectrometer consists of three parts. The Resistive Plate Chambers cover the barrel region and the Thin Gap Chambers are used in the end-cap regions. All the chambers have three roles. They measure tracks coordinate in the direction orthogonal to the bending one. They provide well-defined p_{T} thresholds. And they also serve for the bunch-crossing identification.

2.2.5 Trigger and Data Acquisition

The designed LHC collision frequency is 40 MHz. With a raw data size of $\sim$1.3 Mbyte per event it is impossible to store information about every collision. The ATLAS trigger system takes care about the selection of potentially interesting events that are to be stored. The indicators used are high-p_{T} electrons, photons, jets, τ-leptons, large missing transverse energy $E_{\mathrm{T}}^{\mathrm{miss}}$ or total transverse energy. Many different trigger chains with different thresholds are implemented to search for these signatures. The system consists of three levels: Level 1 (L1), Level 2 (L2) and Event Filter (EF).

The goal of L1 is to reduce the event rate to 75 kHz. The L1 decision is taken upon a reduced information about the event to achieve very short processing time of ∼2.5 μs. The L1 trigger can be so fast because it uses the analogue signal only. The signal it receives comes from the calorimeters, muon spectrometer and muon trigger chambers. L1 also identifies Regions of Interest (RoIs), i.e. regions in $\eta \times \phi$ where interesting features are found. RoIs are passed to L2. Before the L1 decision is taken, the digitized detector signals are stored in pipe-lines corresponding to each subdetector. If L1 accepts the event, they are formatted as raw data and transferred to the Data Acquisition (DAQ) system. DAQ stores the data in Read-Out Buffers before the L2 decision is taken. L2 has access to the full detector information in the RoIs. It reduces the trigger rate to ∼3.5 kHz within its processing time of ∼40 ms.

Events selected by L2 are transferred to the event-building system. EF then takes its decision using offline analysis algorithms. It reduces the trigger rate to the final ∼200 Hz with an average event-processing time of ∼4 s. After EF accept, data are transferred for the permanent storage to the CERN computer centre.

Important feature of L1 is pre-scaling of different trigger chains. As the instantaneous luminosity changes, the rates of different trigger chains change to optimize the usage of the available bandwidth. The inclusive jet cross-section measurement presented in this thesis uses a set of central single jet triggers. In 2011, the lowest unprescaled single jet trigger was EF_j240_a4tc_EFFS with the threshold of 240 GeV.

2.3 Monte Carlo simulation

An essential part of the ATLAS experiment is a detailed detector simulation [33] that is based on the GEANT4 toolkit [34]. It is used to study the detector response to various physical objects, e.g. jets. An important application of the simulation is the data unfolding, i.e. deconvolution of detector effects from data. Monte Carlo (MC) simulation is also used to plan data analyses strategies.

The ATLAS simulation chain consists of three main steps: event generation, simulation (propagation of stable particles through the detector) and digitization (modeling of the read-out electronics response to energy deposits in the sensitive parts of the detector).

The event generation is performed by various MC generators such as PYTHIA [35, 36], HERWIG [37, 38], POWHEG [39, 40, 41] and others. The output is a list of particles considered as stable, i.e. with lifetime τ long enough not to decay before entering the detector: $c\tau > 10$ mm.

In the next step, GEANT4 simulates the interactions of generated particles with the material of the detector. The detector must be described in detail, including its (temporary) defects. The output is a list of hits (energy deposits) in the individual sensitive parts of the detector.

Finally, the hits are digitized, i.e. the functionality of the read-out electronics is simulated. The output are summary files in the same format as data. In addition to this detector-level output the information on the original generated event is stored. Jet MC contains information about jets built from stable particles (truth jets).

Pile-up simulation

Under the LHC data taking conditions, there are two different effects caused by pile-up.

- In-time pile-up is the mutual influence of several proton-proton collisions that happen in the same bunch-crossing.
- Out-of-time pile-up is the influence of the detector response during a given bunch-crossing by the preceding proton-proton collisions. This happens because the read-out time of some subdetectors is longer that the bunch-spacing. For example, the LAr (TileCal) pulse length is ∼600 ns (∼175 ns).

In MC, the pile-up is simulated by overlaying the generated (hard) pp interaction with minimum-bias events. For both the hard and the minimum-bias events simulation, the same MC event generator is used. The amount of simulated pile-up events is chosen such that it matches the data as close as possible. The pile-up conditions are usually described by three parameters:

- μ_{act} - the expected number of pp collisions for a given bunch crossing averaged over one lumiblock.
- μ_{avg} - the expected number of pp collisions in a bunch crossing averaged over all the bunch-crossings and over one lumiblock.
- NPV - the number of reconstructed primary vertices in a bunch crossing.

The number of the in-time pile-up pp collisions is approximated by NPV whereas μ_{avg} is used to estimate the amount of out-of-time pile-up collisions.

For technical reasons, pile-up events are simulated separately. They are merged with the hard pp interaction after the simulation step of the MC production. The number of in-time pile-up events is randomly chosen from a Poisson distribution with mean equal to μ_{avg}. The time of in-time pile-up events is the same as the time of the hard pp interaction. The time of out-of-time pile-up events is shifted with respect to the hard interaction. The time shifts are chosen to model the bunch/train structure of the LHC beam. For each time shift, there is a set of out-of-time pile-up events. For a given shift, the number of out-of-time pile-up events is picked from a Poisson distribution with mean equal to μ_{avg}. All the bunch crossings are considered to have the same luminosity.

Since the MC production is often not specific to one single analysis and the exact pile-up conditions in data are often not known at the time of the production, MC events[1] need to be weighted in such a way that a pile-up-related variable distribution matches with data exactly.

2.4 Jet reconstruction and calibration on ATLAS

Jets are objects whose reconstruction and calibration [42] is a very complex task. It consists of three main steps:

[1] In general, each entry to the measured observable distribution could be weighted.

- Formation of elementary jet constituents, topological clusters (topoclusters), from calorimeter cells with significant energy deposit.
- Jet finding algorithm with topocluster four-momenta as input.
- Correction of jet directions and energies.

2.4.1 Topoclusters

Topoclusters are built from calorimeter cells with a dedicated clustering algorithm [43]. First step in the algorithm is to find seeds, i.e. cells with energy significantly higher than that due to electronic noise, σ. As a consequence of narrow bunch spacing and several pp interactions in one event in 2011, there is one additional term σ_{pileup} constituting σ so that $\sigma = \sqrt{\sigma^2_{\text{noise}} + \sigma^2_{\text{pileup}}}$. This term accounts for the fact that there might be energy deposits unrelated to the hard-scattering process or residuals from previous events due to large readout calorimeter time with respect to the 50 ns bunch spacing. The requirement for a seed cell energy is $E_{\text{seed}} > 4\sigma$.

As a second step, for each seed cell topological neighbours are added to the corresponding topocluster. If energy of a neighbour cell $E_{\text{neighbour}} > 2\sigma$ this cell becomes a seed and the algorithm re-iterates. If a cell satisfies conditions for addition to two topoclusters and its energy $E_{\text{neighbour}} > 2\sigma$ the two topoclusters are merged; if $E_{\text{neighbour}} < 2\sigma$ then the cell is added to the topocluster that has a cell with higher E/σ on the border with the studied cell.

The third step is to assign four momenta to topoclusters. The topocluster centre is determined as the energy-weighted mean of the constituent cells geometrical centres in x, y, z coordinates:

$$(\langle x\rangle, \langle y\rangle, \langle z\rangle) = \frac{\sum_{k|E_k>0} E_k(x_k, y_k, z_k)}{\sum_{k|E_k>0} E_k} \tag{2.2}$$

The direction of the topocluster lies along the connecting line between the interaction point and the topocluster centre. Finally, topoclusters are treated as massless objects which fixes the absolute value of momentum once the energy is known.

Local cluster weighting

All the ATLAS calorimeters are non-compensating which means that the response to electrons and photons is higher than to hadrons. Hadron energy losses due to interactions with nuclei or decays to particles escaping the calorimeter like muons and neutrinos are not measured. The cell information about deposited energy provided by the calorimeter system is at the so-called electromagnetic (EM) scale: calorimeters are calibrated such that the ratio of the reconstructed energy of EM showers with respect to their true energy is close to one.

As stated above, a certain portion of the energy of hadronic showers is not reconstructed by the calorimeters. This feature must be corrected for in the data processing. The local cluster weighting (LCW) scheme [44] is a part of the jet calibration procedure that corrects for it at the level of topoclusters before the

jets are built. LCW also corrects for the particles energy losses in inactive regions of the ATLAS detector and for the out-of-cluster energy deposits.

The LCW procedure has four main parts:

- Classification of topoclusters as hadronic-like or EM-like. The probability p for a topocluster to originate from a hadronic interaction is determined. The discriminating variables used are the measured energy density and the longitudinal shower depth. The dependence of p on the pion type (charged vs. neutral) as a function of the pion energy is shown in [45].
- Hadronic weighting of cells in topoclusters. The hadronic weight w_{had} is a function of the topocluster energy, cell energy density, η and calorimeter layer. The actual applied weight is $w_{\text{had}} \cdot p + w_{\text{EM}} \cdot (1-p)$ where $w_{\text{EM}} = 1$.
- Correction for out-of-cluster energy deposits inside the calorimeter. There are two types of this correction: for hadronic-like and EM-like topoclusters. They are applied with weights p and $(1-p)$ respectively.
- Correction for inactive detector material like the cryostats walls. It is derived separately for hadronic-like and EM-like topoclusters. The corresponding weights of the two sets are again p and $(1-p)$.

2.4.2 Jet finding algorithm

In ATLAS, jets are reconstructed using the anti-k_t algorithm [9] with the four-momentum scheme. The software implementation of the algorithm is provided by the FastJet package [46]. The input to the algorithm is a set of reconstructed topoclusters calibrated at the LCW scale. Jet radius parameters used are $R = 0.4$ and $R = 0.6$. The advantages of the anti-k_t algorithm are infrared and collinear safety and soft-resilience that leads to regular jet shapes not influenced by soft radiation.

2.4.3 Jet calibration

The goal of the final jet calibration procedure is to bring jets from the energy scale set by the LCW scheme (LCW scale) to the final jet energy scale (JES). The procedure is therefore called LCW+JES. All the jet calibration together with the determination of its systematic uncertainty is thoroughly described in [42]. It consists of four main steps, see Fig. 2.5. Alternatively, jets can be built

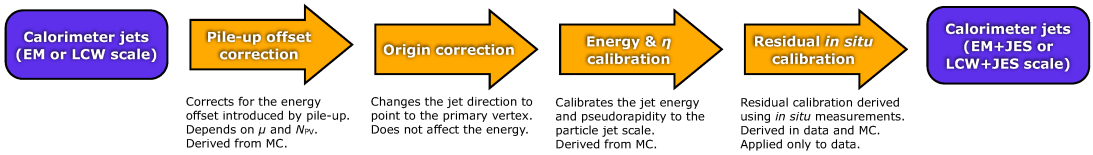

Figure 2.5: Schematic overview of the ATLAS 2011 jet calibration procedure.

from topoclusters on the EM scale. The corresponding calibration procedure (EM+JES) is also performed by ATLAS. However, the advantage of LCW+JES is better jet energy resolution (JER) because it reduces fluctuations resulting from the non-compensating nature of the calorimeter, see Fig. 2.6.

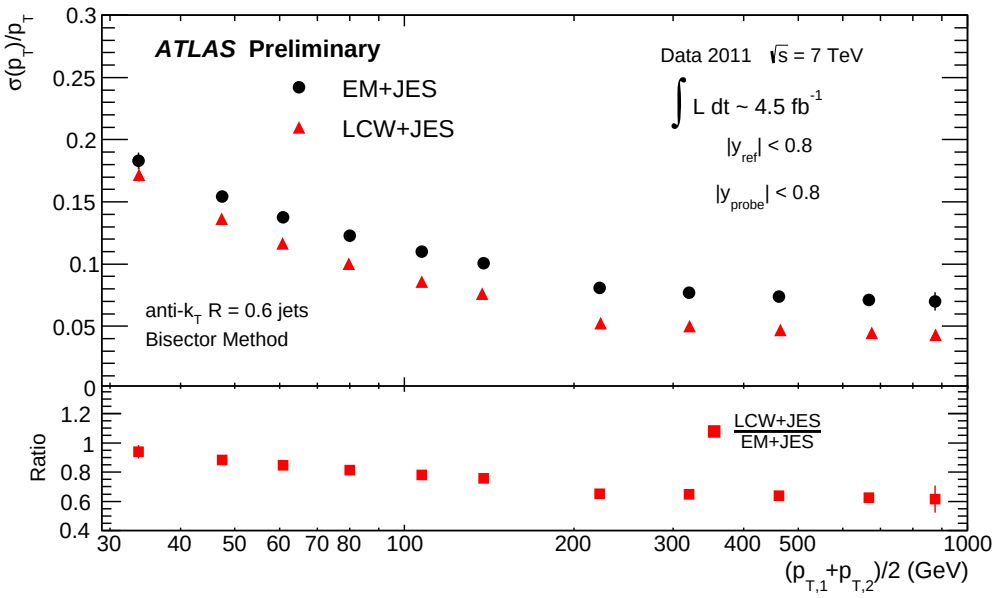

Figure 2.6: The jet energy resolution for jets calibrated with the LCW+JES and EM+JES procedure. The figure is taken from [47].

The different steps of the ATLAS jet reconstruction (Fig. 2.5) are briefly described below.

Pile-up correction

Pile-up influences the jet energies in two different ways:

- In-time pile-up increases the jet energy by contributions from the UE and from additional pp interactions in the same event.
- Out-of-time pile-up influences the jet energy reconstruction due to deterioration of calorimeter pulses by residual energy deposits coming from the previous and next events.

The pile-up correction subtracts the contributions of both in-time and out-of-time pile-up from the reconstructed jet energy.

Origin correction

As discussed above, jet constituents (topoclusters) directions point to the nominal centre of the ATLAS detector, to the interaction point. Therefore, the jet directions point to the ATLAS centre as well. However, the primary event vertex might be displaced from the ATLAS centre due to the finite proton bunch sizes. The origin correction makes each jet point to the vertex.

JES correction

With the use of MC, the average jet energy response is determined as a ratio of the reconstructed jet and the truth jet energy:

$$\mathcal{R}^{\mathrm{LCW}} = E_{\mathrm{jet}}^{\mathrm{LCW}} / E_{\mathrm{jet}}^{\mathrm{truth}} \tag{2.3}$$

The jet calibration function is defined as the inverse of $\mathcal{R}^{\mathrm{LCW}}$. The average response is determined in bins of jet energy and η. See Fig. 2.7 for its dependence on these two variables.

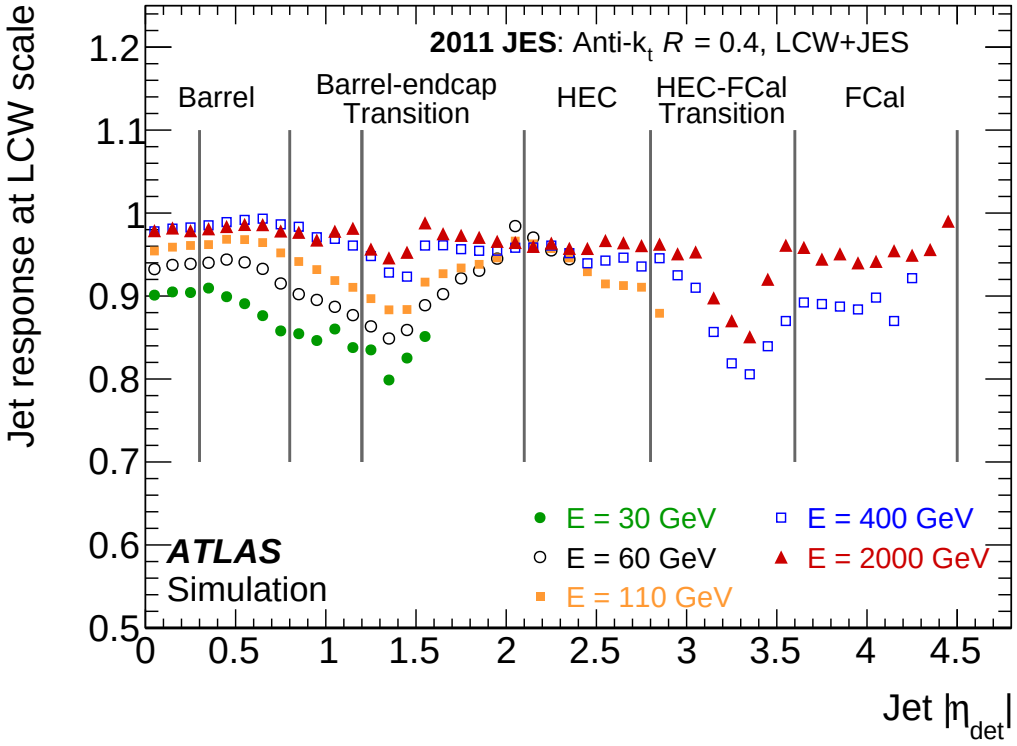

Figure 2.7: Average response of jets at LCW scale as a function of jet η for five different jet energies.

In situ corrections

Final step in the jet calibration procedure is the application of corrections reflecting differences between data and MC. The methods used are based on the transverse momenta balance between a jet and a well-calibrated reference object like e.g. a photon or a Z-boson decaying to two electrons. Since the in situ procedure only corrects for differences between data and MC, the actual correction applied is the inverse of a response ratio that is defined as a double-ratio data/MC of the jet responses $p_{\mathrm{T}}^{\mathrm{jet}}/p_{\mathrm{T}}^{\mathrm{ref}}$ where $p_{\mathrm{T}}^{\mathrm{ref}}$ is a transverse momentum of the reference object. Explicitly, the response ratio $\mathcal{R}$ is defined as

$$\mathcal{R} = \frac{\langle p_{\mathrm{T}}^{\mathrm{jet}}/p_{\mathrm{T}}^{\mathrm{ref}}\rangle_{\mathrm{data}}}{\langle p_{\mathrm{T}}^{\mathrm{jet}}/p_{\mathrm{T}}^{\mathrm{ref}}\rangle_{\mathrm{MC}}} \tag{2.4}$$

First of all, an equalization of the calorimeter response to jets over all its η-coverage is performed with the use of the dijet balance technique. The procedure is based on transverse momentum conservation in dijet events. Jets from lower $|\eta|$-regions are used to calibrate jets with higher $|\eta|$.

Further in situ corrections are derived in the $|\eta| < 1.2$ region where there is sufficient statistics for more techniques. There are three choices of the reference object available in different $p_{\mathrm{T}}^{\mathrm{jet}}$ regions:

- Z-boson decaying to two electrons in Z-jet events:
  $15\ \text{GeV} \lesssim p_{\text{T}}^{\text{jet}} \lesssim 200\ \text{GeV}$
- Photon in γ-jet events: $25\ \text{GeV} \lesssim p_{\text{T}}^{\text{jet}} \lesssim 800\ \text{GeV}$
- System of lower-p_{T} jets balancing the leading jet in multijet events:
  $200\ \text{GeV} \lesssim p_{\text{T}}^{\text{jet}} \lesssim 1200\ \text{GeV}$

Each technique determines the response ratio in bins of $p_{\text{T}}^{\text{ref}}$. Then, a common fine $p_{\text{T}}^{\text{ref}}$-binning is chosen. For each technique, the values of the response ratio in the fine bins are interpolated with the use of a second order polynomial. Then, in each (fine) $p_{\text{T}}^{\text{ref}}$ bin, the results of the three methods are combined as a weighted average; the weights are determined from a χ^2 minimization of the response ratio. The methods get different weights depending on $p_{\text{T}}^{\text{ref}}$ and the corresponding uncertainty. The combined data-to-MC jet response ratio derived in situ with $R = 0.4$ jets in the $|\eta| < 1.2$ region is shown in Fig. 2.8.

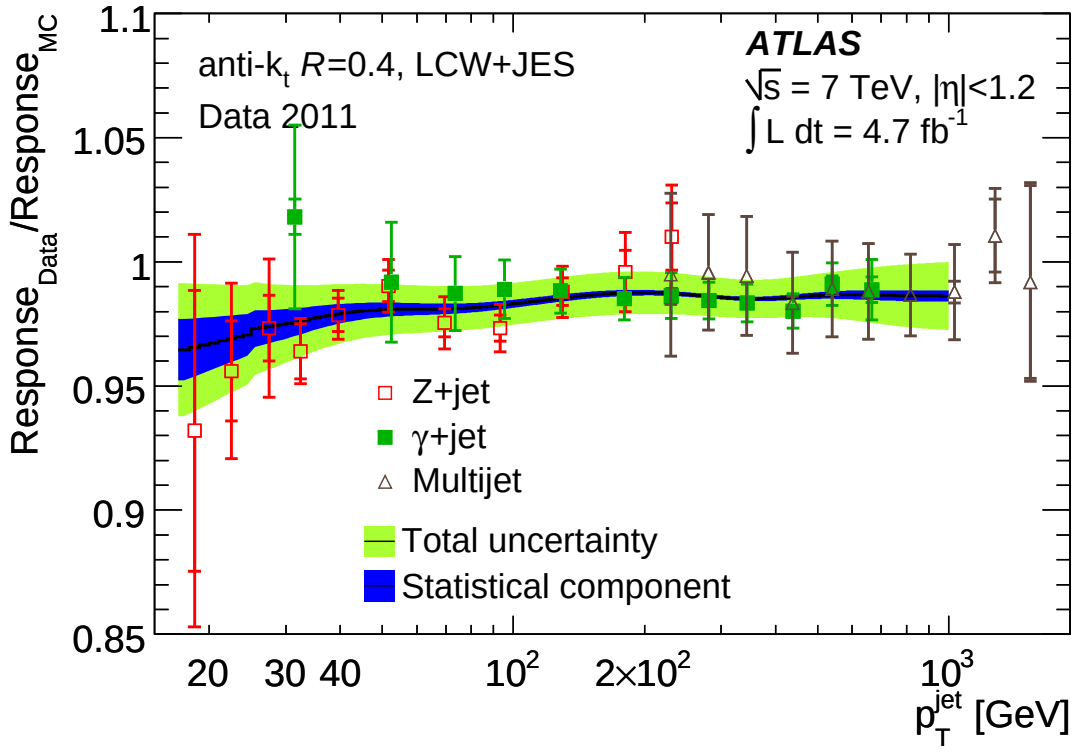

Figure 2.8: The data-to-MC jet response ratio derived in situ with three different methods (points). The combined result is displayed by the black line. The bands show its uncertainty. Jets are clustered with the anti-k_{t} algorithm, $R = 0.4$.

2.4.4 Jet calibration uncertainty

The uncertainty of the jet calibration (often called JES uncertainty) in the $|\eta| < 1.2$ region is derived from the uncertainties of all the in situ techniques used. Each technique has several uncertainty components that are treated as independent from each other. Each component is assumed to be fully correlated in both

p_{T} and η. The propagation of the uncertainty related to an uncertainty component of a calibration method is performed by coherently shifting the jet response determined by the corresponding method in each p_{T} bin by one standard deviation, redoing the combination as described in Sec. 2.4.3. The difference of the result from the nominal combined data-to-MC jet response ratio is interpreted as one standard deviation corresponding to the uncertainty component under study. In total, there are 63 uncertainty components of the jet energy calibration. The total JES uncertainty is shown in Fig. 2.8.

The JES uncertainty in the $1.2 < |\eta| < 4.5$ region is derived from the uncertainty in the $|\eta| < 1.2$ with the use of the dijet balance technique.

3. Non-operating TileCal modules

TileCal has very high data taking efficiency. However, no device works on 100 % for all the data taking period. During the period, the calorimeter experiences some failures of its hardware. The hardware problems are usually treated such that the corresponding problematic channels are masked for further data processing chain. The energy deposited inside the region that is not read must be estimated and the estimation introduced as a correction in the data analysis. For jets containing a masked TileCal cell, there are two corrections available. The goal of this chapter is to check their performance for cases when a jet falls into a region with a non-operational TileCal module. The technique used for this check is a p_{T} balance between two leading jets in dijet events.

3.1 Bad TileCal channels

A TileCal channel is tagged as bad if it has some important operation problem. Such channels are masked for further data processing chain. There are two basic types of bad channels: temporary and permanent. The reason for a temporary bad channel is e.g. a trip of the LVPS. Those channels are identified and masked "on-the-fly" (online) by a dedicated algorithm. The reasons for permanent bad channels are serious problems, e.g. channel off (due to LVPS), serious ADC problems, etc. If both channels reading a cell are bad the cell is tagged as bad and masked consequently.

At the end of the 2011 pp collision period, there were ∼5 % of masked TileCal cells. Fig. 3.1 shows the evolution of the fraction of masked cells as a function of time for both years 2011 and 2012. Most of those cells belong to 12 modules that failed during the period.

3.2 Bad cell energy correction

If one channel is bad and the other reading the same cell is not, the bad channel is assigned energy and time measured by the good one. More problematic situation arises if both channels reading one cell are masked. In such cases, more complicated energy correction must be used. There are two options developed to estimate the energy not measured by a masked TileCal cell inside a jet. They are called $\mathrm{BCH}_{\mathrm{cor,\,cell}}$ and $\mathrm{BCH}_{\mathrm{cor,\,jet}}$ in [42].

3.2.1 $\mathrm{BCH}_{\mathrm{cor,\,cell}}$

This correction estimates the energy deposited in a masked cell on the basis of energy density measured by its neighbour cells inside the same calorimeter layer. The masked cell energy density is evaluated as an arithmetic mean of the neighbour cell energy densities. The energy of the masked cell is determined as

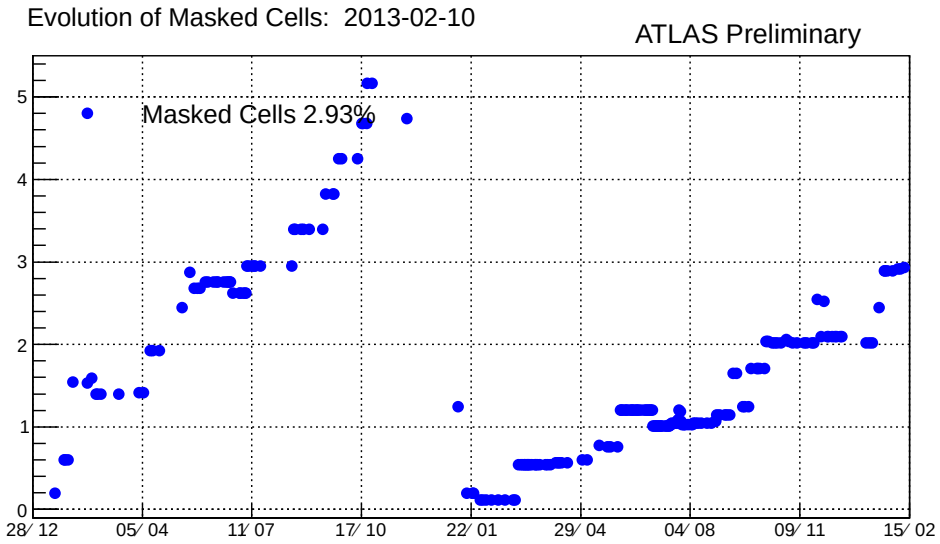

Figure 3.1: Fraction of masked TileCal cells as a function of time for 2011 and 2012 data taking periods. At the end of the 2011 (2012) data taking there were ∼5 % (∼3 %) of masked cells.

a product of the estimated energy density and the cell volume. The neighbour cells must satisfy the following requirements:

- Not to have zero volume (as e.g. the gap scintillators have).
- Not to be bad cells.
- Belong to the same subdetector and layer as the cell being corrected.

This correction is the ATLAS default and it is applied to cells before the topoclusters and jets are constructed.

$\mathrm{BCH}_{\mathrm{cor,\,cell}}$ underestimates the masked cell energy if the deposited energy density is larger than in the neighbour cells. This happens if the masked cell lays inside a high-energetic jet core around the jet axis and if the neighbours lay in larger distance from the axis where there is much less jet energy. This is a typical situation because most energy of a jet is contained inside a narrow cone around the jet axis and there is much less energy in cells more distant from the axis [48].

On the other hand, $\mathrm{BCH}_{\mathrm{cor,\,cell}}$ tends to overestimate the masked cell energy if the deposited energy density is lower than in a neighbour cell. This is another typical situation that happens if the masked cell lays in larger distance from the jet axis than a neighbour cell laying inside the jet core.

3.2.2 $\mathrm{BCH}_{\mathrm{cor,\,jet}}$

This second available correction estimates the energy deposited in masked cells on the basis of the average transverse jet shapes [48]. It is applied after the jet reconstruction to jets at the EM scale. The reconstruction is performed with the use of the default $\mathrm{BCH}_{\mathrm{cor,\,cell}}$ correction.

$\mathrm{BCH}_{\mathrm{cor,\,jet}}$ is derived from MC with all the TileCal modules set as operational. $\mathrm{BCH}_{\mathrm{cor,\,jet}}$ is constructed regarding the type and layer of calorimeter to which the

cell belongs, jet p_{T} and η and the distance dR in the $\eta - \phi$ plane between the cell centre and the jet axis. The correction is applied to jets at the EM scale in the following way:

$$E_{\mathrm{jet}}^{\mathrm{corr}} = \frac{E_{\mathrm{jet}}^{\mathrm{uncorr}}}{1 - \mathrm{BCH}_{\mathrm{cor,\,jet}}} \tag{3.1}$$

where ($E_{\mathrm{jet}}^{\mathrm{uncorr}}$) $E_{\mathrm{jet}}^{\mathrm{corr}}$ is the (un)corrected jet energy and $\mathrm{BCH}_{\mathrm{cor,\,jet}}$ is evaluated as

$$\mathrm{BCH}_{\mathrm{cor,\,jet}} = \sum_{\mathrm{masked\ \ cells}} \frac{E_{\mathrm{cell}}}{E_{\mathrm{jet}}} \tag{3.2}$$

with E_{cell} being the estimated energy deposited in a masked cell contained in the jet.

3.3 In situ dijet p_{T} balance method

To check the performance of $\mathrm{BCH}_{\mathrm{cor,\,cell}}$ and $\mathrm{BCH}_{\mathrm{cor,\,jet}}$ on the jet energies, the in situ dijet p_{T} balance method is used. It is based on the fact that the average difference between two leading jets transverse momenta is zero in dijet events. One jet is required to fall into an operational calorimeter region (tag jet). The other jet is required to hit a vicinity of one chosen non-operational TileCal module (probe jet). The average relative response $1/c = p_{\mathrm{T}}^{\mathrm{probe}}/p_{\mathrm{T}}^{\mathrm{tag}}$ of the two jets is studied as a function of the probe jet axis ϕ-coordinate. Significant deviations of $1/c$ from one are interpreted as impact of the non-operational module. The same exercise is repeated with the use of the two available corrections and their impact on $1/c$ is compared qualitatively. Jets reconstructed using the anti-k_t algorithm with $R = 0.4$ are used in this study.

3.3.1 Event selection

General jet event selection

Data collected in 2011 are used. The data sample consists of events collected with stable beams only. The events are required to pass data quality requirements of the ATLAS subdetectors used for the jet reconstruction. In addition, the following event selection criteria are used:

- Number of tracks associated to the hardest primary vertex in the event must be greater than one. The hardest vertex is identified as the one with highest $\sum p_{\mathrm{T}}^2$ of associated tracks.
- All the event information must be available.

Luminosity corresponding to the lowest unprescaled trigger is 4.5 fb^{-1} [13].

Dijet event selection

From the general jet data sample defined in the previous section the dijet events are extracted with a set of criteria described in [42]. These criteria are chosen to select events with two highest-p_{T} jets that are back-to-back in the transverse

plane. All other jets (if any) are required to be suppressed. Only jets tagged as not Ugly[1] and Good with the Tight jet cleaning criterion [50] are considered.

Events are triggered by central jet triggers according to the arithmetic mean of the two highest-p_{T} jets transverse momenta, $p_{\mathrm{T}}^{\mathrm{avg}}$. The trigger scheme adopted is shown in Tab. 3.1. Just one trigger is used for each $p_{\mathrm{T}}^{\mathrm{avg}}$ bin. In each event, the

$p_{\mathrm{T}}^{\mathrm{avg}}$ [GeV]	trigger	p_{T} threshold [GeV]
75 - 100	EF_j40_a4tc_EFFS	40
100 - 130	EF_j55_a4tc_EFFS	55
130 - 170	EF_j75_a4tc_EFFS	75
170 - 220	EF_j100_a4tc_EFFS	100
220 - 300	EF_j135_a4tc_EFFS	135
300 - 400	EF_j180_a4tc_EFFS	180
400 -	EF_j240_a4tc_EFFS	240

Table 3.1: The trigger scheme used for the selection of dijet events. The thresholds correspond the jet energy at the EM scale.

azimuthal angle difference between the two highest-p_{T} jets is required to be large: $\Delta\phi > 2.5$ rad. The requirements on the remaining jets are imposed according to their η:

- From jets with $\eta < 2.5$ (within the ID acceptance) and with JVF > 0.6 the highest-p_{T} jet is chosen and required to have $p_{\mathrm{T}} < \max(0.25 p_{\mathrm{T}}^{\mathrm{avg}}, 12\ \mathrm{GeV})$. JVF is an abbreviation for "Jet Vertex Fraction" and, roughly speaking, it has the meaning of the fraction of a jet transverse momentum originating in the hardest vertex in the event. For details on JVF see [42].

- From jets with $\eta > 2.5$ (outside the ID acceptance) the highest-p_{T} jet is chosen and required to have $p_{\mathrm{T}} < \max(0.20 p_{\mathrm{T}}^{\mathrm{avg}}, 10\ \mathrm{GeV})$.

3.3.2 Monte Carlo

Section 2.3 describes general principles of the ATLAS MC simulation. This section provides details related to the MC used for the dijet study.

Events are generated with Pythia 6.425 [35] with the Perugia 2011 tune [51] and the CTEQ 5L PDF set [52]. Since Pythia is a leading-order (LO) generator, there are just two outgoing partons in the HS process. Additional partons are produced by the p_{T}-ordered parton shower process [53], initial state radiation (ISR), final state radiation (FSR) and UE that are factorized from the HS. Therefore, more than two jets often occur in the final state.[2] The event generation is split into eight samples (called J1, J2,..., J8) according to the highest-p_{T} of a parton in the event, $\hat{p}_{\mathrm{T}}$. This separation of different p_{T} regions is done to generate sufficient statistics in each region while keeping the total number of generated events reasonable. Each JX sample gets different weight when they are merged.

[1] Ugly jets are seeded by real energy deposits that are located in problematic calorimeter regions. A jet is considered as ugly if $\mathrm{BCH}_{\mathrm{cor,\,cell}} > 0.5$ or the EM energy fraction deposited in the Tile gap scintillators $f_{\mathrm{TileGap3}} > 0.5$ [49]

[2] At the particle level, further jet seeds can be produced by hadronization.

The weight is equal to the cross-section divided by the number of used events in each sample (see Tab. 3.2).

sample	p_{T}-range [GeV]	σ [pb]	# events generated	# events used
J1	17 - 35	$5.2454 \cdot 10^{8}$	2799546	1806340
J2	35 - 70	$3.0399 \cdot 10^{7}$	3799691	2543522
J3	70 - 140	$1.6095 \cdot 10^{6}$	7597518	7587923
J4	140 - 280	$6.6283 \cdot 10^{4}$	11391127	11379420
J5	280 - 560	$1.9253 \cdot 10^{3}$	19495044	19477588
J6	560 - 1020	$3.1136 \cdot 10^{1}$	13990439	13979653
J7	1020 - 2040	$1.3513 \cdot 10^{-1}$	7595551	7590065
J8	2040 -	$5.0943 \cdot 10^{-6}$	1997672	1996287

Table 3.2: p_{T}-ranges, cross-sections and generated statistics corresponding to different JX samples. The used number of events (i.e. after the cut on hard pile-up) is also shown.

Cut on jets with p_{T} larger than $\hat{p}_{\mathrm{T}}$

The addition of pile-up events to the generated hard pp collision yields certain problems. In some cases, a pile-up event contains a higher-p_{T} parton than the generated hard pp collision. When the JX samples are merged, such event gets weight that is much larger than weights assigned to the higher JX sample that generates partons with such p_{T}. Therefore, the resulting jet p_{T} spectrum is deteriorated and the statistical error is increased[3].

Another problem with similar consequences arises at the truth level due to the ISR. A jet can receive contributions from the ISR that raise its p_{T} above $\hat{p}_{\mathrm{T}}$.

To get rid of those events, a veto must be introduced. This section provides a short summary of cuts that were tuned for the presented MC sample. The number of events passing the veto is used in the calculation of the JX sample weights (Tab. 3.2).

As discussed above, the events to veto have a clear signature: a truth or a reconstructed jet p_{T} exceeds $\hat{p}_{\mathrm{T}}$. Such events might affect several variables. The variables studied were truth and reconstructed inclusive jet spectra of the first four JX samples, the ratio of the leading truth jet p_{T} ($p_{\mathrm{T,\,max}}^{\mathrm{truth}}$) and $\hat{p}_{\mathrm{T}}$, the ratio of the leading reconstructed jet p_{T} ($p_{\mathrm{T,\,max}}^{\mathrm{reco}}$) and $p_{\mathrm{T,\,max}}^{\mathrm{truth}}$, the ratio of the two leading reconstructed jets average p_{T} ($p_{\mathrm{T,\,avg}}^{\mathrm{reco}}$) and $p_{\mathrm{T,\,max}}^{\mathrm{truth}}$, the distance $\Delta R(\mathrm{reco},\ \mathrm{truth})$ of the leading reconstructed jet and the leading truth jet. Except for the jet spectra, all the distributions were studied as a function of pile-up, i.e. on MC subsamples corresponding to events with certain NPV (NPV $= 1, 2; 3, 4; 5, 6; 7, 8$). Fig. 3.2 shows some of the distributions for the lowest four JX samples used (J1 - J4). The truth jet spectra in Fig. 3.2a have tails reaching too high-p_{T} regions. Fig. 3.2c shows that there are events with the leading truth jet p_{T} exceeding $\hat{p}_{\mathrm{T}}$ almost three times. As expected, no dependence of the ratio $p_{\mathrm{T,\,max}}^{\mathrm{truth}}/\hat{p}_{\mathrm{T}}$ on pile-up is observed in the figure. On the other hand, the reconstructed jet p_{T} spectra in Fig. 3.2b are affected by the pile-up events a lot. For the J1 sample, the high-p_{T}

[3] A jet with high weight makes the effective number of jets to decrease if it falls in a bin where other jets are assigned much lower weights.

tail of the spectrum exceeds the contributions of J2, J3 and even J4 samples to the total spectrum. This observation is confirmed by Fig. 3.2d that reveals the pile-up dependence of the ratio $p_{\mathrm{T,\,max}}^{\mathrm{reco}}/p_{\mathrm{T,\,max}}^{\mathrm{truth}}$ for values higher than ∼2.

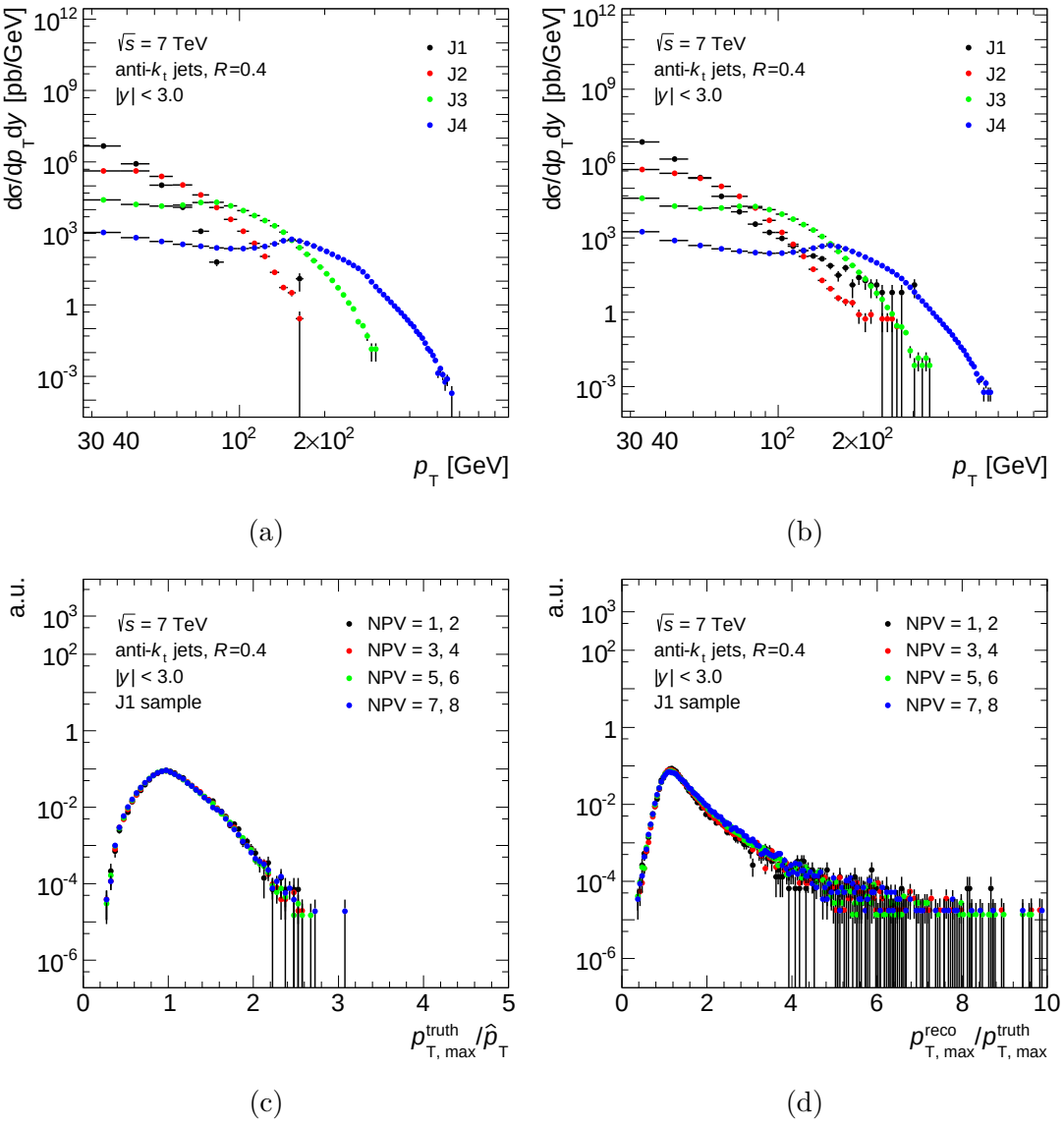

Figure 3.2: Distributions used to tune cuts on MC events with either very hard pile-up collision or a truth jet with too large p_{T} due to ISR. Truth (a) and reconstructed (b) jet spectrum for the samples J1 - J4. Distributions of $p_{\mathrm{T,\,max}}^{\mathrm{truth}}/\hat{p}_{\mathrm{T}}$ (c), $p_{\mathrm{T,\,max}}^{\mathrm{reco}}/p_{\mathrm{T,\,max}}^{\mathrm{truth}}$ (d) for the J1 sample shown for different MC subsamples characterized by NPV.

The cuts used in the measurement are:

- Reject MC event if $p_{\mathrm{T,\,max}}^{\mathrm{truth}}/\hat{p}_{\mathrm{T}} > 2.0$
- Reject MC event if $p_{\mathrm{T,\,max}}^{\mathrm{reco}}/p_{\mathrm{T,\,max}}^{\mathrm{truth}} > 2.0$

Fig. 3.3 shows the truth and reconstructed jet spectra after the application of the above two cuts. The cut on $p_{\mathrm{T,\,max}}^{\mathrm{truth}}/\hat{p}_{\mathrm{T}}$ slightly improves the truth jet spectrum. What concerns the reconstructed jet spectra, significant improvement is seen

for the J1 sample, especially. Without the cuts, its high-p_{T} tail exceeds the contributions of J2, J3 and even J4 samples. This domination of the J1 sample is removed after application of the cuts. Similar but less pronounced behavior is observed for the J2 and J3 samples as well.

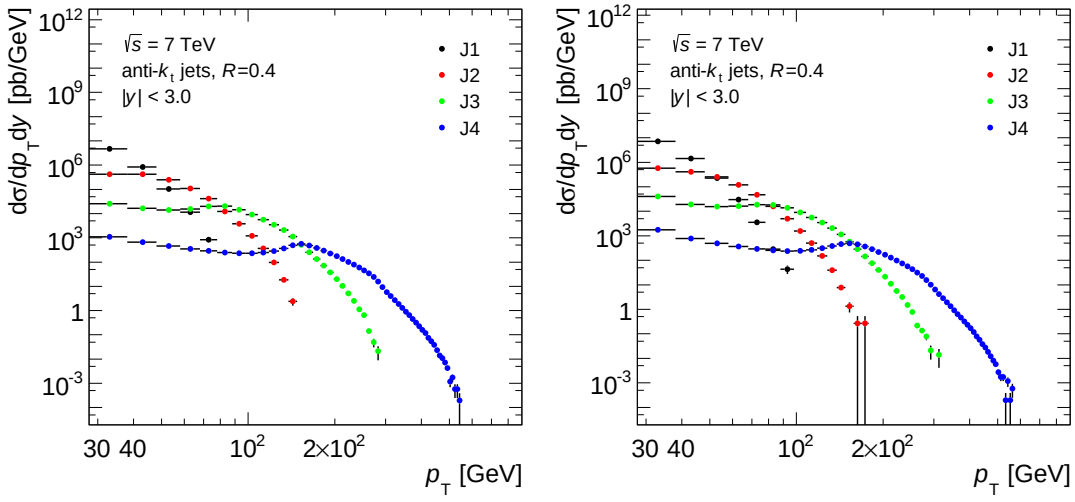

(a) (b)

Figure 3.3: Truth (a) and reconstructed (b) jet spectrum for the lowest four JX samples after application of the cuts on very hard pile-up collision and truth jets with too large p_{T} due to ISR.

3.3.3 Detector defects and their simulation

During the data taking periods E-H, there was a problem with one front-end crate of the LAr calorimeter barrel. As a result, 6 FEBs were non-operational and the corresponding calorimeter area was not read-out. 4 (2) FEBs were related to the second (third) calorimeter layer as numbered according to the increasing distance from the interaction point. The inactive area was $(0.0, 1.475) \times (-0.791, -0.595)$ in the $\eta - \phi$ plane. Jets falling into the region and its vicinity were very poorly reconstructed in the affected periods E-H. After the period H, the 4 FEBs related to the second calorimeter layer were repaired. The remaining 2 non-operational FEBs reading the third layer are not considered as an intolerable defect because the third layer is much thinner than the second one, see Fig. 2.3.

Before and during the 2011 data taking 12 TileCal modules failed. Seven modules faced LVPS failure. Two modules had problems with the HV system and two modules had the IF card disconnected (see Sec. 2.2.3). One module (LBA24) was non-operational in 8 runs in periods D, E. These 12 failures that occurred during the 2011 pp data taking at different dates is summarized in Tab. 3.3.

The detector simulation also includes detector defects that occurred during the 2011 data taking. To describe the evolution of these defects, four different MC periods are generated with different detector conditions. The MC sample corresponding to given MC period is identified by a run number. See Tab. 3.4 for a brief summary of simulated detector defects. Detailed information about which

module	failed on	simulated in MC periods			
LBA11	18.1.2011	180164	183003	186169	189751
LBA22	14.10.2011				189751
LBA24		180164			
LBA54	17.5.2011		183003	186169	189751
LBC02	8.4.2011	180164	183003	186169	189751
LBC07	1.4.2011	180164	183003	186169	189751
LBC11	17.8.2011			186169	189751
LBC25	24.9.2011				189751
LBC32	11.9.2011				189751
LBC50	21.10.2011				
LBC52	18.1.2011	180164	183003	186169	189751
EBC37	19.1.2011	180164		186169	189751

Table 3.3: Dates of failures of 12 TileCal modules. For each module, the information in which MC periods it is simulated as non-operational is provided. Module LBC50 failed at the end of period M and was not simulated as non-operational in MC.

TileCal module is simulated as non-operational in which MC period is in Tab. 3.3. The MC samples get weight according to the luminosity collected during the data

MC run number	data periods	luminosity fraction	LAr defects	TileCal defects
180164	D	3.5 %	-	6 modules
183003	E-H	20.5 %	6 FEBs	5 modules
186169	I-K	24.4 %	2 FEBs	7 modules
189751	L-M	51.6 %	2 FEBs	10 modules

Table 3.4: Brief description of detector defects simulated in four different MC samples. Each sample is assigned a run number for identification and corresponds to a range of data taking periods. The fraction of total luminosity corresponding to the periods is also provided.

taking period that corresponds to the given detector conditions. These weights differ for different triggers. Tab. 3.4 shows the fractions of luminosity taken by the lowest unprescaled single jet trigger EF_j240_a4tc_EFFS in the four periods.

Since the detector conditions were stable in the region used in this study (see below), all the weighs are set to one.

3.4 Results

The studied non-operating TileCal module is LBA11. It spans the region $(0.0, 1.0) \times (0.98, 1.08)$ in the $\eta \times \phi$ plane. This module is chosen because it did not operate all the 2011 data taking period (therefore, maximum statistics was taken) and the opposite region (in the ϕ-coordinate) did not contain any severe problem discussed in Sec. 3.3.3.

The tag jets are required to point into the pseudorapidity region $|\eta| < 1.6$ covered by TileCal; the transition region $0.8 < |\eta| < 1.2$ between LB and EB is excluded. Probe jets with $0.0 < \eta < 0.8$ are selected.

Fig. 3.4 shows the dependence of the relative jet response as a function of the probe jet axis ϕ-coordinate. Four different $p_{\mathrm{T}}^{\mathrm{avg}}$ bins are displayed. If no

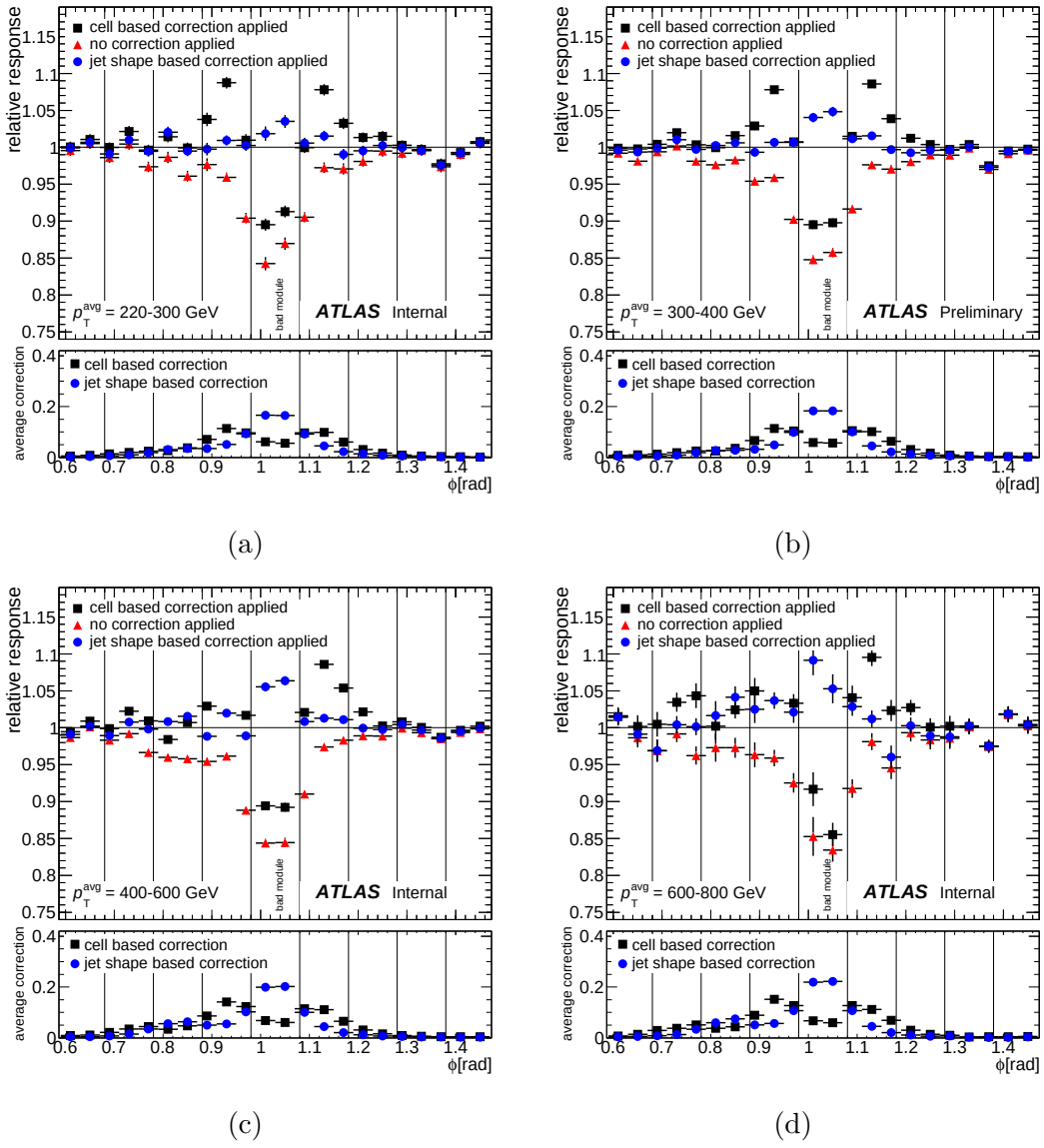

Figure 3.4: The relative jet p_{T} response measured in data using dijet events with one jet falling into an operational calorimeter region and the other jet probing the vicinity of one chosen non-operational TileCal module. Four different $p_{\mathrm{T}}^{\mathrm{avg}}$ bins are shown. The vertical lines represent the TileCal module edges. Jets are calibrated with the EM+JES scheme.

bad channel correction is used, the probe jet p_{T} is underestimated by $\sim$15 % if the jet axis points to the non-operational module. The probe jet p_{T} is also underestimated if its axis points to the region $\Delta\phi \sim \pm 0.1$ around the module but no more than by $\sim$5 %. If $\mathrm{BCH}_{\mathrm{cor,\,cell}}$ is used to correct the probe jet energy then its p_{T} is underestimated by $\sim$10 % in the non-operational module and it is overcorrected by up to $\sim$10 % in the module's vicinity ($\Delta\phi \sim \pm 0.1$ around the

module). $\mathrm{BCH}_{\mathrm{cor,\,jet}}$ yields an average overcorrection by $\sim$5 % (depending on $p_{\mathrm{T}}^{\mathrm{avg}}$) in the problematic module but just a very low over-/under-estimation (no more than $\sim$2 %) in its vicinity.

3.4.1 Application of $\mathrm{BCH}_{\mathrm{cor,\,jet}}$ to jets on the LCW scale

As stated above, $\mathrm{BCH}_{\mathrm{cor,\,jet}}$ is designed to correct energies of jets at the EM scale. A test of its performance when applied on jets at the LCW scale[4] is done. Fig. 3.5 shows the results for data. The features observed are similar to those seen in the previous section. The overcorrection of jets falling in the dead module is even slightly lower in the present case. In total, the performance of $\mathrm{BCH}_{\mathrm{cor,\,jet}}$ is better than that of the default correction for LCW jets, $\mathrm{BCH}_{\mathrm{cor,\,cell}}$, which is also shown in Fig. 3.5.

Fig. 3.6 shows the comparison of the relative jet response $1/c$ in data with MC when $\mathrm{BCH}_{\mathrm{cor,\,cell}}$ is used. MC reasonably describes all the effects mentioned above. MC also succeeds in the description of the relative jet response when $\mathrm{BCH}_{\mathrm{cor,\,jet}}$ is used. It is shown in Fig. 3.7. For jets calibrated with the EM+JES scheme, the comparison of MC with data is shown in Appendix A. Again, MC describes the effects observed in data reasonably well.

[4] I.e. jets built from the locally calibrated topoclusters.

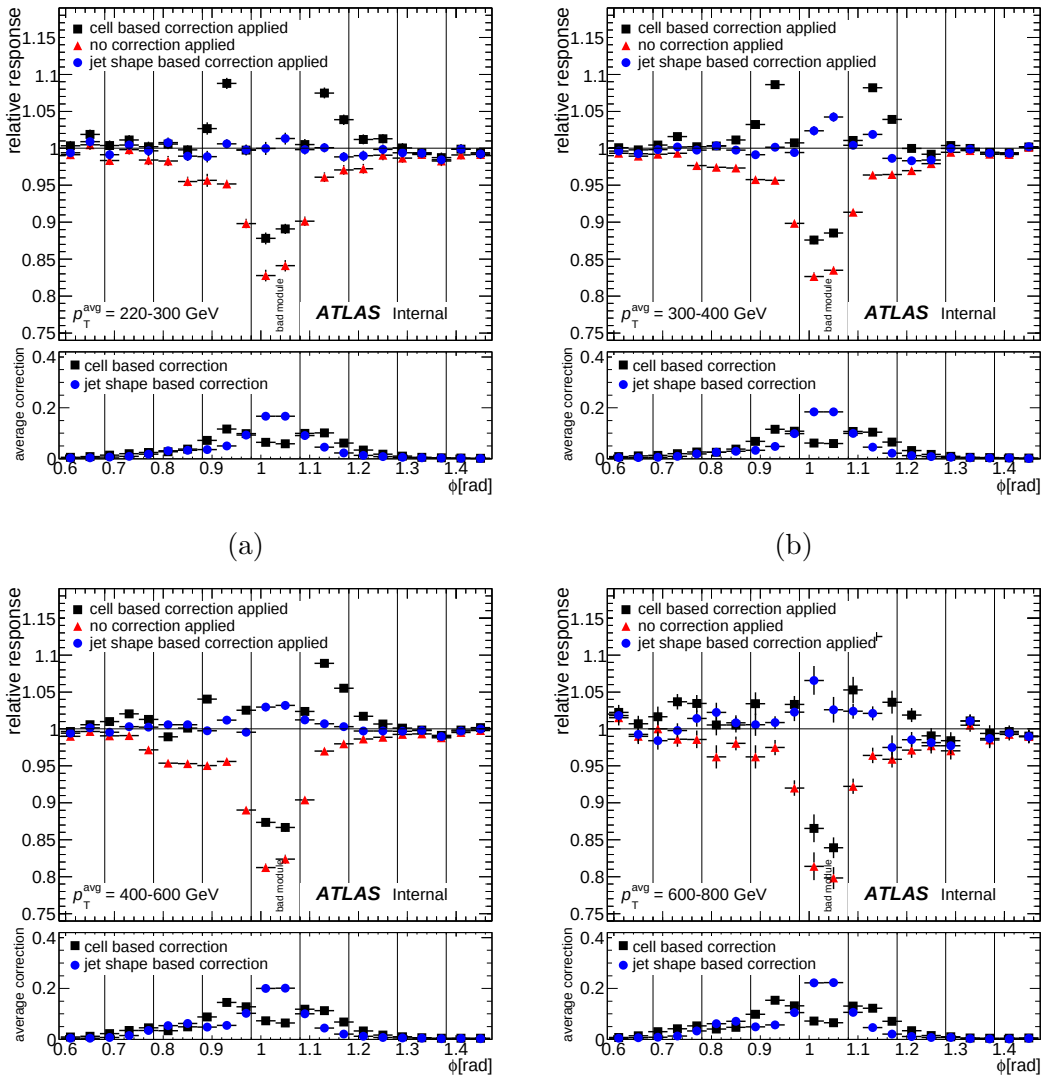

Figure 3.5: The relative jet p_{T} response measured in data using dijet events with one jet falling into an operational calorimeter region and the other jet probing the vicinity of one chosen non-operational TileCal module. Jets are built from locally calibrated topoclusters and calibrated with the LCW+JES scheme. $\mathrm{BCH}_{\mathrm{cor,\,jet}}$ is applied on jets at the LCW scale. Four different $p_{\mathrm{T}}^{\mathrm{avg}}$ bins are shown. The vertical lines represent the TileCal module edges.

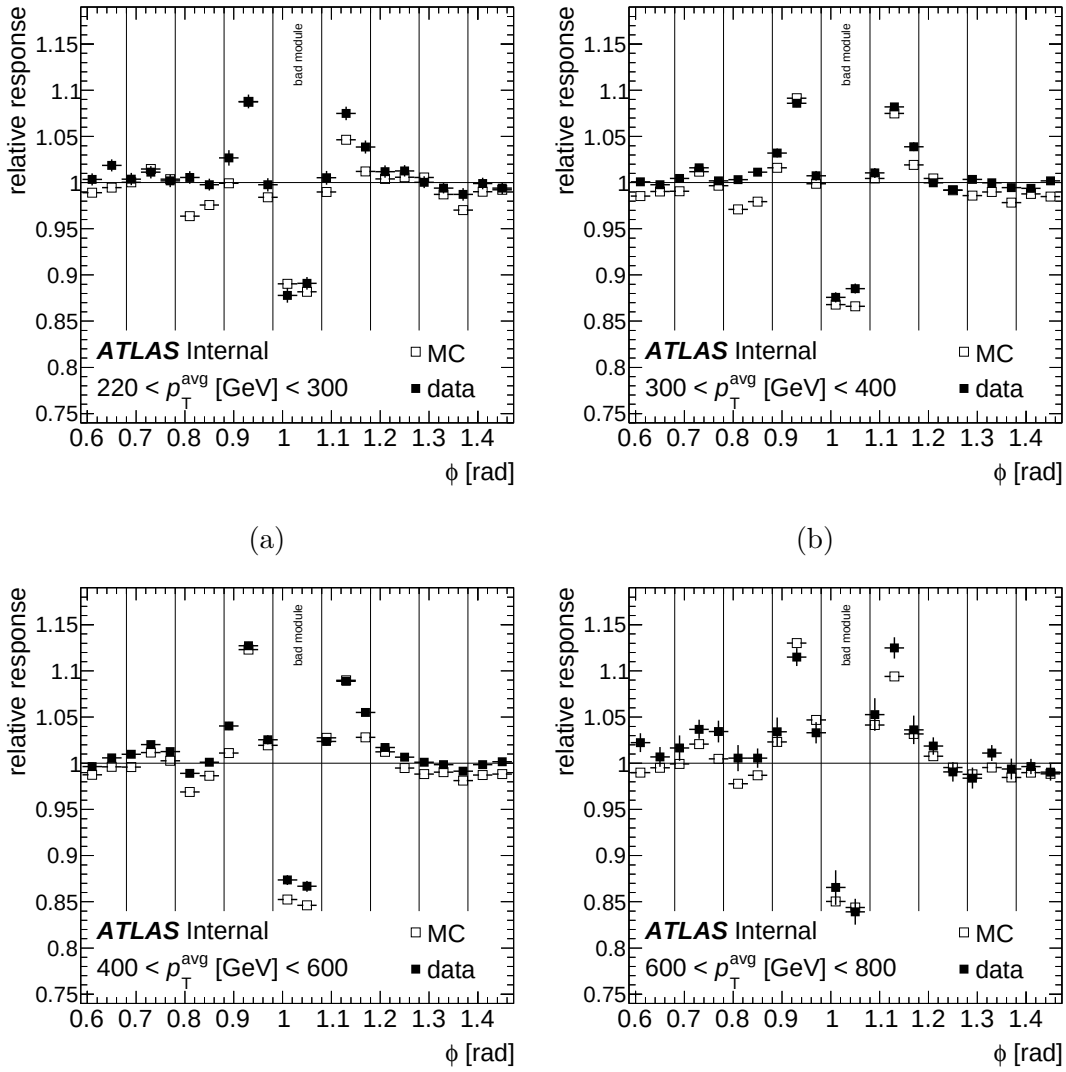

Figure 3.6: The relative jet p_{T} response measured in dijet events with one jet falling into an operational calorimeter region and the other jet probing the vicinity of one chosen non-operational TileCal module. Jets are built from locally calibrated topoclusters and calibrated with the LCW+JES scheme. $\mathrm{BCH}_{\mathrm{cor,\,cell}}$ is used to correct the probe jet energy. Four different $p_{\mathrm{T}}^{\mathrm{avg}}$ bins are shown for both MC and data. The vertical lines represent the TileCal module edges.

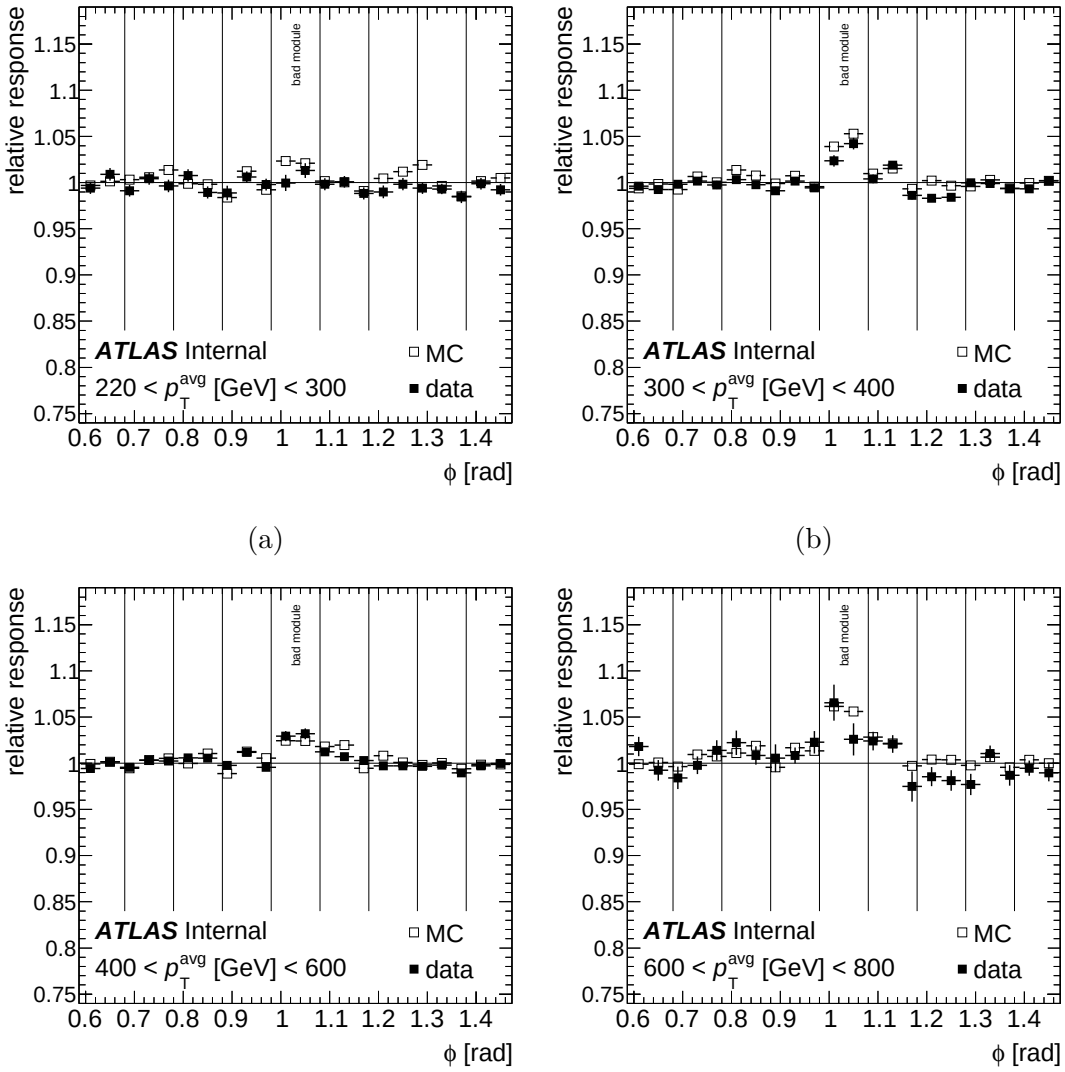

Figure 3.7: The relative jet p_{T} response measured in dijet events with one jet falling into an operational calorimeter region and the other jet probing the vicinity of one chosen non-operational TileCal module. Jets are built from locally calibrated topoclusters and calibrated with the LCW+JES scheme. $\mathrm{BCH}_{\mathrm{cor,\,jet}}$ is used to correct the probe jet energy. Four different $p_{\mathrm{T}}^{\mathrm{avg}}$ bins are shown for both MC and data. The vertical lines represent the TileCal module edges.

4. Inclusive jet cross-section measurement

The inclusive jet cross-section measurement is one of the basic tests of QCD. In the past, it was measured by various experiments at different centre-of-mass energies of different colliding particles, with various choices of the jet algorithm. The most recent results come from the LHC experiments ALICE [54], CMS [55, 56] and ATLAS [57, 58, 59].

This thesis presents the ATLAS inclusive jet cross-section results at $\sqrt{s} = 7$ TeV with the full 2011 integrated luminosity of 4.5 fb^{-1} and with jets reconstructed using the anti-k_t jet algorithm with $R = 0.4$ and $R = 0.6$. ATLAS measured this cross-section using the 2010 data sample of 37 pb^{-1} already [57]. The main advantages of the 2011 measurement [59] are higher integrated luminosity and improved jet energy calibration (see Sec. 2.4.3). The main challenge is higher pile-up.

4.1 Observable definition and theoretical predictions

Jets described in Sec. 2.4.2 are used in the measurement. Three different types of jets are distinguished according to the objects used as input to the jet algorithm:

- Parton-level jets: final-state partons.
- Particle-level jets: stable particles (see Sec. 2.3) including muons and neutrinos.
- Detector-level jets: locally calibrated calorimeter topoclusters, see Sec. 2.4.

The resulting spectra are provided at the particle-level where they are compared against theoretical predictions.

The measurement covers the region delimited by $|y| < 3.0$ and 100 GeV $< p_T \lesssim 2$ TeV. Below 100 GeV, the cross-section is precisely measured with the 2010 data under lower pile-up conditions. Since pile-up especially affects these low-p_T jets, it is decided not to remeasure the cross-section in this region in 2011 data. 2 TeV is the highest reach of the 2011 data sample. The region $|y| < 3.0$ is chosen because it is covered by the central jet triggers that span the pseudorapidity region $|\eta| < 3.2$. Second reason is pile-up, that becomes more important for jets with high pseudorapidities. Since the 2010 measurement goes up to $|y| = 4.4$ it is decided to stay within the $|y| = 3.0$ boundary in 2011.

4.1.1 Theoretical predictions

Theoretical predictions for the cross-section of the HS process are calculated at next-to-leading-order (NLO) with the NLOJET++ 4.1.2 software [60]. The calculated cross-section is convoluted with PDFs by the APPLGRID framework [61]. The PDF sets used are CT10 [62], MSTW2008 [63], NNPDF 2.1 [64, 65], ABM 11

with five quark flavours [66] and HERAPDF 1.5 [67]. The renormalization and factorization scale are set to the highest-p_{T} of a jet in the event.

The resulting parton-level inclusive jet cross-section is corrected for the electroweak (EW) radiative effects. These EW corrections are calculated following the same technique as [68] and by the same authors. The corrections are important at the low-$|y|$ and high-p_{T} region ($|y| \lesssim 1.0$, $p_{\mathrm{T}} \gtrsim 1$ TeV) where they reach up to 15 %. They are derived as multiplicative factors using the LO QCD predictions.

Non-perturbative corrections

NLOJET++ with APPLgrid predicts the inclusive jet cross-section of the HS process, with partons in the initial and final state. Modifications due to the UE and hadronization are missing. They are introduced by the non-perturbative (NP) corrections. These corrections are bin-by-bin multiplicative factors derived from the LO MC generators Pythia 6.427, Pythia 8.175 [36] and Herwig++ 2.6.3 with various underlying event tunes. For each generator and tune the corrections are calculated as a ratio of two spectra: inclusive jet cross-section generated with UE and hadronization turned on vs. the cross-section generated with these two effects turned off. The nominal NP correction is derived from Pythia 6.427 with the Perugia 2011 tune [51].

Uncertainty of the theoretical predictions

The theoretical predictions have the following components: HS cross-section convoluted with PDFs, EW correction and NP correction. The following paragraph describes the considered uncertainty on each component.

The HS cross-section convoluted with PDFs has uncertainty due to the renormalization and factorization scale choice, experimental (plus parametrization, eventually) uncertainty of the PDFs and the uncertainty on $\alpha_{\mathrm{S}}(M_Z^2)$. The uncertainties are estimated by the prescriptions given by each PDF set and by PDF4LHC [69]. The uncertainty related to the choice of the renormalization and factorization scale is estimated by varying the scales [57]. The two scales are multiplied by several combinations of factors of 2 and 1/2, rederiving the parton-level cross-section. The envelope of all those variations is taken as the uncertainty. The $\alpha_{\mathrm{S}}(M_Z^2)$ uncertainty is evaluated with the use of alternative PDF sets derived with varied $\alpha_{\mathrm{S}}(M_Z^2)$ values.

The uncertainty of the NP correction is estimated as an envelope of five different predictions obtained with different MC generators and tunes: Pythia 6.427 with Perugia 2011, Pythia 6.427 with AUET2B [70], Pythia 8.175 with 4C [71], Pythia 8.175 with AU2 [72] and Herwig++ 2.6.3 with UE-EE-3 [73]. The results for both $R = 0.4$ and $R = 0.6$ jets and for three representative rapidity bins are shown in Fig. 4.1.

The EW correction is assigned no uncertainty as proposed by the authors because it is currently not available. An estimate of the uncertainty could be obtained by applying the EW correction to a LO spectrum instead of to the NLO one, schematically:

$$\mathrm{NLO} + \mathrm{EW} \times \mathrm{LO} \qquad \text{instead of} \qquad \mathrm{NLO} + \mathrm{EW} \times \mathrm{NLO} \tag{4.1}$$

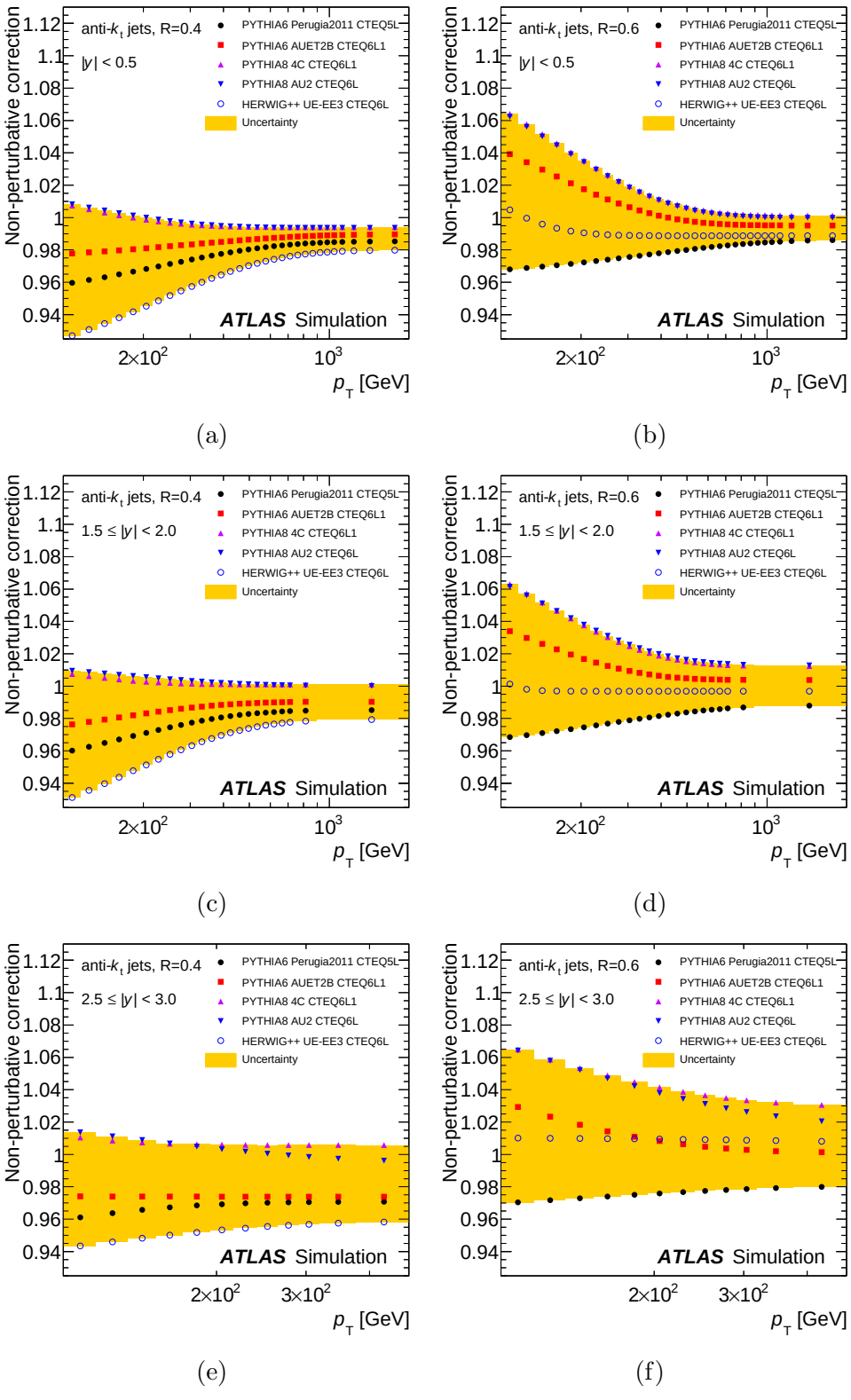

Figure 4.1: The NP correction with its uncertainty in three representative y-bins for anti-k_t jets with $R = 0.4$ (a), (c), (e) and with $R = 0.6$ (b), (d), (f). The nominal correction is derived from PYTHIA 6 with the Perugia 2011 tune. The asymmetric uncertainty is taken as an envelope of the different predictions plotted around the nominal one.

This alternative approach comes from the fact that the EW correction is derived by adding the EW effects to the LO QCD prediction. The difference between the two approaches is the highest in the lowest-y, highest-p_{T} bin where it reaches 3% (4%) for the $R = 0.4$ (0.6) jets. However, the uncertainty evaluated in this way could be overestimated according to the authors.

The total uncertainty of the theoretical predictions is a quadrature sum of the PDFs, α_{S}, scale and NP correction uncertainties. It is shown in Fig. 4.2 with its components for three representative y-bins for the anti-k_{t} jets with both $R = 0.4$ and 0.6. The NP correction uncertainty is not added in these figures.

Note on the non-perturbative correction

After the publication of the paper [59], it was discovered that the nominal non-perturbative correction evaluated with Pythia 6.427 and Perugia 2011 tune suffers from a bug in the tune parameter settings [74]. Some of the parameters were not set according to the Perugia 2011. In particular, the UE was switched off. On top of that, there is a bug in Pythia 6.427 leading to a strong suppression of final-state radiation from a gluon in $q^* \to qg$ processes, see [75].

After these observations, a new non-perturbative correction is evaluated with Perugia 2011 tune parameters set correctly and with a newer version of Pythia 6.428 where the bug is fixed. The result is compared with the published one in Fig. 4.3. A maximum difference of 2 % (6 %) is observed for anti-k_{t} jets with $R = 0.4$ (0.6). The difference is most pronounced in the low-p_{T} region. The high-p_{T} region is not affected by more than 1 % in any y-bin.

4.1.2 Powheg prediction

An alternative way for the computation of the theoretical predictions at NLO is the Powheg [39, 40, 41, 76, 77] program. In the presented analysis, Powheg is interfaced to Pythia to include parton showers, UE and hadronization. Other MC generators are often used as well. Here, only Pythia with two different tunes is used: AUET2B and Perugia 2011. Thus, the Powheg prediction is calculated with the NLO+LL precision. The most delicate part of the event generation is the matching between the HS process and the parton shower program. Since both parts provide gluon emissions, a matching scale limits the parton shower to avoid double-counting. Unfortunately, there is no clear procedure for the uncertainty estimation of the Powheg prediction. Therefore, a quantitative comparison of Powheg with data is impossible.

Since the output of Powheg is at the particle-level, no NP corrections need to be applied. The QCD-based Powheg results are corrected for the EW radiative effects, similarly to the case of the NLOJET++ predictions.

4.2 Data and Monte Carlo

The data and MC simulation used are the same as in Chap. 3. Here, only the treatment specific to the inclusive jet cross-section analysis is described.

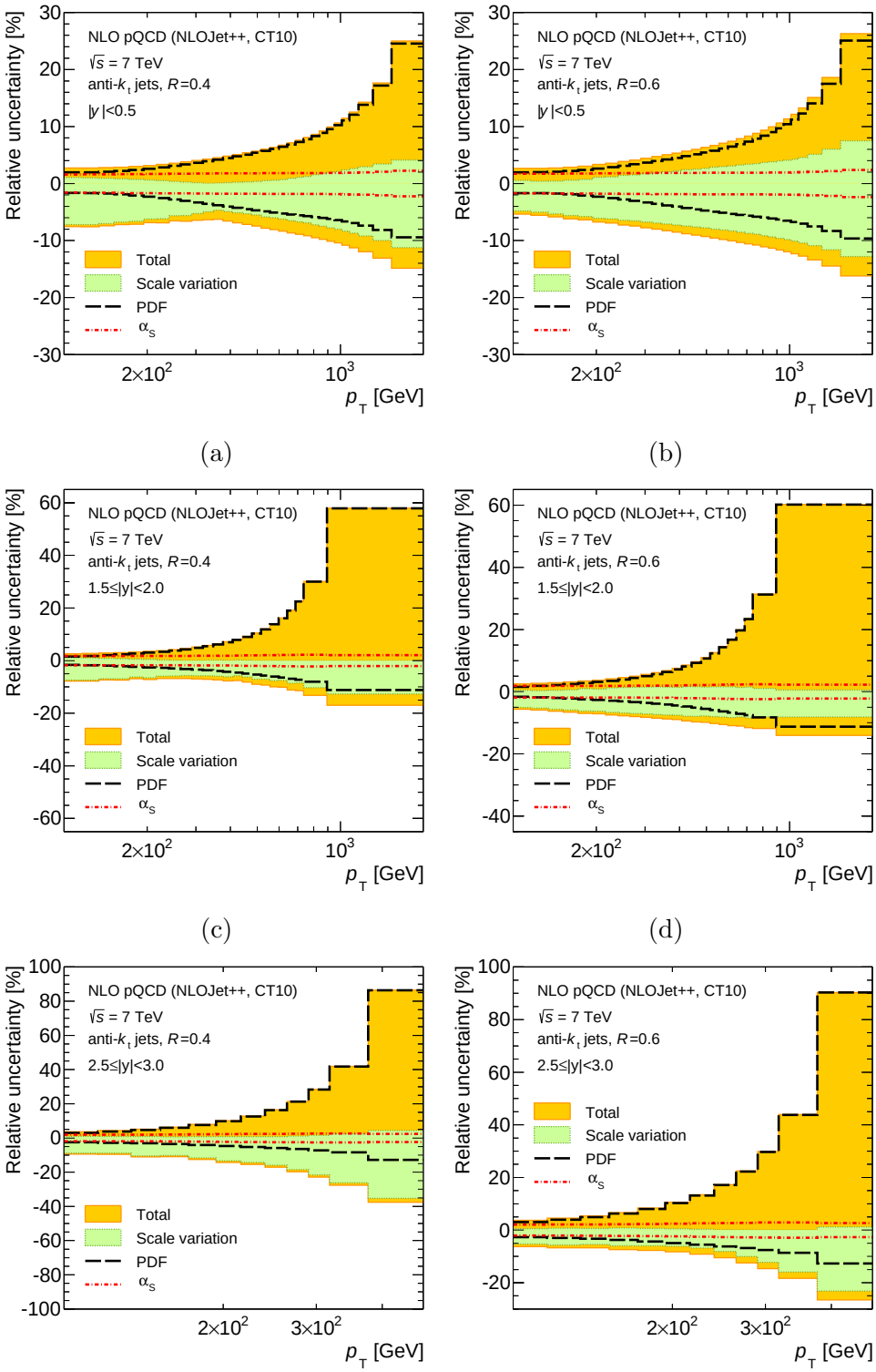

Figure 4.2: The components of the theoretical uncertainty in three selected y-bins for anti-k_t jets with $R = 0.4$ (a), (c), (e) and with $R = 0.6$ (b), (d), (f). The sources considered here are due to the PDF, α_S and renormalization/factorization scales choice. The total uncertainty is a quadrature sum of these three components. The NP correction uncertainty is not included in this figure.

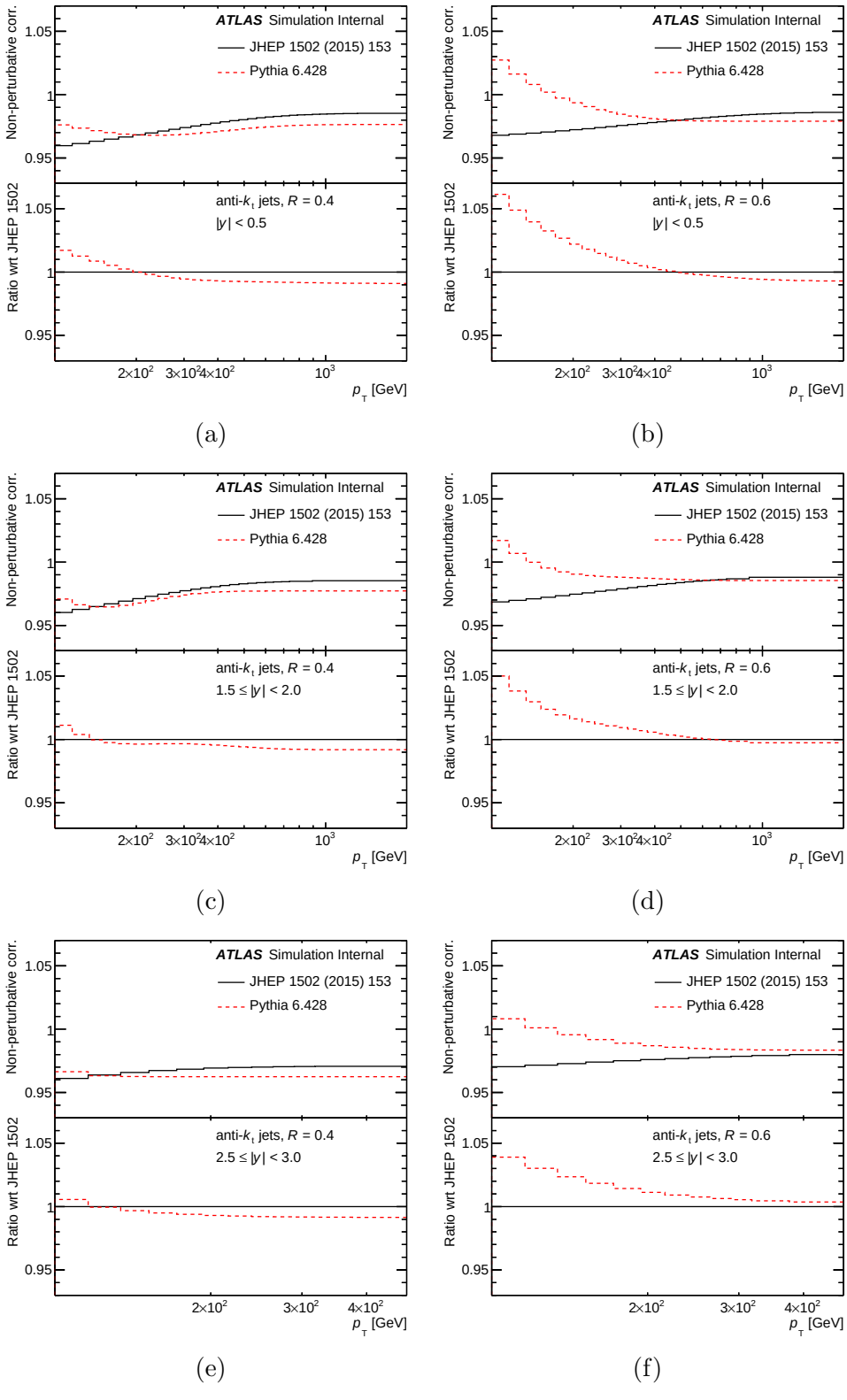

Figure 4.3: Comparison of the published nominal NP correction with the updated one. In each figure, the top plot shows the non-perturbative corrections and the bottom one displays their ratio. Three representative y-bins for anti-k_t jets with $R = 0.4$ (a), (c), (e) and with $R = 0.6$ (b), (d), (f) are shown.

p_{T} [GeV]	trigger	p_{T} threshold [GeV]
0 - 56	EF_j10_a4tc_EFFS	10
56 - 63	EF_j15_a4tc_EFFS	15
63 - 84	EF_j20_a4tc_EFFS	20
84 - 103	EF_j30_a4tc_EFFS	30
103 - 145	EF_j40_a4tc_EFFS	40
145 - 166	EF_j55_a4tc_EFFS	55
166 - 216	EF_j75_a4tc_EFFS	75
216 - 330	EF_j100_a4tc_EFFS	100
330 - 365	EF_j135_a4tc_EFFS	135
365 - 460	EF_j180_a4tc_EFFS	180
460 -	EF_j240_a4tc_EFFS	240

Table 4.1: The trigger scheme used for the jet selection. The thresholds correspond the EM scale jet energy.

4.2.1 Data

The data used and the basic event selection criteria are the same as in Sec. 3.3.1.

4.2.2 Jet selection

Only jets tagged as not Ugly (see Sec. 3.3.1) and Good with the Medium jet cleaning criterion [50] are used.

A trigger decision is checked for each jet in an event separately. Different triggers are used for different p_{T} ranges, see Tab. 4.1. Each trigger is required to be at least 99 % efficient on the p_{T} range it covers.

Due to the problems with 6 FEBs in the LAr calorimeter barrel, jets falling into the area $(-0.1, 1.5) \times (-0.88, -0.50)$ are discarded from the measurement. They are removed in both data and MC regardless of the period.

As described in Sec. 3.1, there were 11 non-operational TileCal modules at the end of 2011 pp-collision data taking. Based on the results of Chap. 3, the $\mathrm{BCH}_{\mathrm{cor,\,jet}}$ bad channel energy correction is used for jets falling in the $|\eta| < 1.5$ region. Outside this region the default correction $\mathrm{BCH}_{\mathrm{cor,\,cell}}$ is kept. See Sec. 4.5.4 for the justification of this treatment.

4.2.3 Monte Carlo

The MC used for the derivation of the jet calibration is based on Pythia version 6.425 with the AUET2B tune. The MC used in the inclusive jet cross-section analysis is the same as in Sec. 3.3.2. It employs Pythia version 6.425 with the Perugia 2011 tune.

Pile-up reweighting

As mentioned in Sec. 2.3, the pile-up conditions in MC are tuned to be close to those in data. However, there is still some difference between the distributions of the pile-up related variables (μ_{avg}, NPV) between MC and data. For this reason, each MC jet is assigned a weight whose goal is to match the distribution of one

variable in MC to data exactly. This procedure is called pile-up reweighting (of the MC).

In the inclusive jet cross-section analysis, the chosen variable is μ_{avg}. Its distribution in data and MC before the pile-up reweighting is shown in Fig. 4.4 for the jet samples triggered by the lowest and the highest trigger used. The NPV distribution is also shown in the figure. The MC μ_{avg} distribution models the data reasonably well in the case of the unprescaled trigger but there is a large difference between μ_{avg} distributions corresponding to the lowest trigger used in the analysis. Qualitatively very similar behaviour is observed for the NPV distributions as well. The reweighting is done separately for p_{T}-ranges that

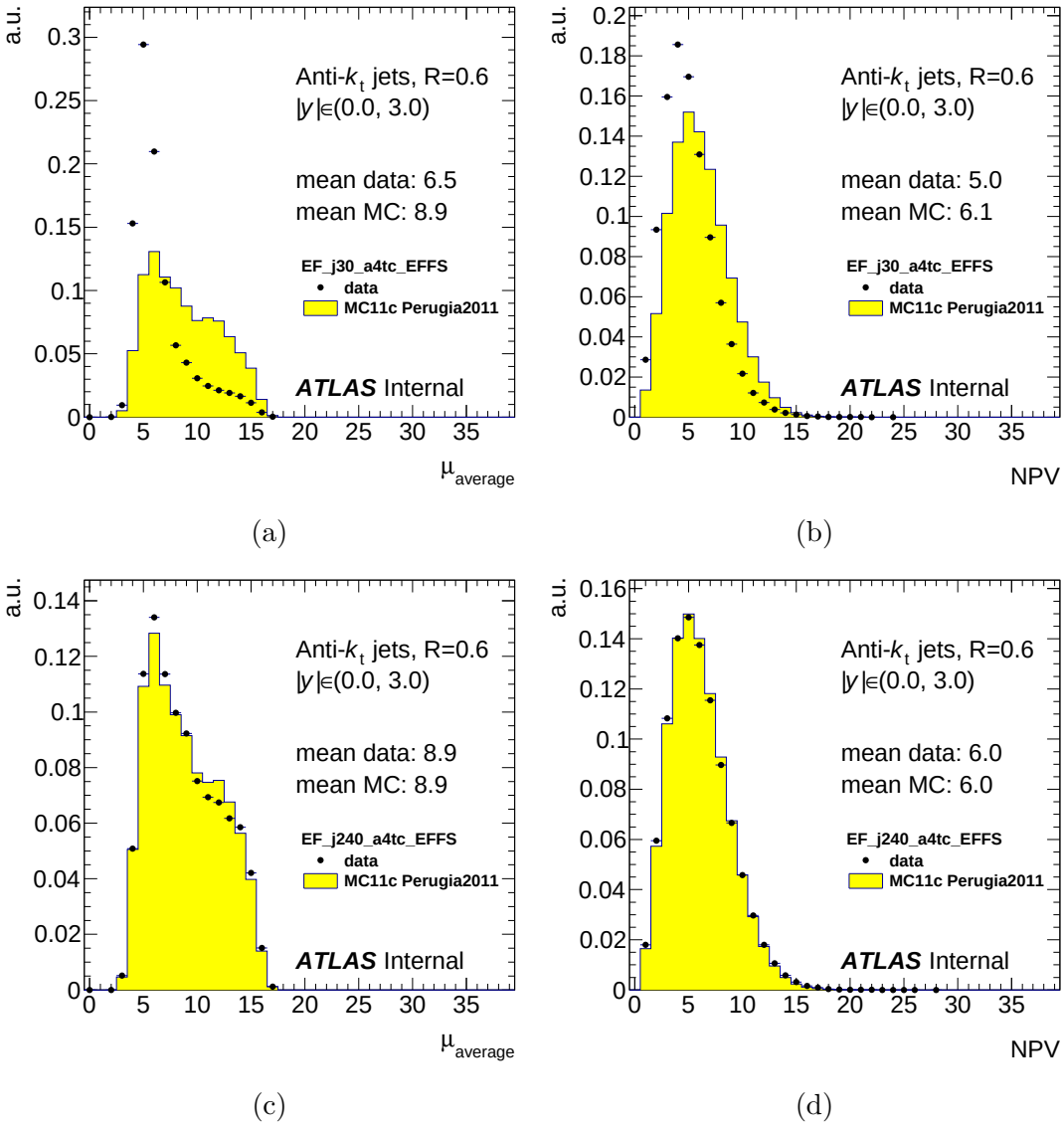

Figure 4.4: The distributions of μ_{avg} (a, c) and NPV (b, d) in data and MC before the pile-up reweighting. All the distributions are normalized to the integral. They correspond to the inclusive sample of anti-k_{t} jets with $R = 0.6$ triggered by the lowest (a, b) and the highest (c, d) triggers used in the analysis. The highest trigger is unprescaled.

correspond to different triggers. This differentiation must be done because of

important trigger prescales evolution during 2011. See Fig. 4.5 that shows the normalized distribution of jets as a function of data taking period for several p_{T} ranges.

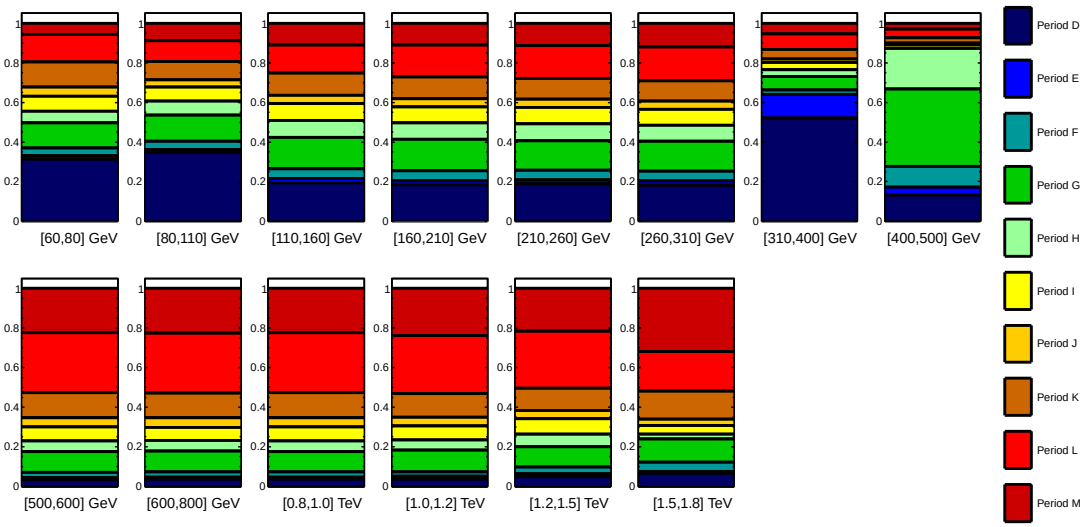

Figure 4.5: Normalized distribution of jets as a function of data taking period for several p_{T} ranges. For each p_{T} range and each period, the fraction of jets falling into the bin and coming from the period is plotted.

In the reweighting, each MC jet is assigned a weight whose purpose is to bring the MC μ_{avg} distribution to agreement with data for the p_{T}-range the jet belongs to. The weights are derived as bin-by-bin ratios of the μ_{avg} distribution in data and MC. The distributions are split into 40 bins with width equal to 1. They are filled for each jet in an event if the corresponding trigger fired.

Fig. 4.6 shows the MC distributions of μ_{avg} and NPV after pile-up reweighting for two p_{T}-ranges denoted by the trigger used for jets falling in them. Since the jets are reweighted according to μ_{avg}, the NPV distributions in data and MC do not exactly overlap. However, the agreement is improved for them as well.

Distributions of kinematical variables

The unfolding procedure (Sec. 4.3) relies on the assumption of a decent modeling of the measured spectra by the MC. Distributions of several kinematical variables are compared between data and MC to check that MC models data well. Fig. 4.7 shows the detector-level distributions of jet y, ϕ and p_{T} for anti-k_{t} jets with $R = 0.6$. Fig. 4.8 compares the $\eta-\phi$ jet distributions in MC and data. Reasonable agreement is observed for all the distributions which leads to the conclusion that the MC can be used for the unfolding.

4.3 Unfolding

Unfolding is a procedure that deconvolutes detector effects from the measured spectra. There are several different unfolding implementations like e.g. Singular Value Decomposition (SVD) [78], iterative Bayes-inspired regularized unfolding [79, 80] or Iterative, dynamically stabilized (IDS) method of data unfold-

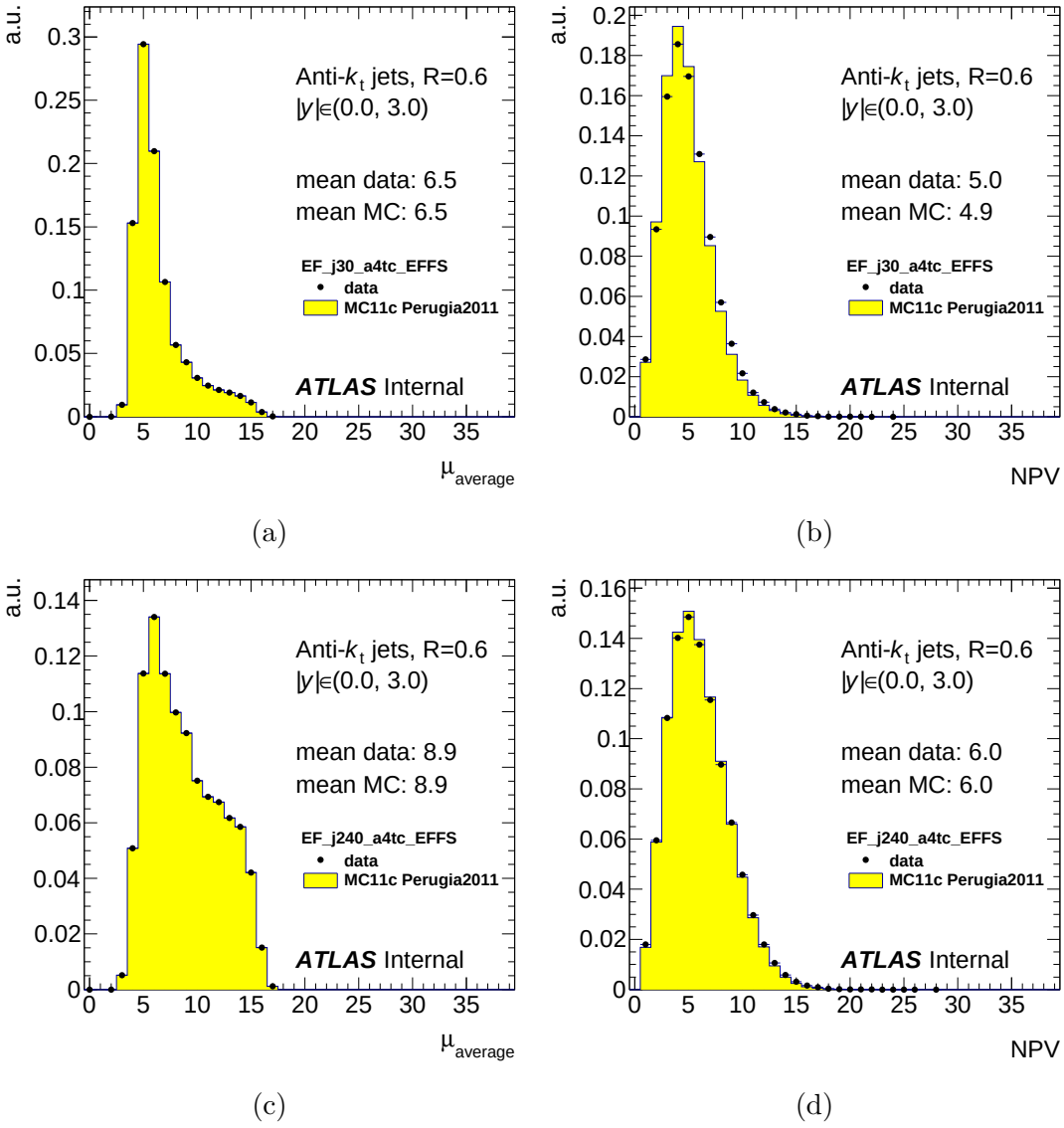

Figure 4.6: The distributions of μ_{avg} (a, c) and NPV (b, d) in data and MC after the pile-up reweighting. All the distributions are normalized to the integral. They correspond to the inclusive sample of anti-k_t jets with $R = 0.6$ triggered by the lowest (a, b) and the highest (c, d) triggers used in the analysis.

ing [81, 82]. The presented analysis uses the IDS method because it yields the lowest unfolding bias.

This section briefly explains the main ideas of IDS and presents the construction and tests of its inputs.

4.3.1 IDS method of data unfolding

The IDS method relies on a detailed MC description of the detector effects and a decent modeling of the truth spectra by the MC event generator. If these two conditions are fulfilled, it is possible to build a transfer matrix (TM) whose

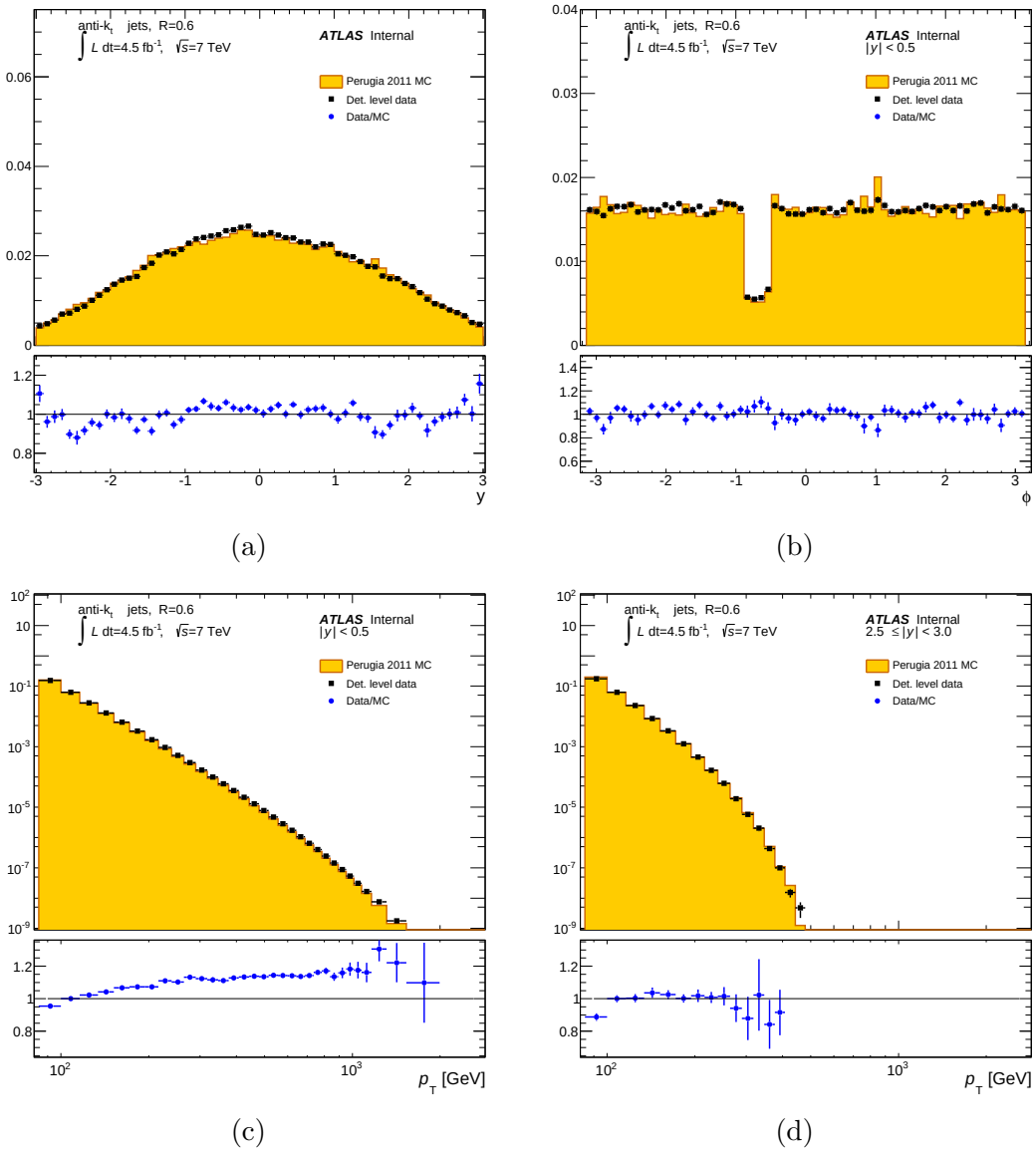

Figure 4.7: The detector-level distributions of jet y (a) and ϕ (b). Both are integrated over jet p_{T}. The ϕ distribution is restricted to jets with $|y| < 0.5$. The dip in the ϕ distribution corresponds to the rejection of jets falling into the problematic LAr area (Sec. 4.2.2). The jet p_{T} spectrum is shown for the lowest $|y| < 0.5$ (c) and the highest $2.5 \le |y| < 3.0$ (d) y-bin. All the distributions correspond to anti-k_{t} jets with $R = 0.6$.

element A_{ij} is the number of events[1] generated in the bin j and reconstructed in the bin i. From the TM, both the folding P_{ij} and the unfolding matrix $\tilde{P}_{ij}$ are

[1]In the case of the inclusive jet cross-section, it is not number of events but jets. This particularity has no impact on the described procedure.

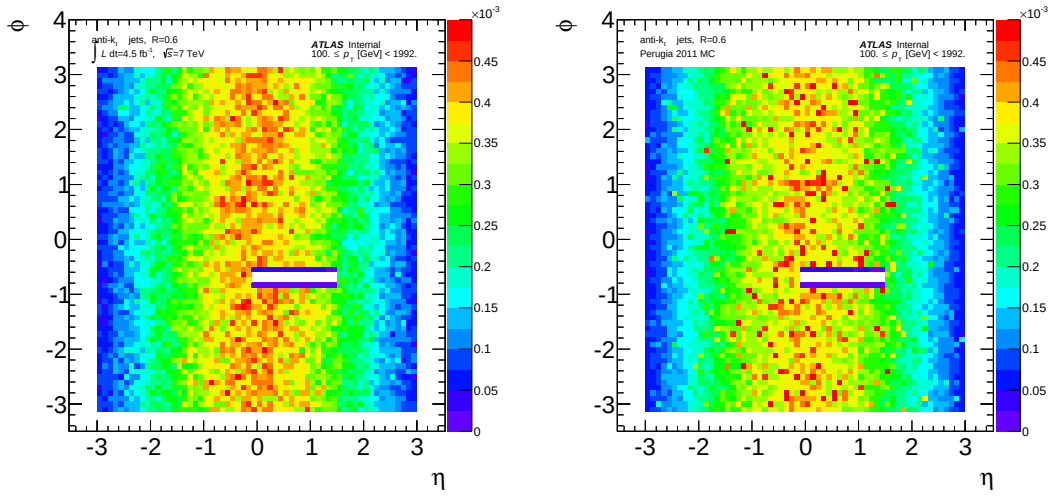

(a) (b)

Figure 4.8: The detector-level two-dimensional distributions of jet $\eta - \phi$ in data (a) and in MC (b). Plots for anti-k_t jets with $R = 0.6$ are shown. The white band in the middle of the plane corresponds to the rejection of jets falling into the problematic LAr area (Sec. 4.2.2).

derived as:

$$P_{ij} = \frac{A_{ij}}{\sum_{k=1}^{N_{\text{bins}}} A_{kj}} \tag{4.2}$$

$$\tilde{P}_{ij} = \frac{A_{ij}}{\sum_{k=1}^{N_{\text{bins}}} A_{ik}} \tag{4.3}$$

$$\tag{4.4}$$

P_{ij} has the meaning of a probability that an event generated in the bin j would be reconstructed in the bin i. $\tilde{P}_{ij}$ has the meaning of a probability that an event reconstructed in the bin i originates (was generated) in the bin j.

As stated above, the IDS method is iterative. It uses the unfolding matrix to derive an intermediate unfolded spectrum that is used to improve the TM. From the improved TM, new unfolding matrix is calculated and the procedure repeats. The improvement is based on a difference between the intermediate unfolded spectrum and the MC truth spectrum. Both the "improvement" and "unfolding" steps are controlled by a regularization function $f(\Delta x, \sigma, \lambda)$ that quantifies the significance of deviations between two given spectra. In each bin, Δx is the difference, σ is the associated uncertainty and λ is a regularization parameter. The continuous, smooth and monotone function $f(\Delta x, \sigma, \lambda)$ is 0 for bins with no (significant) difference of the two spectra, i.e. if $\Delta x \to 0$. It is 1 if the difference is much larger than the associated uncertainty, i.e. $\Delta x >> \sigma$. The parameter λ is used to scale the uncertainty σ and, therefore, it changes the discrimination between a significant deviation and a statistical fluctuation. In each bin, the IDS method distributes any deviation of data from the reconstructed MC spectrum in two steps:

- The fraction $f(\Delta x, \sigma, \lambda)$ of the deviation is distributed into all the bins with the use of the unfolding matrix.

- The remaining fraction $1 - f(\Delta x, \sigma, \lambda)$ is left in the actual bin.

The second item is very important because it prevents large but insignificant deviations from propagation to more precisely measured parts of the spectrum. It is especially important in cases when a background subtraction introduces large uncertainty.

IDS can also be used in cases of new significant structures in data that are not modeled by the MC. It carefully derives a normalization factor of the MC (roughly speaking, the total number of events in data with respect to MC) without including events belonging to the new structures. Therefore, the normalization factor is not affected by the absence of the structures in MC.

IDS can also be generalized to cases when the reconstructed and truth spectra have different binning.

4.3.2 Transfer matrix

In the inclusive jet cross-section analysis, entries of the TM are not events but individual jets. To build the TM, it is therefore necessary to match the truth jets with the reconstructed ones in the MC. The geometrical matching algorithm used takes into account directions of the jets only. A truth and a reconstructed jets are considered as matched if they both belong to the same y-bin, are the closest to each other and are within $\Delta R < 0.3$ distance from each other. Unmatched jets (both reconstructed and truth) are counted separately and their numbers are used in the correction for detector inefficiencies.

In the MC presented in Sec. 4.2, the truth jet collection does not contain jets coming from the overlaid pile-up interactions. Most of those jets are thus unmatched despite the fact that the "pile-up" jets contribute to the data spectrum. However, the effects of this incompatibility is not important because there are hardly ever pile-up jets with $p_{\mathrm{T}} > 100$ GeV.

4.3.3 Three step unfolding procedure

The unfolding procedure used in the inclusive jet cross-section analysis corrects for both the detector inefficiencies and for the migration of jets among p_{T} bins. The migrations among y-bins are small and they are treated by a bin-by-bin correction. Fig. 4.9 shows the purity of y-bins for anti-k_t jets, $R = 0.6$; the purity is defined as the number of truth jets generated and reconstructed in the same bin over the total number of jets reconstructed in that bin. The purity is higher than 95 % in all the y-bins. It is higher for anti-k_t jets with $R = 0.4$.

All the unfolding procedure consists of three steps:

- Bin-by-bin multiplicative correction of the detector-level data spectrum by the efficiency of matching reconstructed jets to truth jets.

- IDS unfolding using the transfer matrix built from matched reconstructed and truth jets as described above. Each y-bin is unfolded separately thus correcting for the migrations among p_{T}-bins only.

- Bin-by-bin division by the efficiency of matching truth jets to the reconstructed ones.

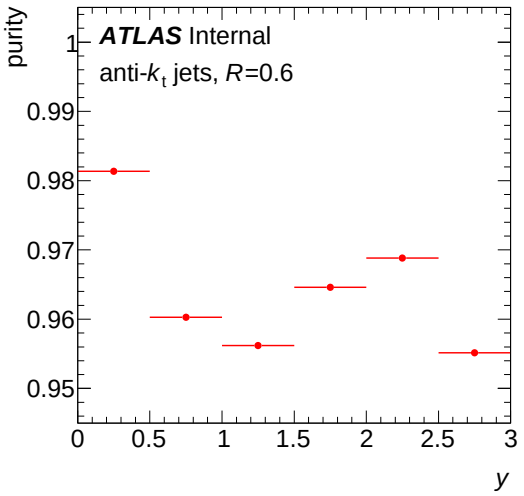

Figure 4.9: Purity of y-bins for anti-k_t jets, $R = 0.6$. Here, the purity is defined as the number of truth jets generated and reconstructed in the same y-bin over the total number of jets reconstructed in that bin.

The two bin-by-bin corrections include the effects of migrations among y-bins.

In order to reduce the effects of the jet migrations from/to the measured p_{T}-range in each y-bin, the input spectra are extended by one p_{T}-bin below 100 GeV. The input jet spectra lower limit used is 84 GeV.

4.3.4 Bias of the unfolding

A measurement is usually biased by the unfolding procedure and its settings together with the modeling of the truth spectrum. The unfolding method and its settings are chosen such that this bias is minimized. In order to estimate the bias, a data-driven closure test is performed as described in Sec. 5.1.5 of [83].

In the test, the transfer matrix is modified by weighting the truth spectrum in such a way that the reconstructed MC spectrum matches the reconstructed data spectrum as close as possible. For the weighting, a smooth function has to be found. The modified reconstructed MC spectrum is unfolded using the original transfer matrix. The result is compared with the modified truth spectrum. Their difference is interpreted as a bias due to the used method. It is taken as a systematic uncertainty.

In the presented analysis, three unfolding methods are tested: IDS, SVD and bin-by-bin correction. The comparison of the corresponding biases is shown in Fig. 4.10 for all the y-bins for anti-k_{t} jets with $R = 0.6$. In IDS, one iteration is performed only, already giving the lowest bias among the three unfolding methods.

4.3.5 Statistical uncertainty

The statistical uncertainty in each (p_{T}, y) bin cannot be estimated as a variance of the Poisson distribution because of two effects:

- Several triggers may contribute to a bin because the bin edges do not overlap

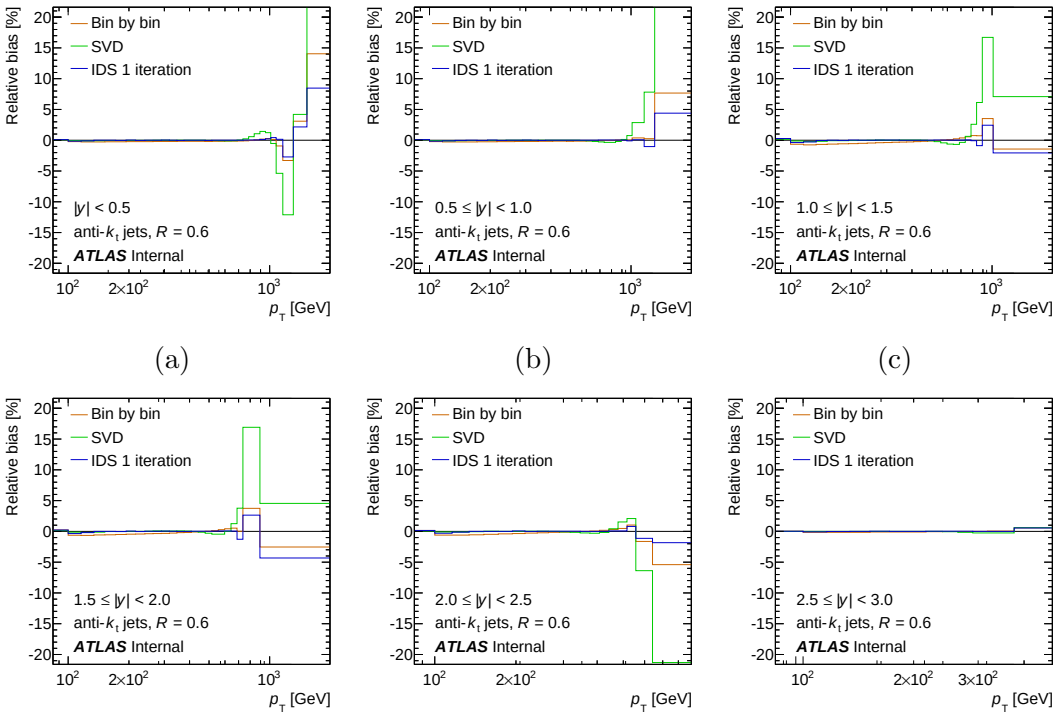

Figure 4.10: Comparison of the bias of three unfolding methods: IDS, SVD and bin-by-bin correction. In IDS, 1 iteration is performed only. All the six y-bins are shown for anti-k_t jets with $R = 0.6$.

with limits of the p_T-ranges covered by different triggers.

- Unfolding causes jets migrate among bins.

The statistical uncertainty is estimated with the bootstrap method ([83]) which is based on pseudo-experiments. Aside the measured inclusive jet spectrum, 10^4 toy spectra are created. They are filled with jets in a similar way as the nominal spectrum but the jets get different weights. In each event, a set of 10^4 weights is generated according to the Poisson distribution with mean equal to 1. If a jet contributes to the nominal spectrum in the event, it is filled to each toy spectrum weighted by the corresponding weight to that toy. Each toy spectrum is unfolded with the nominal TM and a covariance matrix is built from them. The statistical uncertainty in a bin is then estimated as a square root of the corresponding diagonal element of the covariance matrix.

An important advantage of the bootstrap method is that it preserves statistical correlations of jets in events because all the jets in an event get the same weight in a given pseudo-experiment.

Due to the finite statistics of MC, the TM is also affected by a statistical uncertainty. This uncertainty is estimated in an analogic way as in data. The object being fluctuated is TM instead of the measured spectrum. The generated number of toys is also 10^4. The nominal data spectrum is unfolded 10^4-times: once with each TM toy. From all the toy unfolded spectra a covariance matrix is built. In each p_T-bin, the statistical uncertainty due to the amount of MC events is estimated as a square root of the corresponding diagonal element of the

matrix. The MC statistics is chosen such that the statistical uncertainty due to it is (much) lower than that of data. The comparison of the two uncertainties is shown in Fig. 4.11. The total statistical uncertainty is evaluated as their quadrature sum. It is also displayed in Fig. 4.11.

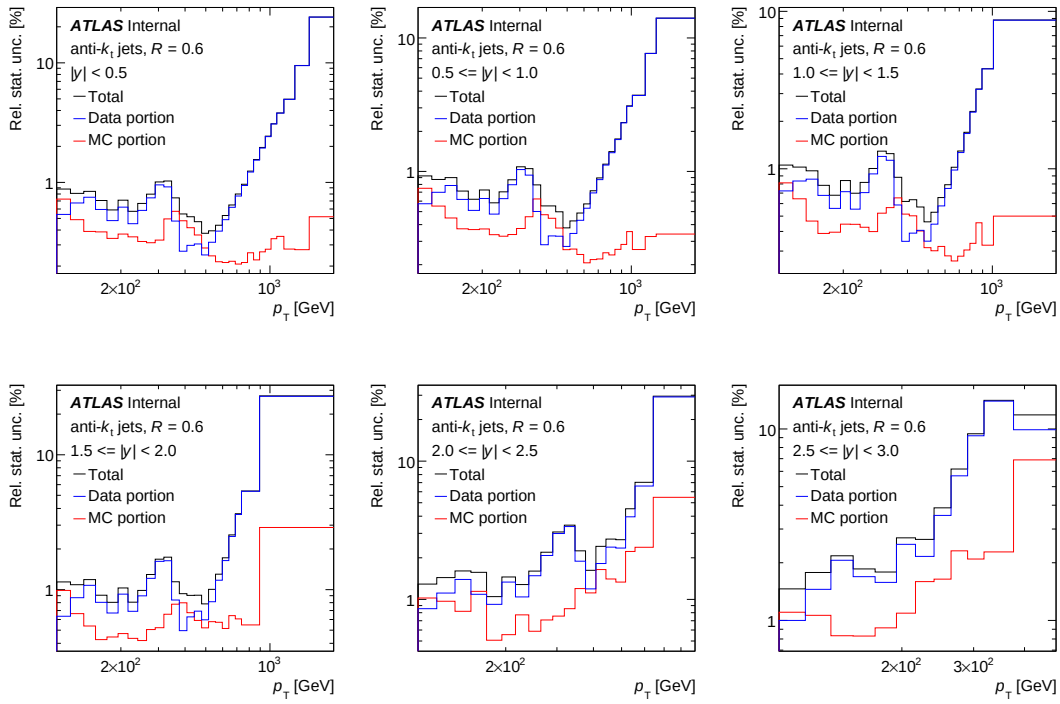

Figure 4.11: Statistical uncertainty due to data (blue), MC (red) and total (black). All the six y-bins are shown for anti-k_t jets with $R = 0.6$.

4.3.6 Interplay between unfolding bias and statistical uncertainty

The IDS unfolding is set to iterate just once and the resulting bias is well below 1 % in most of the (p_T, y) bins. However, it reaches up to ∼10 % in the highest-p_T bins. Adding more iterations would reduce the bias, but it would increase the statistical uncertainty. The dependence of the two entities on the number of iterations is shown in Fig. 4.12. The bias is indeed reduced. However, the increase of the statistical uncertainty is quite important with respect to the benefits of the reduced bias. With one iteration, the bias is larger than 1 % just in regions where the rest of the systematic uncertainty[2] totally dominates. Therefore, one iteration is kept as the most reasonable solution.

4.3.7 Binning

The inclusive jet cross-section binning is required to fulfill the following criteria in each (p_T, y) bin:

[2]The systematic uncertainty will be discussed in the next section.

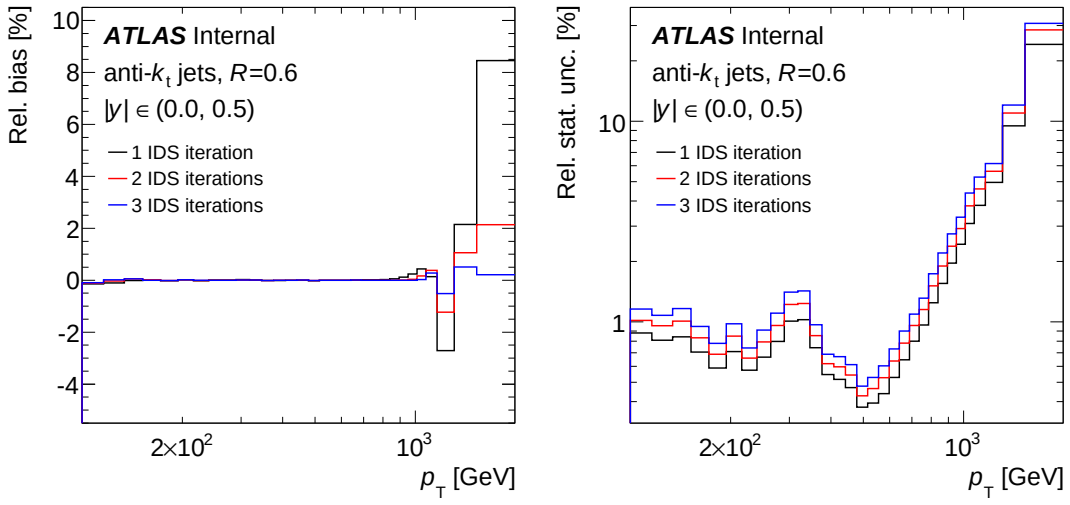

(a) (b)

Figure 4.12: Relative bias (a) due to the IDS unfolding method for the settings with 1, 2 and 3 iterations. Total statistical uncertainty (b) after propagation through the IDS unfolding with 1, 2 and 3 iterations. Just the first y-bin for anti-k_t jets with $R = 0.6$ is shown.

- Statistical uncertainty is lower than 40 % of the systematic uncertainty (see Sec. 4.4).
- Correlation between adjacent p_T-bins is lower then 80 %.
- Jet migration purity in p_T is higher then 50 % in each p_T-bin and higher then 60 % in bins with statistical uncertainty higher then 10 %.

The p_T-binning is different for different y-bins. However, for each y-bin, the p_T-bin edges are required to overlap with the p_T-bin edges in all the other y-bins.

The final binning fulfills the above requirements almost perfectly. The jet migration purity is shown in Fig. 4.13 for two representative y-bins for anti-k_t jets with $R = 0.6$. The correlation matrix is in Fig. 4.14 for the same two y-bins.

4.4 Systematic uncertainties

The inclusive jet cross-section measurement is affected by several sources of systematic uncertainty. The dominant one is the JES uncertainty that is briefly discussed in Sec. 2.4.4. Further sources are uncertainty in the JER and jet angular resolution (JAR) determination, uncertainty related to the jet quality selection (jet cleaning algorithm) and luminosity uncertainty. A source of a very small uncertainty is also the choice of the "matching radius" ($\Delta R < 0.3$) in the truth-to-reconstructed jet matching procedure described in Sec. 4.3.2.

All these sources are propagated through all the analysis chain, including the unfolding. Most uncertainties are affected by statistical fluctuations after the propagation. This is especially true for the small sources. A dedicated procedure

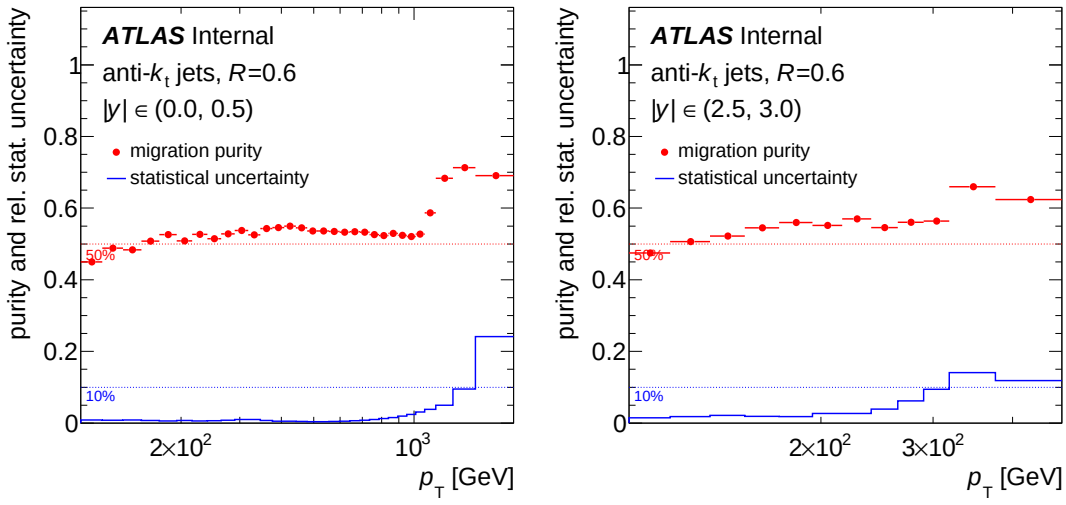

(a) (b)

Figure 4.13: The jet migration purity in p_{T} for the lowest $|y| < 0.5$ (a) and the highest $2.5 \leq |y| < 3.0$ (b) y-bin. The relative statistical uncertainty is also displayed. Shown for anti-k_{t} jets with $R = 0.6$.

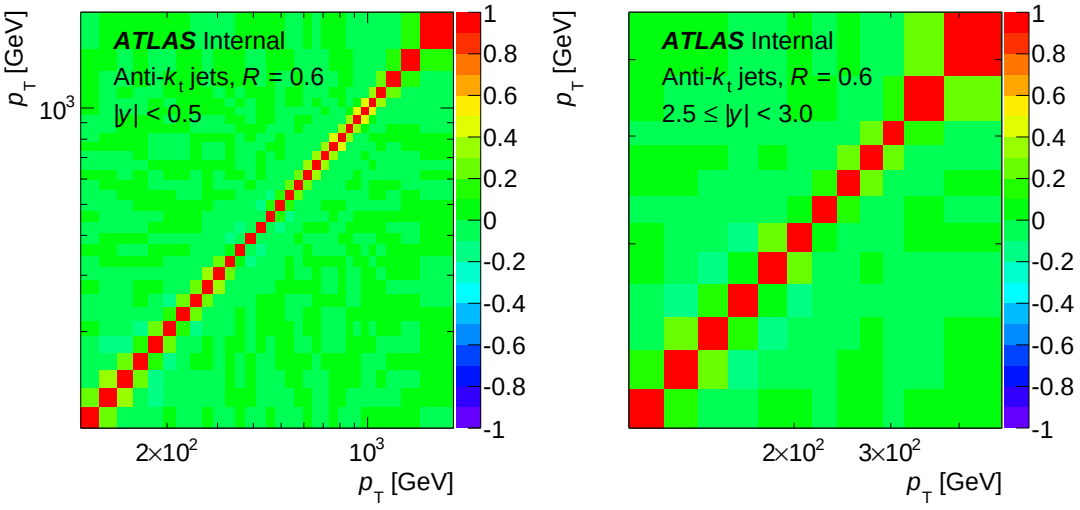

(a) (b)

Figure 4.14: The correlation matrix for the lowest $|y| < 0.5$ (a) and the highest $2.5 \leq |y| < 3.0$ (b) y-bin. Shown for anti-k_{t} jets with $R = 0.6$.

that includes Gaussian kernel smoothing [84] is used to get rid of the statistical fluctuations.

Many sources of the uncertainty are constructed as Gaussian-shaped at the jet-level but they are non-Gaussian after the propagation to the cross-section. The shape of the cross-section uncertainty components is also studied.

4.4.1 JES uncertainty

The JES uncertainty is the dominant source of the systematic uncertainty. It is split into 63 independent components with a Gaussian shape at the jet-level.

Each component is treated as fully correlated across all the (p_{T}, y) bins. The propagation of these jet-level uncertainties to the cross-section is done in the MC to reduce statistical fluctuations in the systematic uncertainty determination because the statistical uncertainty is much lower in MC than in data, see Fig. 4.11. The nominal inclusive jet spectrum is measured in MC by applying the same cuts as in data. It is also unfolded in the same way as data. This cross-section is taken as a baseline in the systematic uncertainty determination. It is assumed to be the median of the cross-section distribution in each (p_{T}, y) bin. It will be called the "nominal cross-section" in this section. In the next step, the inclusive jet spectrum is remeasured (twice) for each component of the JES uncertainty; in each such measurement, all jet transverse momenta are shifted up (resp. down) by one standard deviation, $\sigma_{\mathrm{NP}}^{\mathrm{jet}}$, of the corresponding component.[3] Each such spectrum is unfolded in the same way as data. The resulting spectra are interpreted as positions of the $\pm 1\sigma$ quantiles of the cross-section distribution in each (p_{T}, y) bin for a given component.

Smoothing of the JES uncertainties

The JES uncertainties are derived from MC to reduce the impact of statistical fluctuations. However, residual fluctuations might persist and affect the systematic uncertainty determination. The most affected uncertainty components correspond to small nuisance parameters. Reduction of the impact of these statistical fluctuations is the topic of this section.

As a first step, a statistical uncertainty is assigned to the estimation of each JES-related uncertainty component. To do this, the bootstrap method is used. Pseudoexperiments are generated as described in Sec. 4.3.5. For each component and for both $\pm 1\sigma$ uncertainties, 500 pseudoexperiments are produced. In each (p_{T}, y) bin, the statistical uncertainty is estimated separately. In each pseudoexperiment, the distance of a given quantile position from the nominal cross-section (determined in the same pseudoexperiment) is evaluated. The statistical uncertainty is estimated as a RMS of the distribution of these distances.

In the second step, statistical significance of each systematic uncertainty estimate in each (p_{T}, y) bin is checked. In the case of a low significance, neighbouring bins are merged. This is done for each uncertainty component. The rebinning procedure uses both the systematic uncertainty and the statistical uncertainty of its determination relative to the nominal cross-section value in each (p_{T}, y) bin. An example input is displayed in Fig. 4.15 by the black line for one chosen component of the JES uncertainty. The relative systematic uncertainty is considered as significant in bins where it is displaced from zero by more than two standard deviations of the corresponding statistical uncertainty. If it is not the case in at least one p_{T}-bin for a given uncertainty component in a given y-bin, it is rebinned until the statistical significance is reached in all the p_{T}-bins. The rebinning proceeds independently in two directions: from the lowest p_{T}-bin to the highest one and vice versa. If an insignificance is found in a bin, it is merged

[3] Here, the abbreviation NP stands for "nuisance parameter"; the different uncertainty components are often called nuisance parameters.

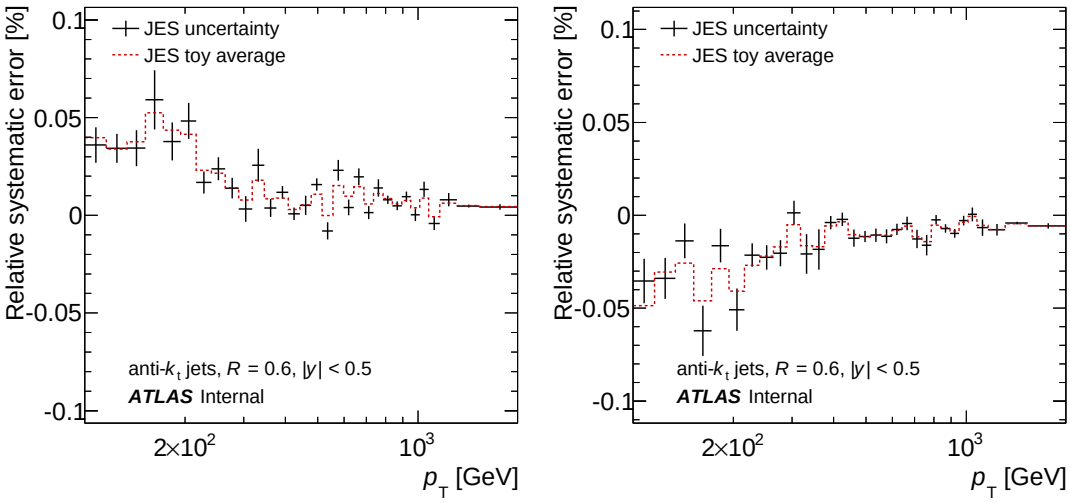

Figure 4.15: Relative systematic uncertainty due to one component of the JES before smoothing. The $+1\sigma$, resp. -1σ uncertainty is shown in (a), resp. (b). The black line corresponds to the uncertainty derived by shifting all jet transverse momenta by plus, resp. minus one standard deviation of the corresponding jet-level uncertainty. The vertical error bars display the statistical uncertainty of the estimation. Its evaluation is described in Sec. 4.4.1. The red dashed line corresponds to the uncertainty averaged over 500 pseudoexperiments. The uncertainty component shown is related to the jet selection by a JVF cut in the Z+jet direct p_{T} balance method.

with the next bin taking into account their statistical errors:

$$\frac{1}{\sigma_{\mathrm{stat}}} = \sqrt{\frac{1}{\sigma^2_{\mathrm{stat},\,1}} + \frac{1}{\sigma^2_{\mathrm{stat},\,2}}} \tag{4.5}$$

$$\sigma_{\mathrm{syst}} = \sigma^2_{\mathrm{stat}} \left(\frac{\sigma_{\mathrm{syst},\,1}}{\sigma^2_{\mathrm{stat},\,1}} + \frac{\sigma_{\mathrm{syst},\,2}}{\sigma^2_{\mathrm{stat},\,2}} \right) \tag{4.6}$$

where σ_{syst} ($\sigma_{\mathrm{syst},\,1,\,2}$) stands for the systematic uncertainty in the merged bin (original bins) and σ_{stat}, $\sigma_{\mathrm{stat},\,1,\,2}$ are the corresponding statistical uncertainties. From the two independent derivations ("bottom-to-top" and "top-to-bottom"), the one that yields more bins after the rebinning is kept.

In the third step, all the (rebinned) uncertainties are smoothed with a Gaussian kernel smoothing procedure. The procedure is done separately for each shift (up or down) of eachJES uncertainty component and for each y-bin. Each p_{T}-bin is assigned new content calculated as a weighted average of all the p_{T}-bins contents. The weight for i-th p_{T}-bin is given by a Gaussian function

$$\exp\left(-\left(\frac{x_i - x_{\mathrm{act}}}{5 + 0.15 x_{\mathrm{act}}} \right)^2 \right) \tag{4.7}$$

with x_{act} (x_i) being the centre of the actual (of the i-th) p_{T}-bin. In the smoothing procedure, the original p_{T}-binning is restored. The uncertainty being smoothed

is in the original binning but the bin contents are set to be equal to the rebinned uncertainty.

Example results of the three steps are shown in Fig. 4.16.

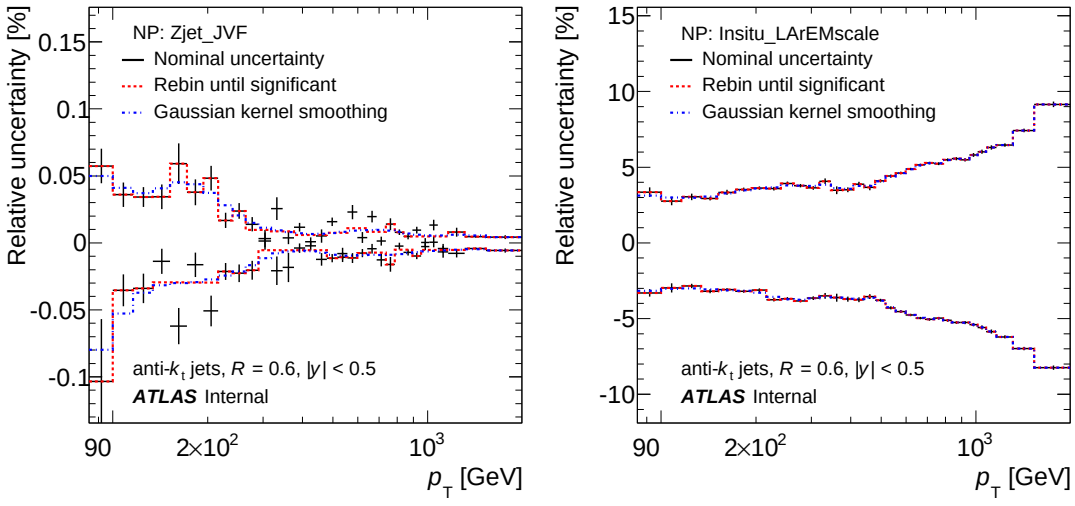

(a) (b)

Figure 4.16: Relative systematic uncertainty due to a small (a) and a large (b) component of the JES. The black line corresponds to the uncertainty derived by shifting all jet transverse momenta by plus (resp. minus) one standard deviation of the corresponding jet-level uncertainty. The vertical error bars display the statistical uncertainty of the estimation. Its evaluation is described in Sec. 4.4.1. The red dashed line corresponds to the rebinned uncertainty. The blue dashed line is the smoothed uncertainty in the original p_{T}-binning. The uncertainty component shown is related to the jet selection by a JVF cut in the Z+jet direct p_{T} balance method (a) and to the energy measurement in the LAr calorimeter (b). Both are related to the anti-k_{t} jets with $R = 0.6$ and to the lowest y-bin, $|y| < 0.5$.

For three large uncertainty components ($\gtrsim 10\,\%$) the Gaussian kernel (4.7) yields too much bias. Another kernel function is therefore used:

$$\exp\left(-\left(\frac{x_i - x_{\mathrm{act}}}{5\log x_{\mathrm{act}}}\right)^2\right) \tag{4.8}$$

This function yields less smoothing because it assigns higher weight to the actual bin with respect to the other p_{T}-bins. The three components are due to the energy measurement uncertainty in the LAr calorimeter, due to the energy over momentum measurement of single particles (this component is used in the highest-p_{T} bins) and due to parton shower modelling in high-y regions (this uncertainty plays a key role in the dijet p_{T}-balance technique).

Shape of the uncertainties at the cross-section level

The JES uncertainty components are constructed to have gaussian shape at the jet-level. It means that the jet energy is distributed according to the gaussian distribution with $\sigma = \sigma_{\mathrm{NP}}^{\mathrm{jet}}$. However, the uncertainty components are non-gaussian

after the propagation through the steeply falling inclusive jet spectra. They are asymmetric as can be seen e.g. from comparison of the $+1\sigma$ and -1σ uncertainties. Their shape at the cross-section level must be studied so that the uncertainty was treated properly in the future usage of the measured results.

The previous Sec. 4.4.1 describes how the quantiles related to $\pm1\sigma$ are determined. The higher quantiles related to $\pm2\sigma$, $\pm3\sigma$, $\pm4\sigma$, $\pm5\sigma$ are evaluated in an analogic way - by shifting all jet transverse momenta by $\pm N \times \sigma_{\mathrm{NP}}^{\mathrm{jet}}$ with $N = 2, 3, 4, 5$ and following the smoothing procedure described previously. An example is shown in Fig. 4.17 for one selected p_{T}-bin and for the JES uncertainty component due to the energy measurement in the liquid argon calorimeter. The quantile positions determined experimentally are compared with the expectations evaluated for two different probability density distributions: Gaussian and log-normal. These expectations are based on the experimentally determined median and 1σ quantile. Fig. 4.18a and 4.18b show the relative difference between the expected and the measured quantile positions as a function of the jet p_{T} for the same component as Fig. 4.17. In general, this relative difference is lower for the log-normal assumption.

Log-normal distribution provides generally better description of the real distribution shape for the JES uncertainty components that are large ($\gtrsim$10 % at the cross-section level) as the one in Fig. 4.18a, 4.18b. On the other hand, the sub-percent uncertainty components are equally described by both the log-normal and Gaussian distributions. It is demonstrated in Fig. 4.18c, 4.18d that are analogic to the Fig. 4.18a and 4.18b but for a small JES component.

Assumptions on correlations of the JES uncertainty components

The nominal set of JES uncertainty components is based on good knowledge of the correlations among different uncertainty sources. However, this knowledge is limited. To estimate the uncertainty on correlations in jet-based analyses two additional sets of the JES uncertainties are built. The sets are derived with "stronger" and "weaker" assumptions on the correlations.

Both sets are propagated through the inclusive jet cross-section measurement. The total JES-related uncertainty of the cross-section is very similar for all the three available sets (nominal, "stronger" and "weaker"). Its comparison is shown in Fig. 4.19 for the $|y| < 0.5$ and $2.5 \leq |y| < 3.0$ bins for $R = 0.6$ jets. The set with "stronger" assumptions yields an overall uncertainty that is slightly bigger than the other two sets. It can be easily understood: roughly speaking, correlated uncertainty components are added linearly whereas uncorrelated ones are added in quadrature. Thus the more sources are correlated, the larger the total uncertainty can be expected.

4.4.2 JER uncertainty

The unfolding procedure described in Sec. 4.3 corrects the detector-level data for the effects of the finite JER. The JER is determined in-situ with the use of the dijet p_{T} balance method and the bisector method [85, 47]. JER is well described in the MC: it agrees with data within uncertainty. Therefore, the finite precision of the JER determination is the only thing that results in a systematic uncertainty of the inclusive jet cross-section measurement.

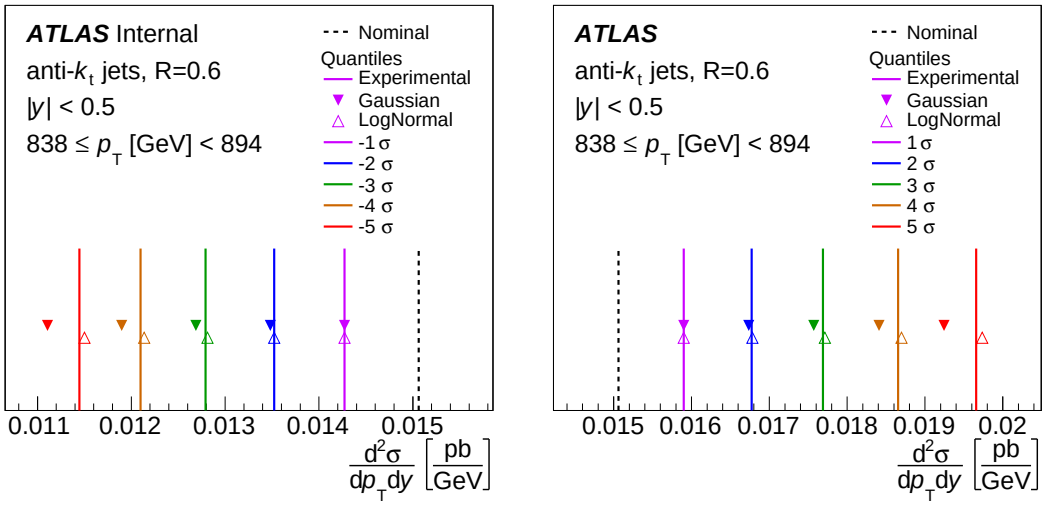

(a) (b)

Figure 4.17: Measured value of the inclusive jet cross-section in one (p_{T}, y)-bin (black dashed line) and positions of five quantiles of the (asymmetric) cross-section probability distribution function due to one component of the JES uncertainty determined experimentally (solid lines). Positions of five quantiles evaluated for a given expected distribution, Gaussian (full triangles) and log-normal (open triangles) are also shown. The measured value of the cross-section is the median of the probability distribution function. The higher (lower) experimental quantiles are determined by shifting all jet energies by $+(-)1\sigma^{\mathrm{jet}}_{\mathrm{NP}}$, $+(-)2\sigma^{\mathrm{jet}}_{\mathrm{NP}}$, $+(-)3\sigma^{\mathrm{jet}}_{\mathrm{NP}}$, $+(-)4\sigma^{\mathrm{jet}}_{\mathrm{NP}}$, $+(-)5\sigma^{\mathrm{jet}}_{\mathrm{NP}}$ of the studied uncertainty component, rederiving the cross-section. By definition, they are the upper (bottom) limits of the $+(-)N\sigma$ uncertainty bands. Only quantiles higher, resp. lower than the median are shown in (b), resp. (a). Expectations of the quantile positions are based on the experimentally determined median and $+1\sigma$, resp. -1σ quantile in (b), resp. (a). Quantiles predicted with the log-normal assumption are closer to the quantiles determined experimentally. The JES uncertainty component shown here is due to the energy measurement in the liquid argon calorimeter. The plots correspond to jets built with the anti-k_t algorithm with $R = 0.6$.

To do this, a new transfer matrix is built with the JER increased by one standard deviation. When a jet is filled to the TM, its reconstructed p_{T} is smeared by a factor derived from a Gaussian distribution with $\mu = 1$ and a certain σ_{smear}. The σ_{smear} is set to such a value that the overall JER is described by a Gaussian with $\sigma = \sigma_{\mathrm{MC}} + \sigma_{\mathrm{JER\ unc.}}$ where σ_{MC} is the JER in MC and $\sigma_{\mathrm{JER\ unc.}}$ is the JER uncertainty derived from data. Apparently, σ_{smear} must satisfy the following relation:

$$\sigma^2_{\mathrm{smear}} + \sigma^2_{\mathrm{MC}} = (\sigma_{\mathrm{MC}} + \sigma_{\mathrm{JER\ unc.}})^2 \tag{4.9}$$

For each jet, the TM is filled 100 times with different generated smearing factors. It is done to decrease the statistical fluctuations. In the next step, the detector-level MC jet spectrum is unfolded with this TM and the relative difference of the result with respect to the nominal measurement[4] is taken as a $+1\sigma$ systematic

[4]Derived by unfolding the detector-level MC jet spectrum with the nominal TM.

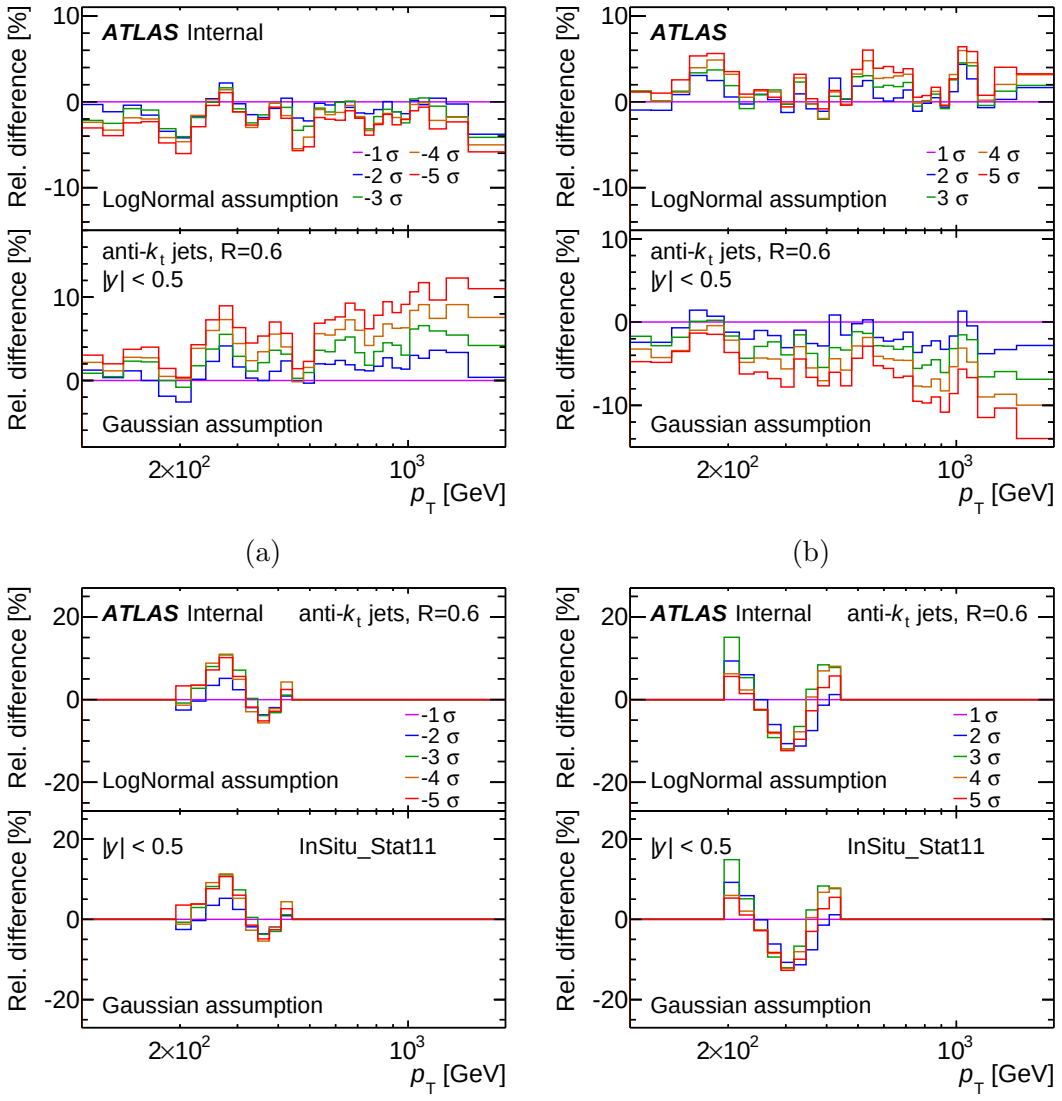

Figure 4.18: Relative difference of experimental and expected quantiles as a function of the jet p_{T}, in a study of the shape of the measured cross-section probability distribution function due to one important component of the JES uncertainty. In each p_{T}-bin, quantiles determined experimentally are compared with the expected positions evaluated for a Gaussian and log-normal shape assumption of the probability distribution function. In each p_{T}-bin and for each of the two shape assumptions, the relative difference between the expected and experimental quantiles is plotted. Only quantiles higher, resp. lower than the median are shown in (b) and (d), resp. (a) and (c). The results are shown for jets identified with the anti-k_{t} algorithm with $R = 0.6$ in the lowest y-bin. In (a) and (b), the JES uncertainty component chosen is due to the energy measurement in the liquid argon calorimeter. For the case of such a large uncertainty, the relative difference is lower for the log-normal assumption. In (c) and (d), the JES uncertainty component is due to a statistical uncertainty of the in-situ Z+jet p_{T} balance method. For the case of such a small uncertainty, the relative difference is very similar for the two assumptions.

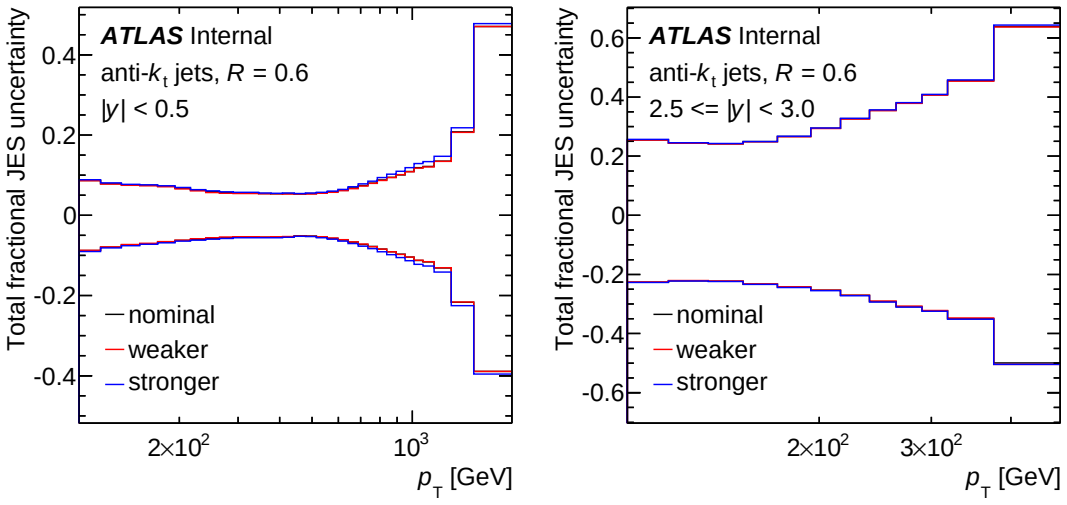

(a) (b)

Figure 4.19: The total inclusive jet cross-section uncertainty due to the JES. It is evaluated for three different assumptions on correlations of the JES uncertainty sources. It is shown for jets identified with the anti-k_t algorithm with $R = 0.6$ in the lowest (a) and the highest (b) y-bin.

uncertainty.

To further reduce the statistical fluctuations in the determination of the systematic uncertainty due to JER, it is smoothed by the procedure described in Sec. 4.4.1. To estimate the statistical bias, 500 pseudoexperiments/toys of the TM are generated by assigning different Poisson weights to each event. Detector-level MC jet spectrum is unfolded with each such TM toy, giving 500 toy-estimates of the $+1\sigma$ systematic uncertainty due to JER.

The uncertainty of the inclusive jet cross-section due to the precision of the JER determination is assumed to be symmetric. It means that the -1σ uncertainty is considered to be equal to the $+1\sigma$ one, except for the sign. The result is shown in Fig. 4.20a for the $2.5 <= |y| < 3.0$ bin for anti-k_t jets with $R = 0.6$.

4.4.3 JAR uncertainty

The resolution in the jet polar angle θ influences the jet p_T in two ways:

- Through the direct calculation of p_T from energy as $p_T = E/\cosh\eta$.
- Through the application of the JES calibration factors that depend on the jet η.

These two effects propagate to the inclusive jet cross-section. Furthemore, the finite resolution of the jet polar angle influences the jet rapidity reconstruction and causes migrations among different y-bins.

The resolution of the jet polar angle is determined from MC. The polar angles of the matched truth and reconstructed jets are compared in predefined bins of jet p_T, y and NPV [86]. No bias in the polar angle reconstruction is found in any bin. The resolution in the polar angle is 0.035 rad at most in the high pile-up

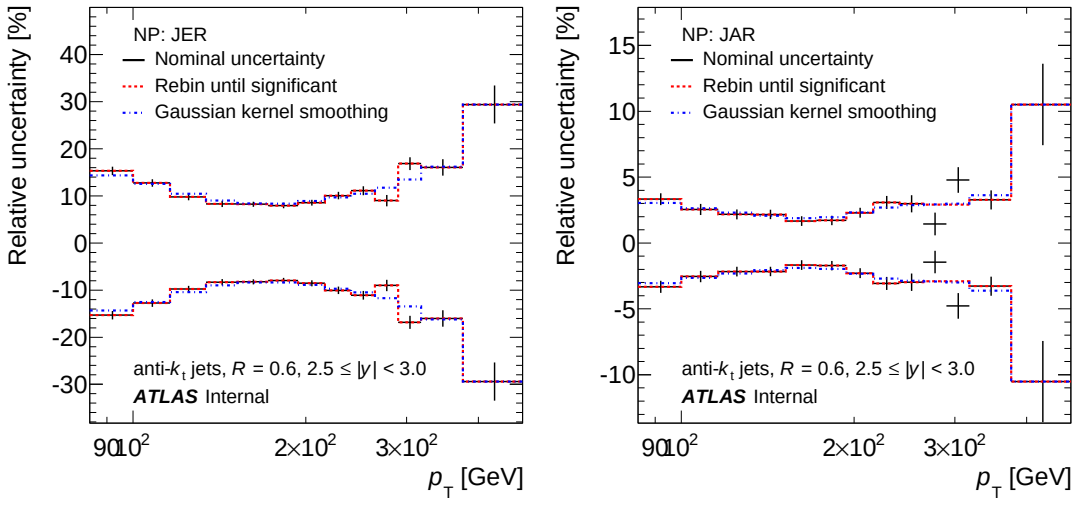

(a) JER (b) JAR

Figure 4.20: The uncertainty related to the JER (a) and JAR (b) in the 2.5 <= $|y|$ < 3.0 bin for anti-k_t jets with $R = 0.6$. It is propagated through the measurement.

bin ($10 \leq$ NPV ≤ 12) for jets with energy $E \geq 100$ GeV. An uncertainty of 10 % is assigned to the polar angle resolution determination. This choice is based on the study performed in [87] where the resolution of the azimuthal angle is compared for isolated tracks and isolated topoclusters. In the study, maximum disagreement of ∼10 % in the resolution is found between data and MC.

The impact of the data-MC JAR disagreement on the cross-section is considered as a systematic uncertainty. The uncertainty is estimated in an analogic way to the JER case: by smearing jet polar angles in such a way that the resulting JAR increases by 10 %. The construction of the TM, number of pseudoexperiments and the smoothing procedure is the same as for the JER uncertainty. The result is shown in Fig. 4.20b for the 2.5 <= $|y|$ < 3.0 bin for anti-k_t jets with $R = 0.6$.

4.4.4 Jet reconstruction efficiency

The jet reconstruction efficiency is estimated for both data and MC by using track jets as a reference. The method is described in [44] and will be briefly reviewed here.

To estimate the jet reconstruction efficiency in data, a sample of track-dijet events is used. The leading track jet is required to have $p_T > 15$ GeV; it is used as a tag jet. A second track jet is required to be in the opposite direction in the azimuthal angle. A criterium of $|\Delta\phi| > 2.8$ is imposed. The jet is further required to have $p_T > 5$ GeV. This second jet is used as a probe jet. If there are two track jets satisfying the conditions imposed on the probe jet, the event is rejected. The tag jet must be matched to a calorimeter jet with $p_T > 7$ GeV; the matching criterium is $\Delta R < 0.6$. Similar criteria are also used for the matching of the probe jet to another calorimeter jet: $p_T^{calo} > 7$ GeV and $\Delta R < 0.4(0.6)$ for anti-k_t jets with $R = 0.4(0.6)$. The jet reconstruction efficiency is defined as

the number of matched probe jets with respect to all the probe jets used. It is binned in probe jet p_{T}, η and in μ_{avg}. The result is shown in Fig. 4.21 for anti-k_{t} jets with $R = 0.6$ and a low and a high μ_{avg} bin. The reconstruction efficiency is 100 % in both data and MC for jets with $p_{\mathrm{T}} \gtrsim 30$ GeV regardless of μ_{avg}. This result is confirmed with the use of an alternative MC technique determining the efficiency to reconstruct a calorimeter jet in the vicinity of a truth jet, see [88]. No systematic uncertainty is therefore assigned to the cross-section measurement.

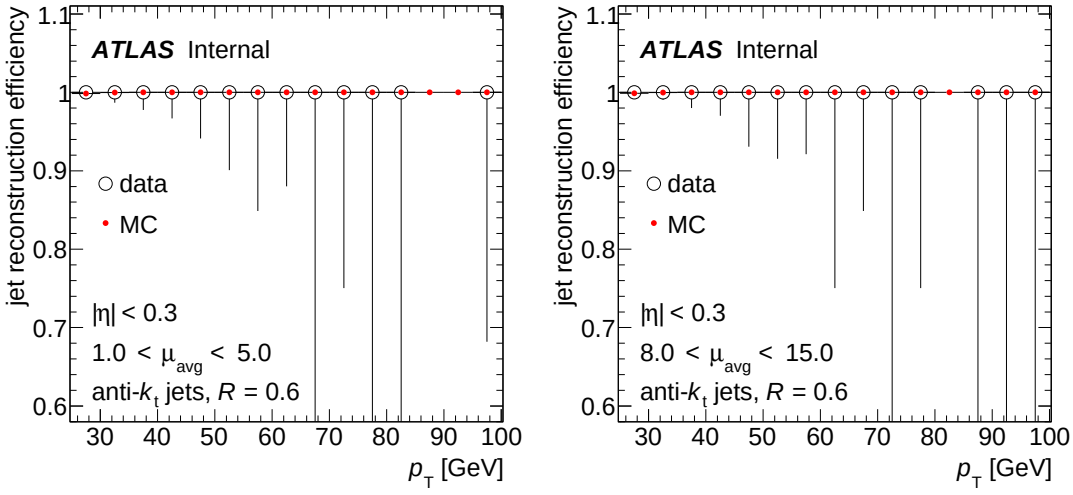

(a) (b)

Figure 4.21: Jet reconstruction efficiency as a function of p_{T} for anti-k_{t} jets with $R = 0.6$. It is determined on data samples with low (a) and high (b) pile-up conditions.

4.4.5 Uncertainty due to the jet cleaning

As discussed in Sec. 4.2.2, the Medium jet cleaning criterium is used to select jets. According to [50], the efficiency of this criterium in MC agrees with data within an envelope of 0.25 %. The MC used in the study was based on Pythia 6 with the AUET2B tune. If this MC was used for unfolding in the inclusive jet cross-section measurement, an uncertainty of 0.25 % on the cross-section would be taken. However, the MC used for the unfolding is based on Pythia 6 with the Perugia 2011 tune.

In order to see the impact of the different MC on the jet cleaning, the distributions of all the variables relevant for the jet selection are checked. Fig. 4.22 shows two representants of the distributions of jet cleaning variables. Fig. 4.22a represents a variable whose distribution in data is not described by neither MC; the variable is the fraction of jet energy coming from cells with too high LAr quality factor. The quality factor is a measure of the difference between the predicted and the measured pulse shape; the higher is the difference the higher is the quality factor. The discrepancy between the two MCs is much lower than between MC and data. Therefore, it is irrelevant from the point of view of this study. Fig. 4.22b shows a variable whose distribution in data is described by

the Perugia 2011 MC better than by the AUET2B MC; the variable displays the fraction of the jet momentum caried by charged particles.

In general, the distributions in the Perugia 2011 MC agree with data similarly (or even better) than those obtained with the AUET2B MC. Therefore, the 0.25 % derived with the AUET2B MC is taken as a conservative uncertainty.

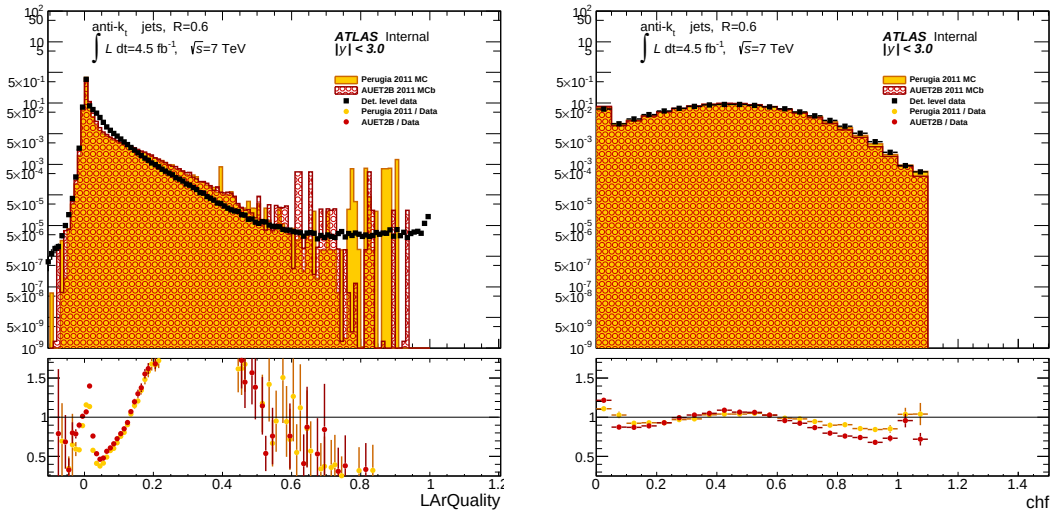

(a) (b)

Figure 4.22: Distributions of two representative variables used in the jet cleaning algorithm. Fraction of the jet energy coming from cells with too high LAr quality factor (a) and fraction of the jet momentum carried by charged particles (b).

4.4.6 Reconstructed-truth jet matching uncertainty

The TM for unfolding is built from reconstructed jets that are matched to truth jets. The matching algorithm requires the matched jets to be within distance of $\Delta R < 0.3$ from each other. Since this choice of ΔR criterium is arbitrary to some extent, it should be assigned an uncertainty. This uncertainty due to the jet matching algorithm is estimated by varying the ΔR cut by ± 0.1.

Two new TMs are built in a similar way as the nominal one. One is constructed with the use of the tighter matching requirement of $\Delta R < 0.2$ and the other with the looser cut of $\Delta R < 0.4$. The nominal spectrum is unfolded with both matrices resulting in two unfolded spectra. To estimate the statistical uncertainty, 500 pseudoexperiments of both spectra are generated. The deviations of the resulting unfolded spectra from the nominal one are used to asses the uncertainty. The relative deviations are assigned the statistical uncertainty in the same way as for JER (Sec. 4.4.2) and JAR (Sec. 4.4.3). Results are shown in Fig. 4.23. Since both ΔR cut variations yield a deviation that is below one permille the uncertainty is neglected.

4.4.7 Uncertainty due to the MC choice

As discussed in Sec. 4.2.3, the MC used for unfolding is different from the MC used to derive the jet calibration. The jet response and JER in the two MCs are

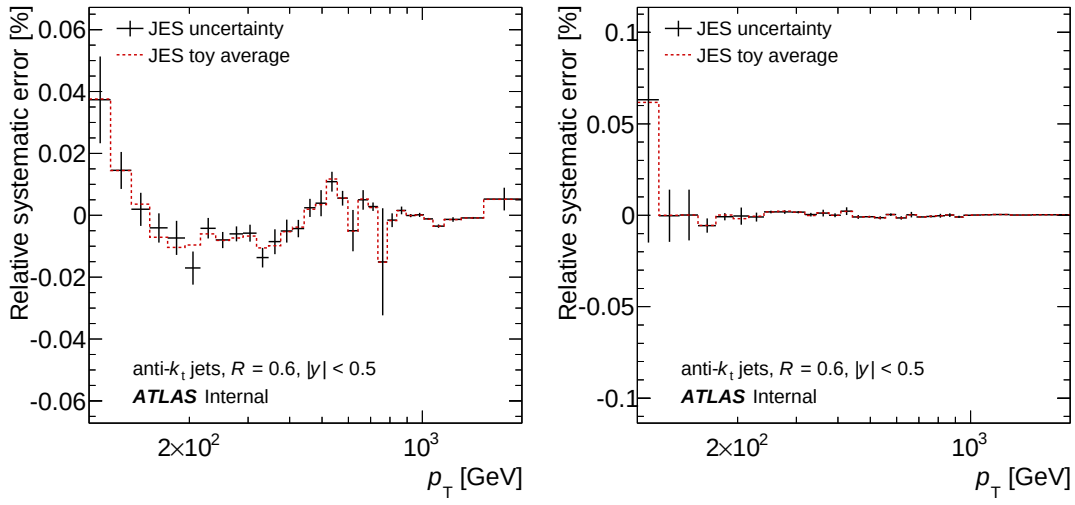

(a) (b)

Figure 4.23: The relative deviation of two inclusive jet spectra built with redefined jet matching algorithm: with the tighter matching requirement of $\Delta R < 0.2$ (a) and the looser one of $\Delta R < 0.4$ (b). Shown for anti-k_t jets with $R = 0.6$ and the lowest y-bin $|y| < 0.5$.

compared.

The discrepancy between the jet responses in the two MCs is taken as an additional source of the systematic uncertainty. The ratio of the two responses minus one is considered as a 1σ relative uncertainty at the jet-level. The uncertainty is assumed to have a Gaussian shape. It is further treated in the same way as all the JES uncertainty sources (propagation through the measurement, smoothing). Fig. 4.24 shows the propagated uncertainty for two representative y-bins. The intermediate steps of the smoothing procedure are also included in the figure.

The JER is compatible in the two MCs. It is assigned no additional uncertainty.

4.4.8 Uncertainty due to unfolding

The uncertainty assigned to the unfolding method covers two effects:

- The choice of the unfolding method and its settings.
- Modelling of the truth spectrum in MC.

Derivation of this uncertainty is described in Sec. 4.3.4. It is shown in Fig. 4.10 for anti-k_t jets with $R = 0.6$.

4.4.9 Luminosity uncertainty

The luminosity measurement has an uncertainty of 1.8 %. The measurement is described in [13] together with the uncertainty assessment.

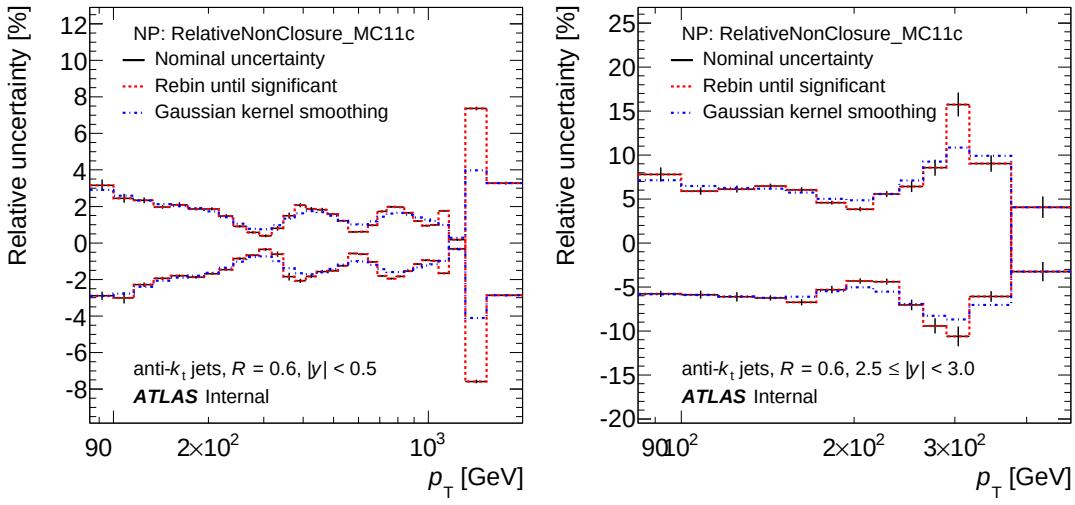

(a) $|y| < 0.5$ (b) $2.5 <= |y| < 3.0$

Figure 4.24: The uncertainty related to the different jet response between two MCs used in the analysis. It is propagated through the measurement. $|y| < 0.5$ bin (a) and $2.5 <= |y| < 3.0$ bin (b) for anti-k_t jets with $R = 0.6$ are shown.

4.4.10 Total systematic uncertainty of the measurement

The above sections describe in detail all the relevant sources of systematic uncertainty for the inclusive jet cross-section measurement. All the different components are summed in quadrature to obtain the total uncertainty. This is done separately for the $+1\sigma$ and -1σ uncertainties. Some JES uncertainty components are built in such a way that the $+1\sigma^{\text{jet}}_{\text{NP}}$ uncertainty of a jet p_{T} is negative; it results in a decrease of the inclusive jet spectrum. In such cases, the upward shifts of the spectrum are added to the $+1\sigma$ overall uncertainty regardless of the sign of $+1\sigma^{\text{jet}}_{\text{NP}}$. Similarly for the downward shifts and the -1σ overall uncertainty. The components showing this behaviour are e.g. the two pile-up-related uncertainties.

Fig. 4.25 shows the total inclusive jet cross-section uncertainty together with the uncertainty related to JER and the total uncertainty due to JES.

4.5 Consistency checks of the measurement

The inclusive jet cross-section is checked against several issues that happened during data taking. They include the non-operational TileCal modules, in-time and out-of-time pile-up, pile-up reweighting of MC, data quality selection (good run list), the time-dependence of the measurement and few fake jets with high-p_{T}. The following subsections describe effects of the non-operational TileCal modules, in-time pile-up and pile-up reweighting of MC. Special care is given to high-p_{T} jets: they are checked one-by-one to make sure that they are measured correctly and that the impact of potential misidentified objects on the measurement is negligible. For the other issues, the analysis team showed no impact in the cross-section measurement, see [88].

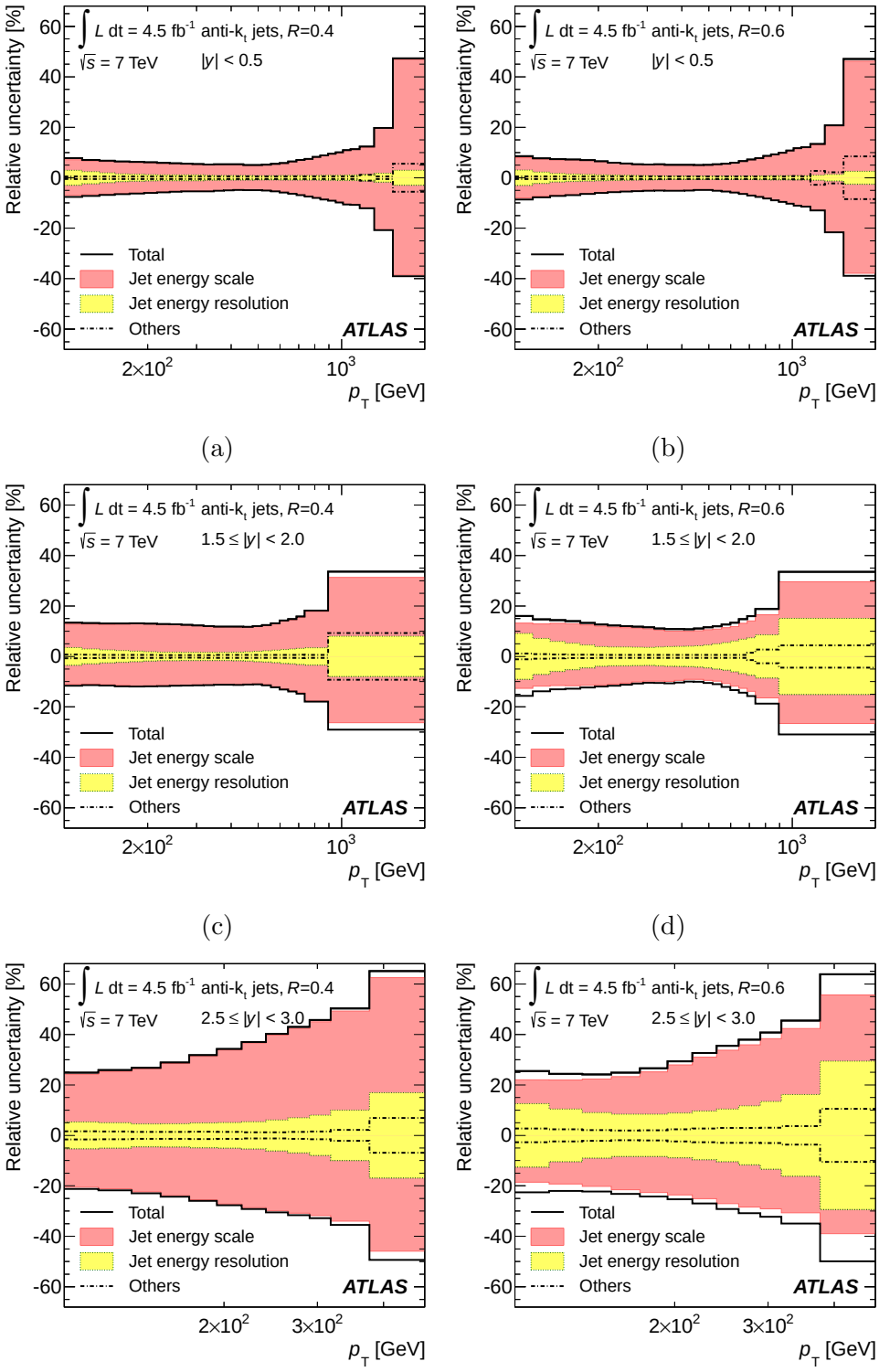

Figure 4.25: The total systematic uncertainty of the inclusive jet cross-section measurement in three selected y-bins for anti-k_t jets with $R = 0.4$ (a), (c), (e) and with $R = 0.6$ (b), (d), (f). The uncertainty due to JES (pink band) and due to JER (yellow band) are also shown.

4.5.1 Non-operational TileCal modules

Chap. 3 describes the impact of the non-operational TileCal modules on the dijet response. It also describes the two available bad channel corrections. One interpolates the energy density measured by neighbouring calorimeter cells. The other is based on the knowledge of jet shapes. Chap. 3 concludes that the latter correction restores the p_{T} response better. However, the impact of the correction on the inclusive jet cross-section must be studied.

The detector-level inclusive jet spectra are remeasured with a cut rejecting jets with ϕ-coordinate falling into a ϕ-region where there is a non-operational TileCal module. Each event is assigned a geometrical weight that compensates the reduction of the phase space. Due to the cut that depends on ϕ only, the weight w is given by a simple formula:

$$w = \frac{2\pi}{2\pi - N\Delta\phi} \tag{4.10}$$

where N is the number of non-operational modules in an event and $\Delta\phi$ is a module width in the ϕ-coordinate. The result is compared to the nominal detector-level spectra. The exercise is done both in data and MC. Fig. 4.26 shows the ratio of the restricted versus nominal jet spectra together with the double-ratio data/MC. The error bars display the statistical uncertainty that is estimated with the bootstrap method. 10^4 pseudoexperiments of each spectrum are generated.

In both data and MC, a non-closure (decrease) of $\sim$1 % is observed. This result is consistent with the observations in Sec. 3.4 that the $\mathrm{BCH}_{\mathrm{cor,\,jet}}$ correction tends to overcalibrate jets falling in a non-operational TileCal module. However, the double-ratio data/MC shows no statistically significant deviations from one. The residual effects of the non-operational TileCal modules are thus corrected by the unfolding procedure.

4.5.2 In-time pile-up

The jet-level correction on pile-up is described in [42]. However, the inclusive jet spectra might be affected by potential residual effects due to pile-up. In this section, the impact of in-time pile-up in the inclusive jet cross-section is described. The inclusive jet detector-level spectra are measured on data subsamples corresponding to different ranges of μ_{act}. The spread of the different measurements around the nominal detector-level spectrum is compared with the uncertainty arising from the jet-level pile-up correction determination.

To perform the check, luminosity for each μ_{act} subsample and for each trigger is determined in the following way. If a jet fires a given trigger, the μ_{act} distribution is filled with μ_{act}. This entry is assigned a weight of μ_{act} because it is proportional to the luminosity taken in the given bunch-crossing. For each lumiblock, the obtained μ_{act} distribution is normalized to the luminosity taken by given trigger in that lumiblock. The luminosity-normalized per-lumiblock μ_{act} distributions are summed to get the total μ_{act} distribution corresponding to given trigger. The luminosity that corresponds to a μ_{act} range $(\mu_{\mathrm{act}}^{\mathrm{min}}, \mu_{\mathrm{act}}^{\mathrm{max}})$ is computed as an integral of the μ_{act} distribution over the given interval. This procedure was developed in the analysis group. It is carefully described in [89]. The document also explains

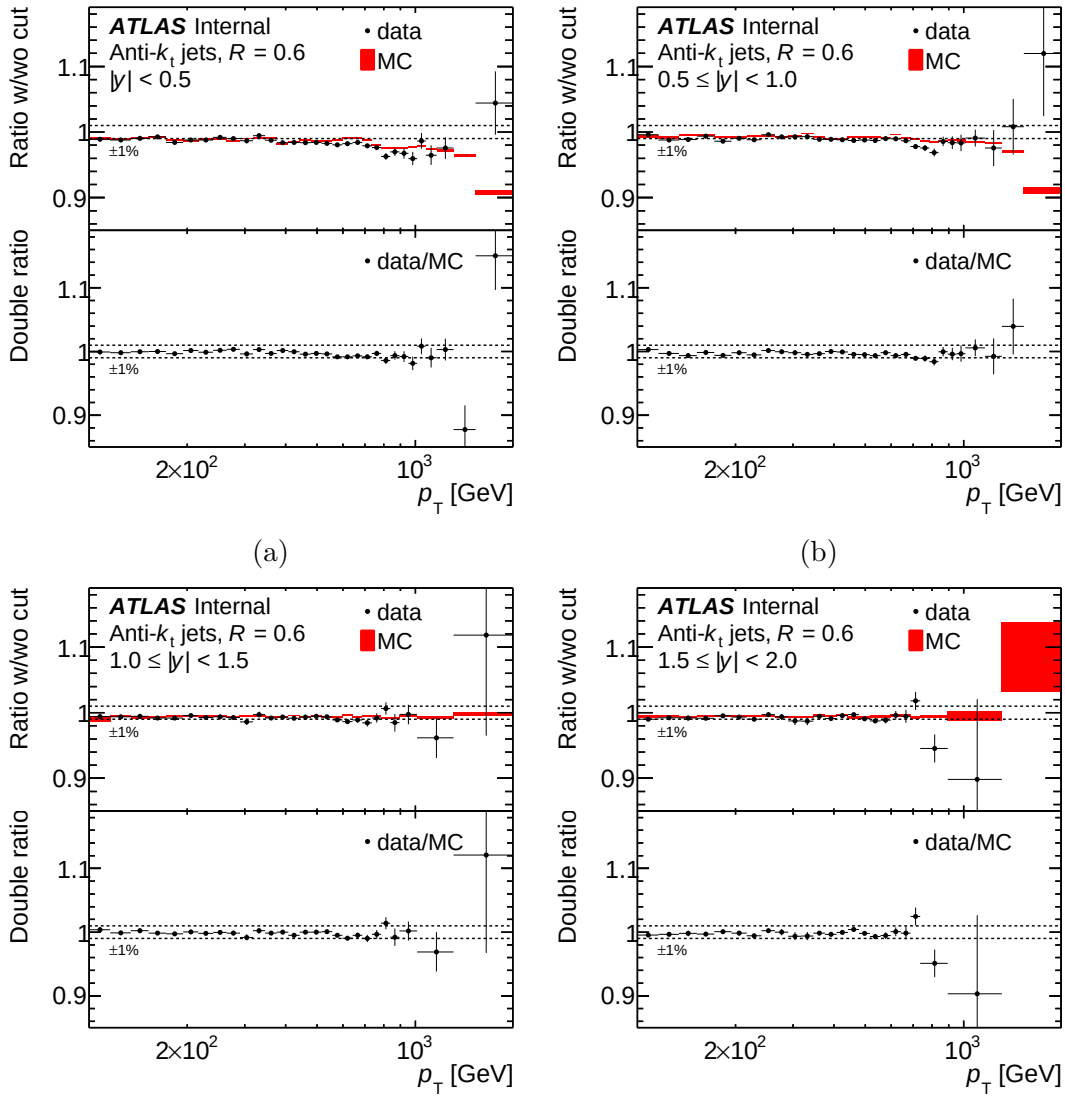

Figure 4.26: The impact of non-operational TileCal modules on the detector-level inclusive jet spectra. Potentially affected y-bins are shown: $|y| < 0.5$ (a), $0.5 <= |y| < 1.0$ (b), $1.0 <= |y| < 1.5$ (c) , $1.5 <= |y| < 2.0$ (d). The upper plot always shows a ratio of the restricted versus nominal jet spectra for both data (black points) and MC (red band). The bottom plot displays the double-ratio data/MC. The dashed lines highlight a 1 % band around 1. Plots correspond to anti-k_t jets with $R = 0.6$.

why μ_{act} is used instead of NPV that is a more intuitive quantification of the in-time pile-up. The reasons are:

- p_T bias of the NPV distributions arising from the trigger requirement.
- Tracking inefficiency of the primary vertices reconstruction.

The ratios of inclusive jet detector-level spectra measured in different ranges of μ_{act} are shown in Fig. 4.27 (4.28) for anti-k_t jets with $R = 0.6$ ($R = 0.4$). No μ_{act} range shows a statistically significant deviation from the uncertainty band due

to the determination of the jet-level pile-up correction. Therefore, no additional pile-up uncertainty is assigned.

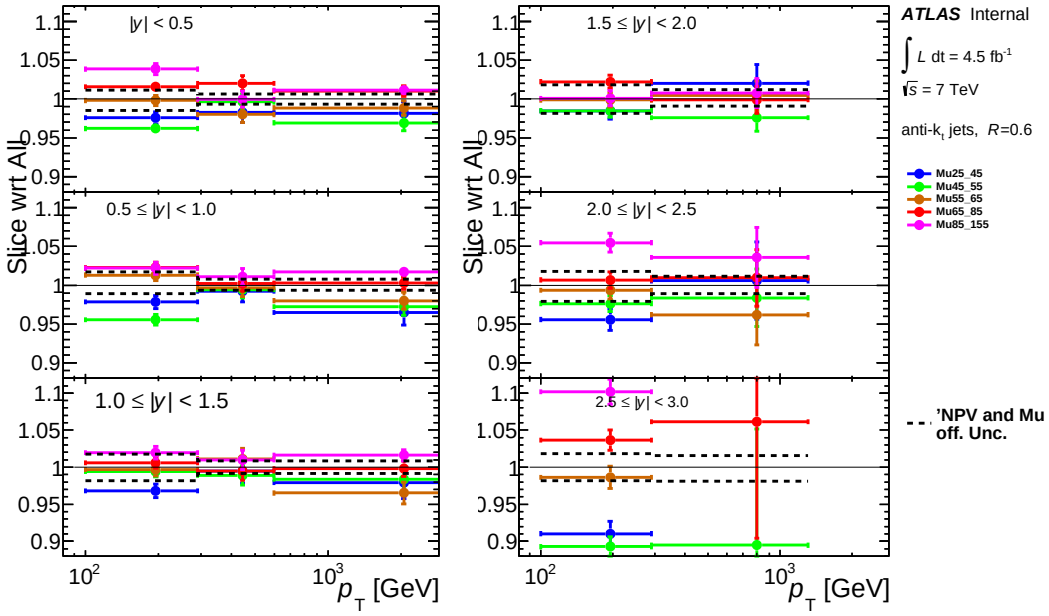

Figure 4.27: The comparison of the nominal inclusive jet detector-level spectrum with the spectra measured in different ranges of μ_{act}. The different pointsets correspond to different μ_{act} ranges. The dashed black lines display the uncertainty arising from the determination of the jet-level pile-up correction. All the y-bins are shown for anti-k_t jets with $R = 0.6$.

4.5.3 Pile-up reweighting of MC

As discussed in Sec. 4.2.3, the jets in MC are weighted to match the MC μ_{avg} distribution with data. This is done separately for the jet p_T ranges that correspond to each trigger. This procedure might increase the statistical uncertainty or bring some undesired bias. This section describes a check of those two points.

The nominal inclusive jet cross-section is unfolded with the reweighted MC. In the presented check, the MC is kept un-weighted and it is used for unfolding. Apart from the pile-up weights, the TM is built in the same way as the nominal weighted one. To estimate the statistical uncertainty of the measurement, 10^4 fluctuated replicas of the TM are generated. The set of detector-level data spectra used is the same as for the nominal measurement.

Fig. 4.29 shows a comparison of the spectra unfolded with and without MC weighting. No sizable difference is observed. A discrepancy is present in the lowest p_T-, highest y-bin. This bin is expected to be the most affected by pile-up. Therefore, the more precise pile-up description in MC is necessary; it is obtained with the MC weighting. The statistical uncertainties of the two approaches are also compared. The method with MC weighting yields an overall statistical uncertainty of almost the same size as the method without weighting. Therefore, one can conclude that the effective MC statistics is not reduced too much if the MC weighting is used.

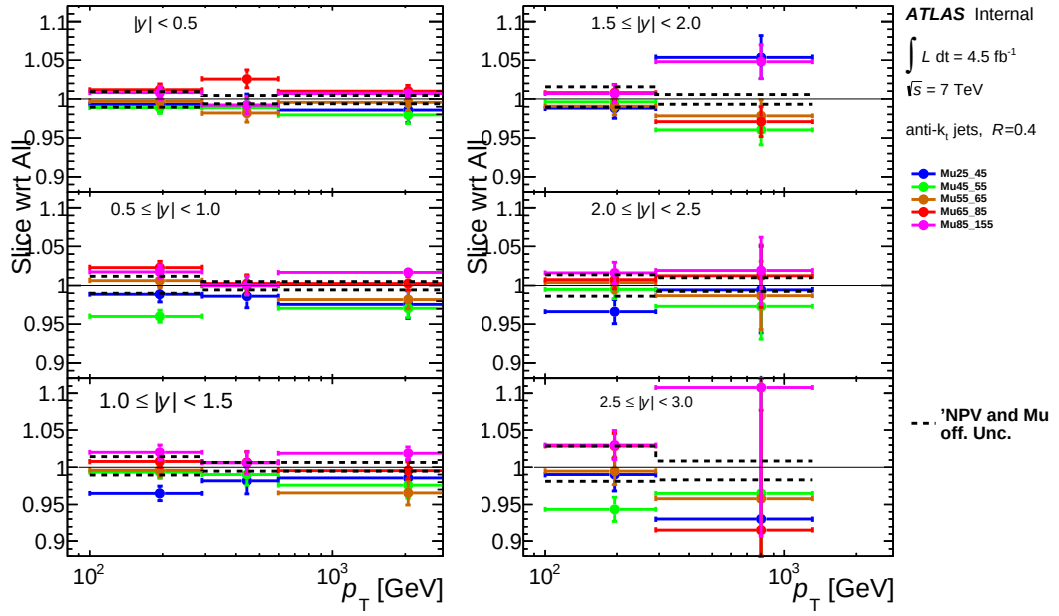

Figure 4.28: The comparison of the nominal inclusive jet detector-level spectrum with the spectra measured in different ranges of μ_{act}. The different pointsets correspond to different μ_{act} ranges. The dashed black lines display the uncertainty arising from the determination of the jet-level pile-up correction. All the y-bins are shown for anti-k_{t} jets with $R = 0.4$.

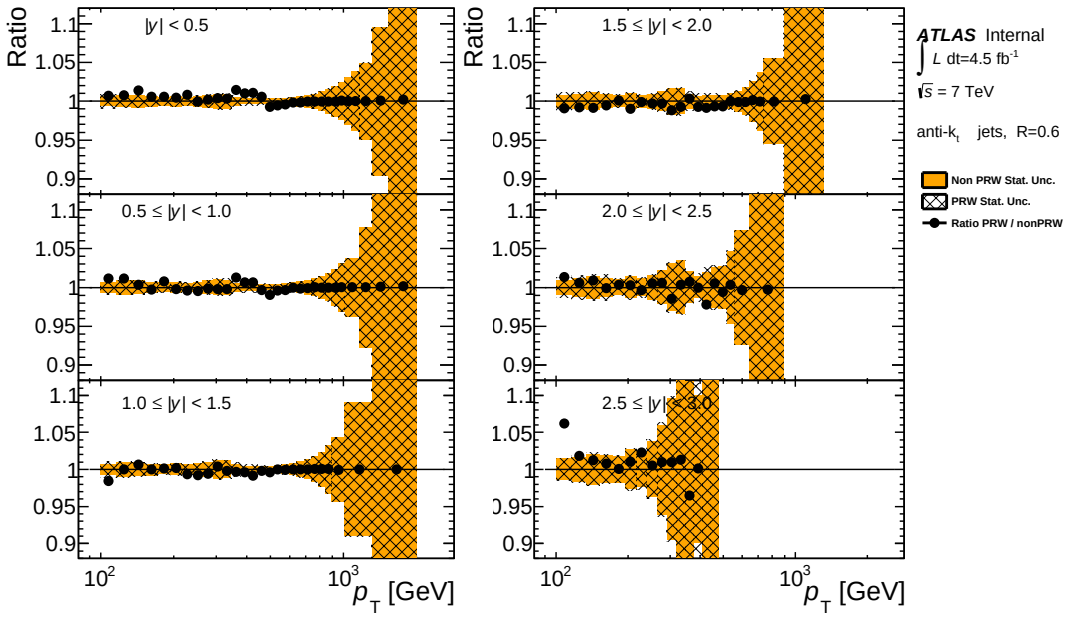

Figure 4.29: The inclusive jet cross-section unfolded with the pile-up-weighted TM and with the un-weighted one. Both are scaled to the spectrum obtained without weighting. The relative statistical uncertainty (due to both MC and data statistics) is shown for both cases. All the y-bins are shown for anti-k_{t} jets with $R = 0.6$.

4.5.4 High-p_{T} jets

The 2011 7 TeV jet spectra reach an unprecedented high-p_{T} region up to 2 TeV. Jets in this region deserve a closer look to make sure that they are properly measured and that the sample is not contaminated by fakes caused by e.g. high calorimeter noise or overcalibration. The highest-p_{T} jets from each y-bin are checked by eye – with the use of ATLAS event displays. This was done for the anti-k_{t} $R = 0.6$ collection. The number of events checked is ∼80. About 70 events are nice dijet (or multijet) events with no apparent problem. But 15 jets originate in events with unnatural or even unphysical topology.

Detector problems

An example is shown in Fig. 4.30. There is an event affected by a coherent noise in the EM calorimeter. All the jets in the event are rejected by the jet cleaning algorithm except for the highest-p_{T} one. Unfortunately, the event was not tagged by a dedicated algorithm detecting the coherent noise problems because the algorithm requires two consecutive affected events. The accepted fake jet has $p_{\mathrm{T}} = 2.6$ TeV and $\eta = 2.9$. It is clearly unphysical because it would break the energy and momentum conservation in pp-collisions. The fake jet was not tagged by the jet cleaning procedure because the cut on objects affected by the coherent noise requires the "jet" $|\eta| < 2.8$. All the jets in the potentially problematic η-region $2.8 <= |\eta| < 3.0$ are checked in all p_{T}-range. No other jets affected by the coherent noise are found.

Overcalibrated jets

Three jets have unrealisticaly large p_{T} due to overcalibration. They all fall in the highest y-bin. They get overcalibrated with the $\mathrm{BCH}_{\mathrm{cor,\,jet}}$ correction on bad channels. An example is shown in Fig. 4.31 where there is a three-jet event. In the event display, the three jets are balanced in the transverse plain because the $\mathrm{BCH}_{\mathrm{cor,\,jet}}$ correction is not used. However, the data analysis does use the correction and the highest-p_{T} jet gets overcalibrated to $p_{\mathrm{T}} = 1.8$ TeV; it is the jet that goes to the left in the schematic (η, ρ) detector map.

After these results it was decided not to use the $\mathrm{BCH}_{\mathrm{cor,\,jet}}$ correction for jets with $|\eta| \geq 1.5$. It is only applied to jets with $|\eta| < 1.5$, i.e. in the region covered by TileCal, for which the correction is carefully tested. In the region $|\eta| \geq 1.5$, the default $\mathrm{BCH}_{\mathrm{cor,\,cell}}$ correction is kept.

Other problems

11 other jets are suspicious. They appear in events with very high $E_{\mathrm{T}}^{\mathrm{miss}}$ because they are not balanced in the transverse plane. They have different pseudorapidities, therefore any specific detector region cannot be blamed. They do not affect the inclusive jet spectra significantly because they fall into the (p_{T}, y)-bins where there are enough other jets. However, the important question is whether there are jets at lower p_{T} with similar properties. The answer is the matter of this section.

All the 11 jets under scrutiny can be tagged with a simple cut based on $E_{\mathrm{T}}^{\mathrm{miss}}$. The cut compares the leading jet transverse momentum $p_{\mathrm{T}}^{\mathrm{lead}}$ with $E_{\mathrm{T}}^{\mathrm{miss}}$.

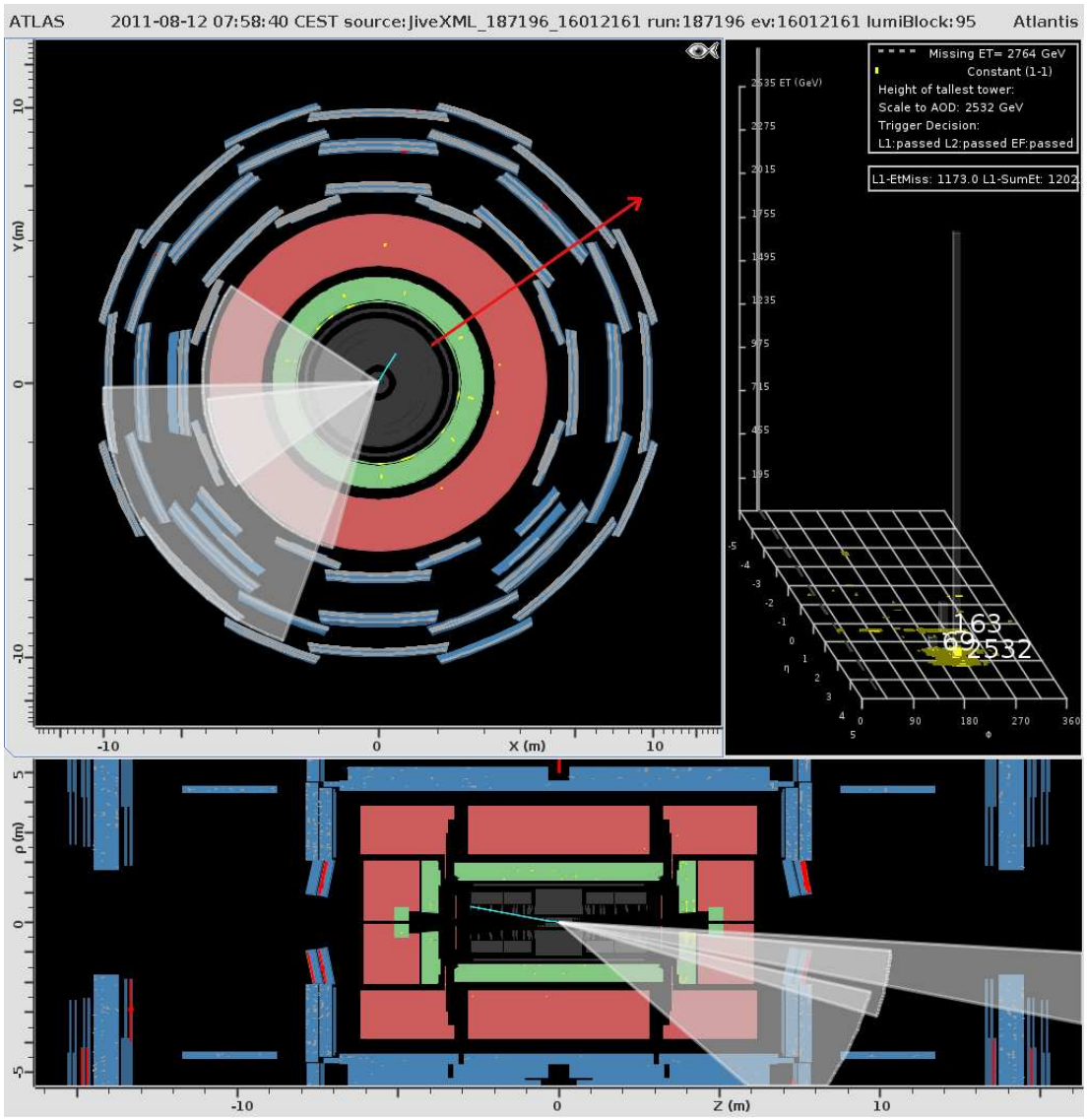

Figure 4.30: Display of ATLAS event 16012161 (run 187196) with very high-p_{T} jet: $p_{\mathrm{T}} = 2.6$ TeV at $\eta = 2.9$. The top left figure represents the (ϕ, ρ) projection of the ATLAS detector. The bottom figure shows the (η, ρ) map. On the top right figure there is a (η, ϕ) map of the energy depositions. The grey/black area in the middle of the ATLAS detector represents the inner detector. Reconstructed tracks are displayed by the blue lines. The green (red) area shows the EM (hadronic) calorimeter. Energy depositions in the calorimeters are displayed by the yellow spots. The blue system around the calorimeters are muon chambers. Hits in muon chambers are displayed by the red colour. The white cones represent jets with $p_{\mathrm{T}} > 50$ GeV. The red arrow shows the missing transverse energy $E_{\mathrm{T}}^{\mathrm{miss}}$.

It fires if $E_{\mathrm{T}}^{\mathrm{miss}}/p_{\mathrm{T}}^{\mathrm{lead}} \geq 0.7$. The cut is used in an alternative measurement of the inclusive jet spectrum at the detector-level. It is applied on top of all the cuts used in the nominal measurement. The resulting spectrum is compared with the nominal one. The statistical uncertainty of the ratio is estimated with the use of 10^3 pseudoexperiments. In MC, the alternative detector-level spectrum is exactly the same as the nominal one. Fig. 4.32 shows the spectra comparison in data for anti-k_{t} jets with $R = 0.6$. The spectra agree with each other with one

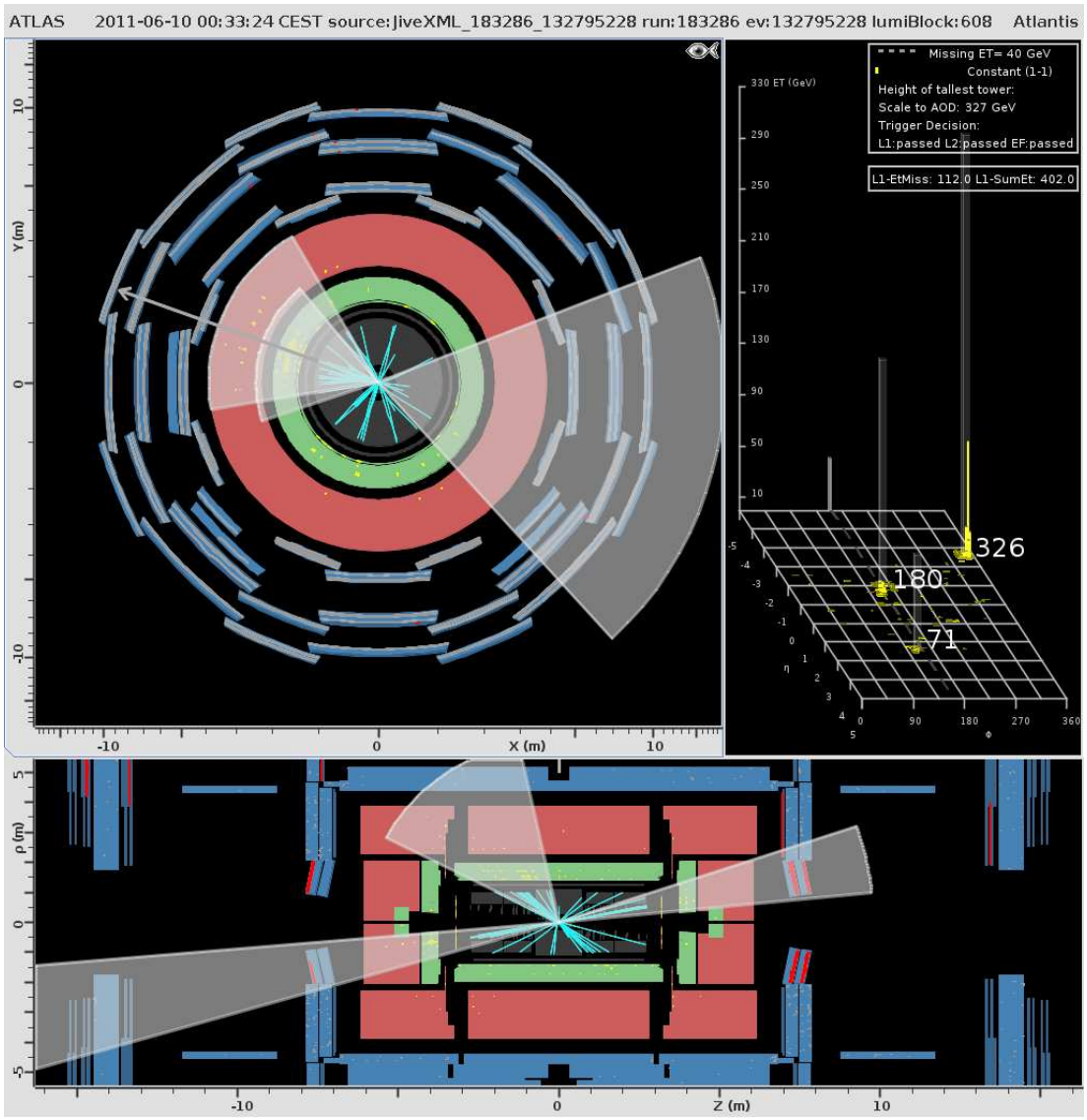

Figure 4.31: ATLAS event display of event 132795228 (run 183286) with very high-p_{T} jet: $p_{\mathrm{T}} = 1.8$ TeV at $\eta = -2.5$. For details about the displayed objects see the caption of the Fig. 4.30.

permille difference at most. This observation means that the suspicious jets (both known and potential) have negligible impact on the measurement. Therefore, no additional cut or uncertainty is needed.

4.6 Results

The double differential inclusive jet cross-section is measured as a function of jet p_{T} and y. The data were recorded by the ATLAS experiment at the LHC in 2011; pp-collisions are studied at 7 TeV centre-of-mass energy. The total integrated luminosity is 4.5 fb^{-1}. Jets are identified with the anti-k_{t} algorithm. Two values of its R-parameter are used: $R = 0.4$ and $R = 0.6$. The phase space region covered is 100 GeV $\leq p_{\mathrm{T}} \lesssim 2$ TeV, $|y| < 3.0$. The high-p_{T} kinematic reach is an unprecented achievement. The measurement benefits from the precise jet

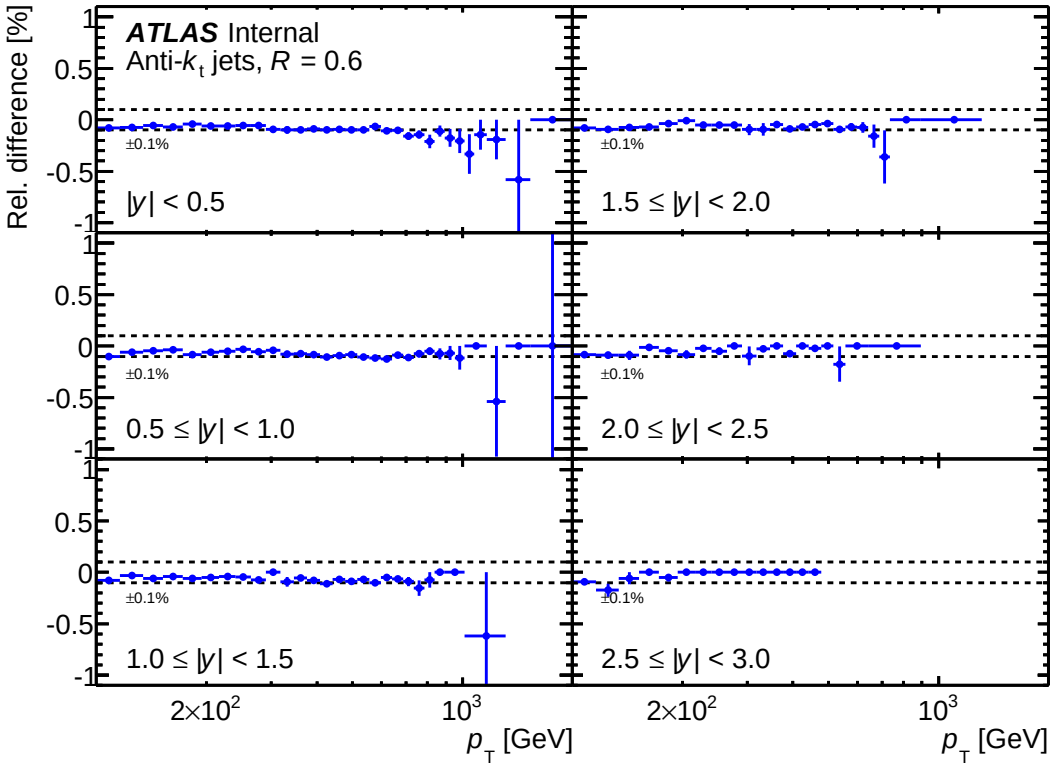

Figure 4.32: Ratio of the inclusive jet detector-level spectrum measured using an additional cut based on $E_{\mathrm{T}}^{\mathrm{miss}}$ over the nominal spectrum. The dashed black lines highlight a one permille band around zero. All the y-bins are shown for anti-k_{t} jets with $R = 0.6$.

energy calibration which is the dominant source of the experimental uncertainty. Many other sources are carefully studied. The total systematic uncertainty is below 10 % up to 1 TeV in the lowest y-bin. The statistical uncertainty is below the systematic one in all the (p_{T}, y)-bins. The unfolding procedure is carefully chosen and set not to introduce much bias to the spectrum while keeping the statistical uncertainty sufficiently low. The measurement is robust against effects like pile-up, detector defects or misidentified high-p_{T} objects.

Fig. 4.33 shows the inclusive jet cross-section together with the theoretical prediction based on the NLO QCD calculation with the CT10 PDF set. The prediction is corrected for the EW radiative and the QCD non-perturbative effects. Ratio of the prediction with respect to data is shown in Fig. 4.34 (4.35) for anti-k_{t} jets with $R = 0.4$ ($R = 0.6$). In the figures, two more theoretical predictions are included; they use different PDF sets, namely MSTW2008 and NNPDF 2.1. Fig. 4.36 and 4.37 show two additional theoretical predictions based on HERAPDF 1.5 and ABM 11. Generally, the theoretical predictions agree with data within uncertainty. Only ABM 11 describes data poorly. The reason might be that ABM 11 is determined with the NNLL precision whereas the parton level cross-section is computed at NLO. Thus, the PDF is not fully compatible with the NLOJET++ calculation.

An interesting observation is that the theory systematically underestimates the cross-section measured with anti-k_{t}, $R = 0.6$ jets in the low y-bins. It is not the case for $R = 0.4$ jets.

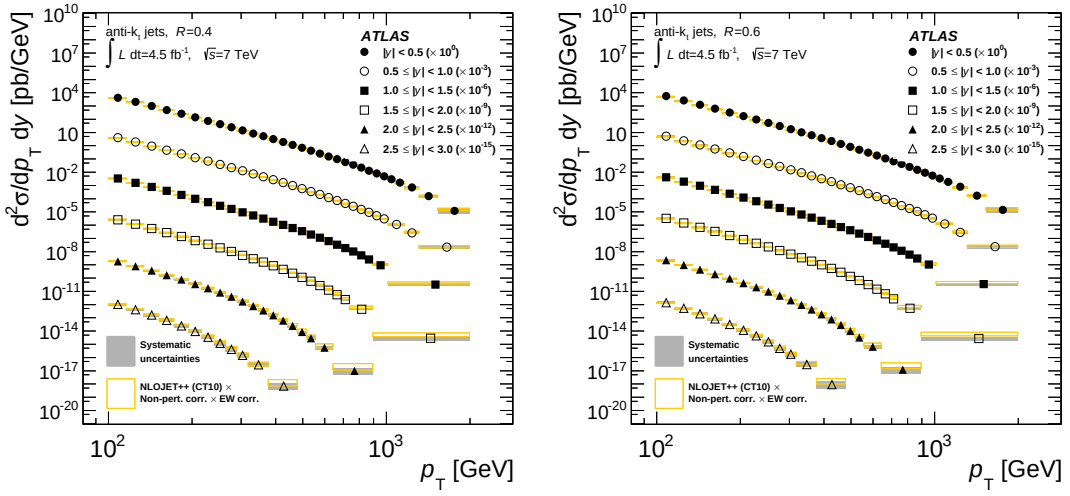

(a) (b)

Figure 4.33: The inclusive jet cross-section measured with the anti-k_t jets with $R = 0.4$ (a) and $R = 0.6$ (b). The grey band displays the total systematic uncertainty. The statistical uncertainty is also plotted but it is invisible. The theoretical prediction (yellow band) is based on the NLO QCD calculation with the CT10 PDF set. The prediction is corrected for the EW radiative and the QCD non-perturbative effects.

The experimental results are also qualitatively compared with the POWHEG predictions. POWHEG is interfaced to PYTHIA with two different tunes: AUET2B and Perugia 2011. Both predictions are evaluated for anti-k_t jets with $R = 0.4$ and 0.6. The comparison is shown in Fig. 4.38 and 4.39. Unlike NLOJET++, POWHEG describes both the $R = 0.4$ and $R = 0.6$ anti-k_t jet spectra equally well in the lowest two y-bins. In this rapidity region, there is a slight shape difference between POWHEG and data. No such difference is observed in the higher y-bins where the POWHEG prediction describes data well. Unfortunately, no quantitative statement can be made due to the lack of the theoretical uncertainty.

4.6.1 Comparison with the 2010 results

As stated already, the inclusive jet cross-section in pp-collisions at 7 TeV centre-of-mass energy was measured by ATLAS on the data sample taken in 2010. The differences of the 2011 measurement were briefly discussed at the very beginning of Sec. 4. The interesting question is the compatibility of the two results. To answer this question, the 2011 cross-section is remeasured with the (p_T, y)-binning used in 2010. Nothing is changed apart from the binning: all the cuts and algorithms are kept. The comparison is shown in Fig. 4.40 and 4.41 for the five lowest y-bins covering the common region in y. The two measurements are compatible within uncertainties. The 2011 systematic uncertainty is smaller than the 2010 one on most of the phase space. The statistical uncertainty is smaller in all the (p_T, y)-bins in 2011.

There is one important difference between the 2010 and 2011 measurements: the 2010 one reaches lower jet p_T down to 20 GeV and higher y up to 4.4. The

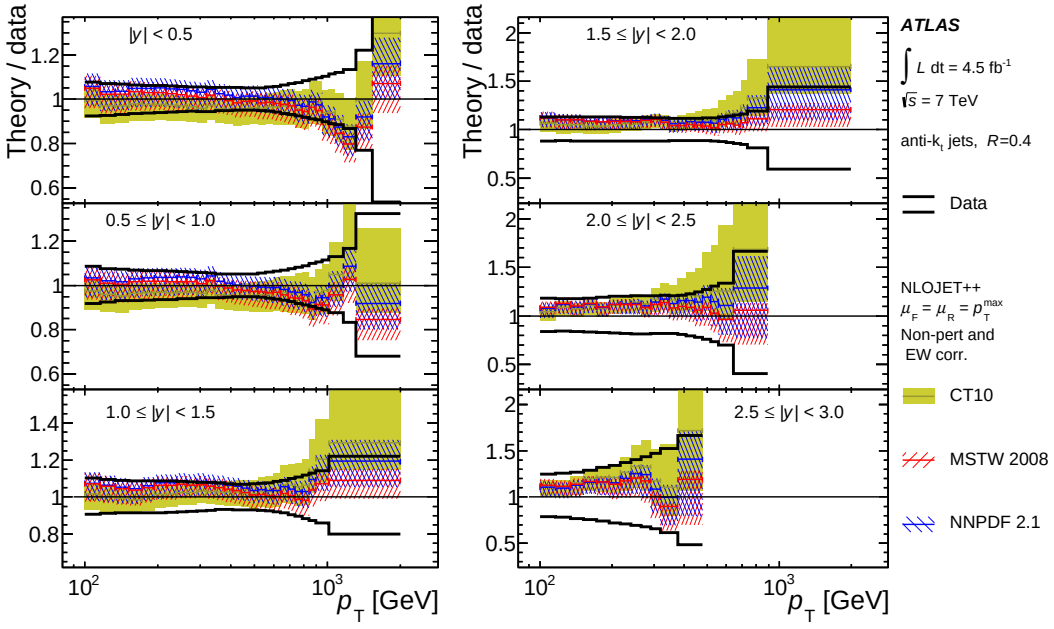

Figure 4.34: Ratio of three theoretical predictions for the inclusive jet cross-section over data (the solid black line at one): based on CT10 (yellow band), MSTW2008 (red hatched band) and NNPDF 2.1 (blue hatched band). All the y-bins are shown for anti-k_t jets with $R = 0.4$.

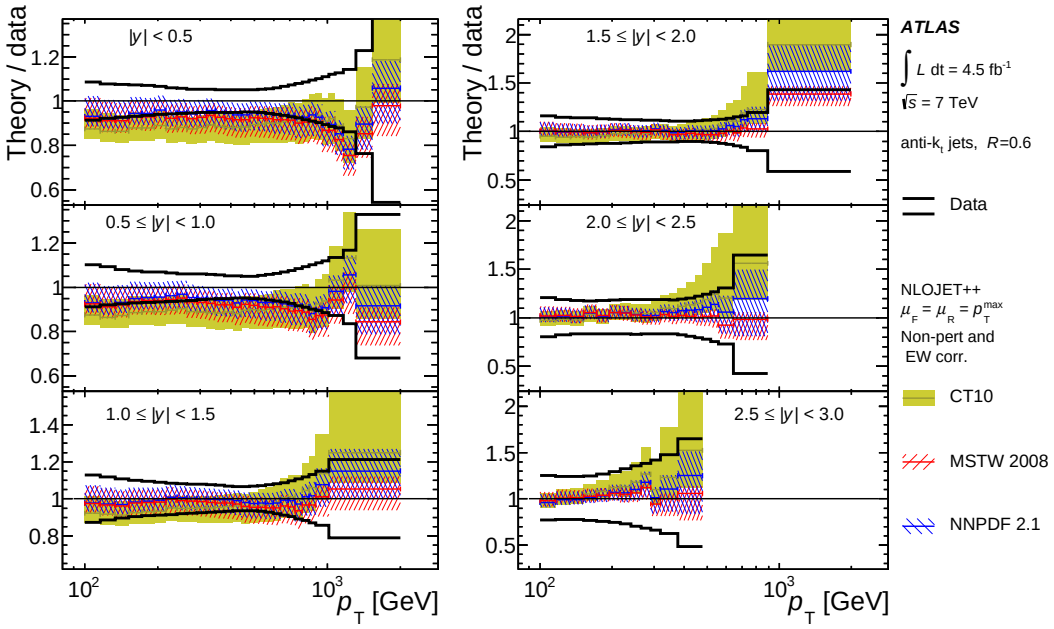

Figure 4.35: Ratio of three theoretical predictions for the inclusive jet cross-section over data (the solid black line at one): based on CT10 (yellow band), MSTW2008 (red hatched band) and NNPDF 2.1 (blue hatched band). All the y-bins are shown for anti-k_t jets with $R = 0.6$.

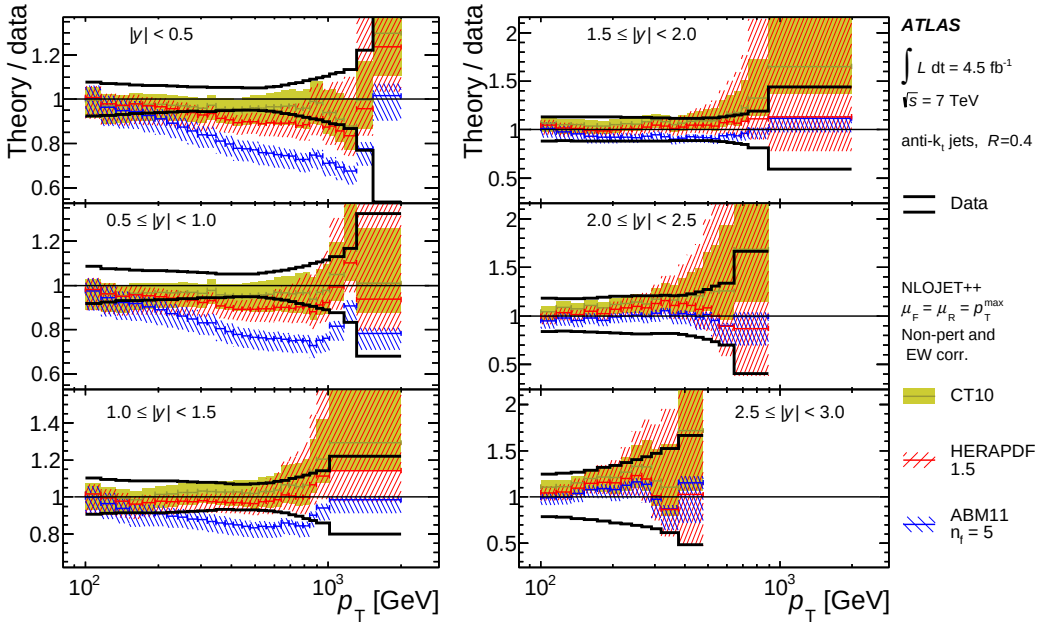

Figure 4.36: Ratio of three theoretical predictions for the inclusive jet cross-section over data (the solid black line at one): based on CT10 (yellow band), HERAPDF 1.5 (red hatched band) and ABM 11 (blue hatched band). All the y-bins are shown for anti-k_t jets with $R = 0.4$.

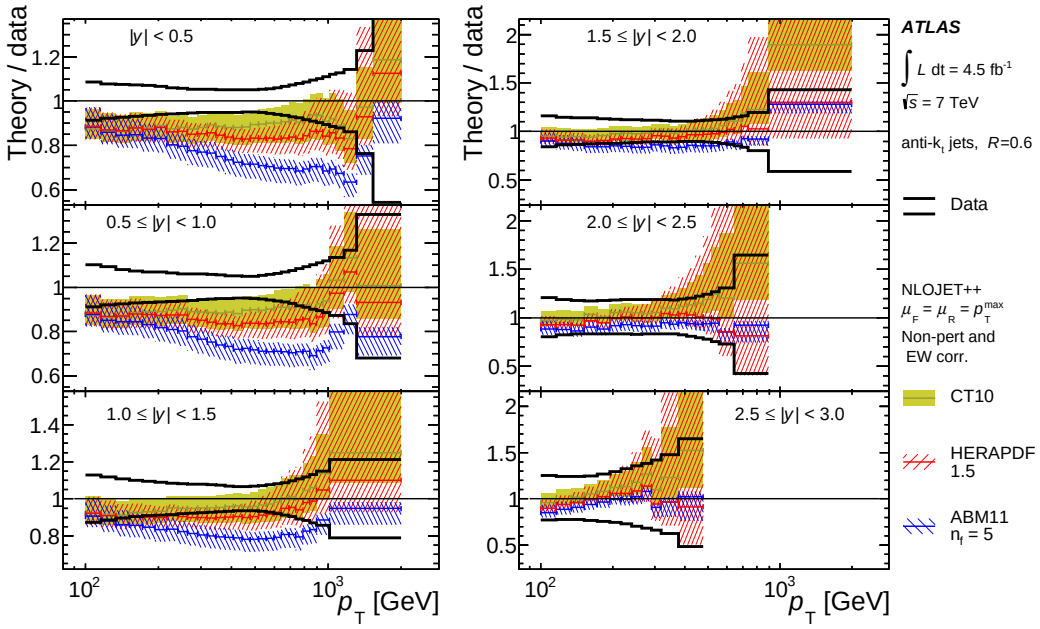

Figure 4.37: Ratio of three theoretical predictions for the inclusive jet cross-section over data (the solid black line at one): based on CT10 (yellow band), HERAPDF 1.5 (red hatched band) and ABM 11 (blue hatched band). All the y-bins are shown for anti-k_t jets with $R = 0.6$.

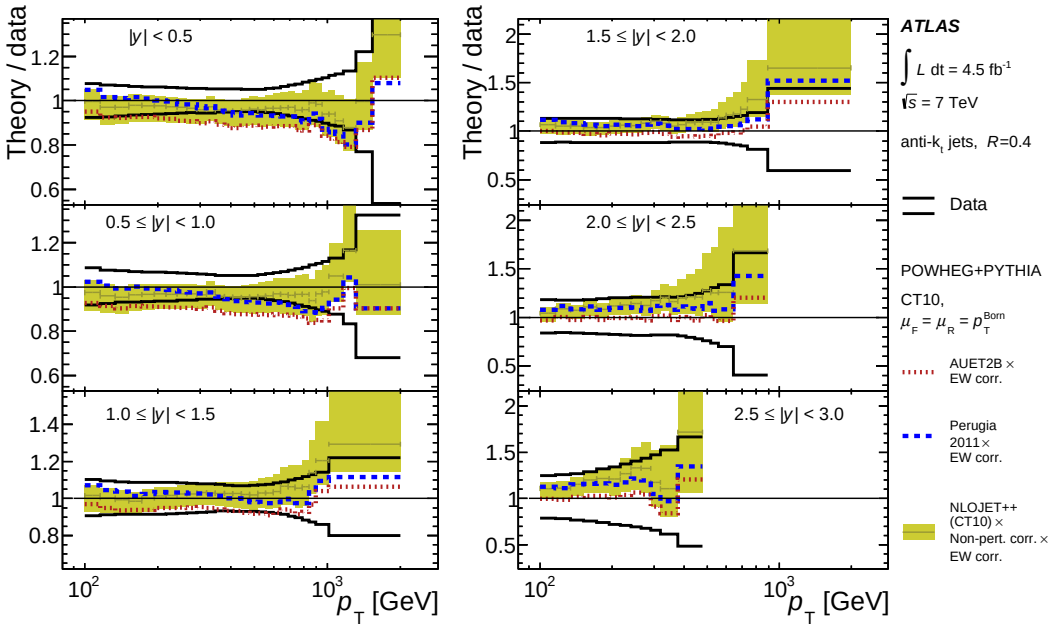

Figure 4.38: Ratio of the POWHEG theoretical predictions for the inclusive jet cross-section over data. POWHEG is interfaced to PYTHIA with the AUET2B tune (dotted red line) and with the Perugia 2011 tune (dashed blue line). For reference, the NLOJET++ prediction based on the CT10 PDF set is shown (the yellow band). All the y-bins are shown for anti-k_t jets with $R = 0.4$.

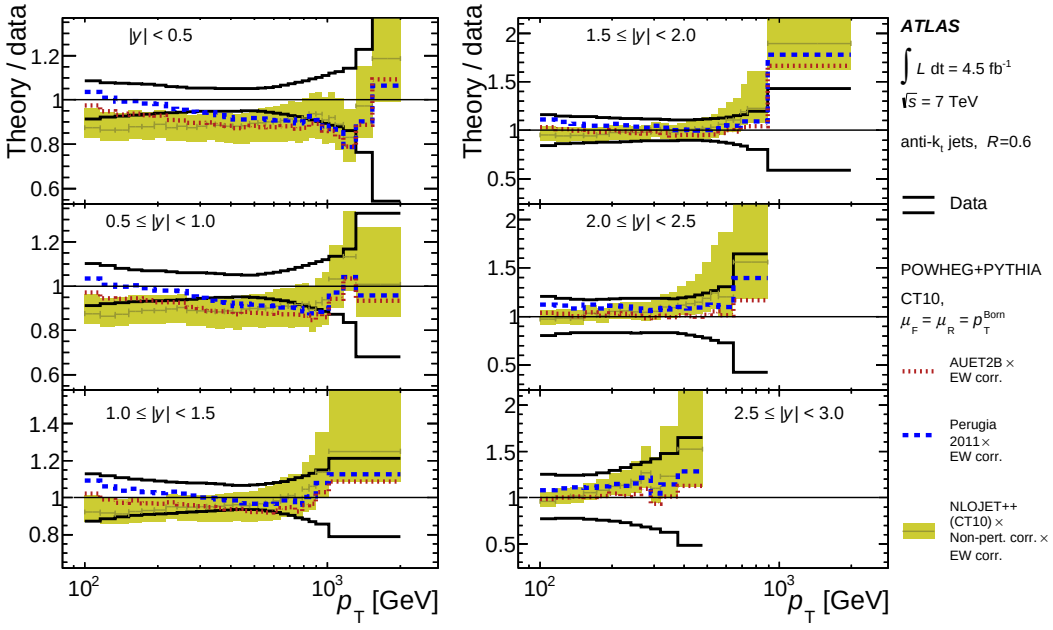

Figure 4.39: Ratio of the POWHEG theoretical predictions for the inclusive jet cross-section over data. POWHEG is interfaced to PYTHIA with the AUET2B tune (dotted red line) and with the Perugia 2011 tune (dashed blue line). For reference, the NLOJET++ prediction based on the CT10 PDF set is shown (the yellow band). All the y-bins are shown for anti-k_t jets with $R = 0.6$.

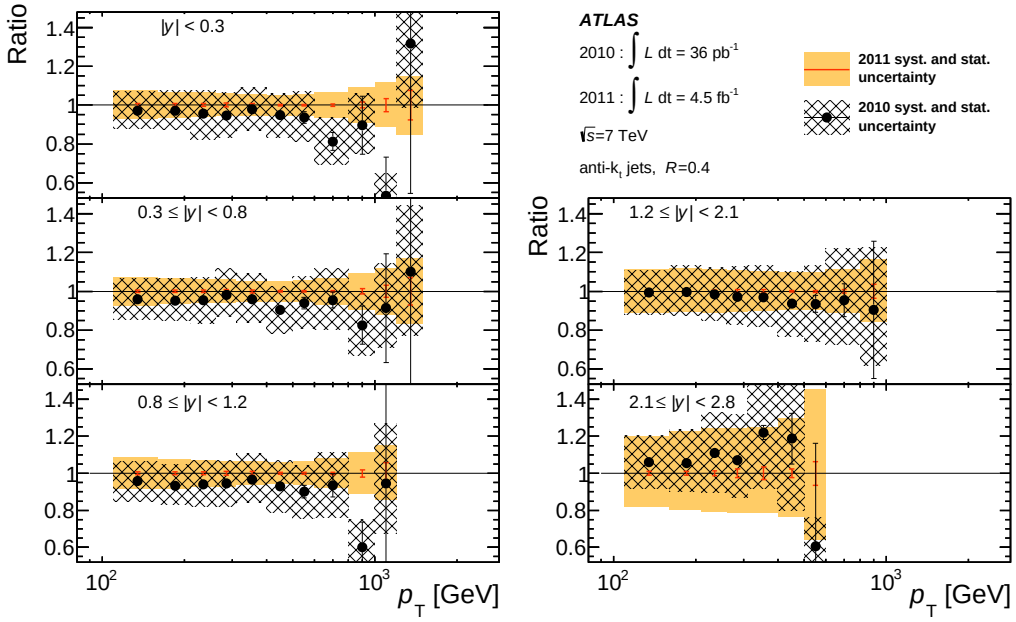

Figure 4.40: The inclusive jet cross-section measured in pp-collisions at 7 TeV on the 2010/37 pb^{-1} (black points) and the 2011/4.5 fb^{-1} (solid black line) data samples. The measured values are scaled to the 2011 cross-section. The relative systematic uncertainty of the two measurements is displayed by the hatched black band (2010) and orange band (2011). The error bars show the relative statistical uncertainty of the measurements. Five lowest y-bins are shown. These bins almost cover the y-overlap of the two measurements. Results correspond to anti-k_t jets with $R = 0.4$.

reason is lower pile-up. A comparison of the 2010 and 2011 p_T-coverage is shown in Fig. 4.42 for two selected y-regions for anti-k_t jets with $R = 0.6$.

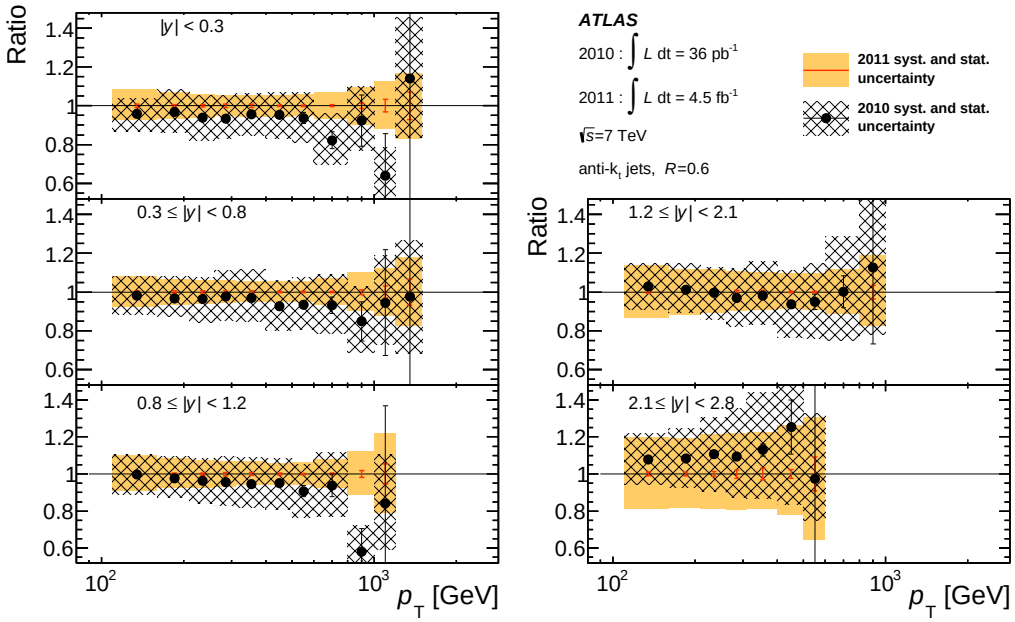

Figure 4.41: The inclusive jet cross-section measured in pp-collisions at 7 TeV on the 2010/37 pb^{-1} (black points) and the 2011/4.5 fb^{-1} (solid black line) data samples. The measured values are scaled to the 2011 cross-section. The relative systematic uncertainty of the two measurements is displayed by the hatched black band (2010) and orange band (2011). The error bars show the relative statistical uncertainty of the measurements. Five lowest y-bins are shown. These bins almost cover the y-overlap of the two measurements. Results correspond to anti-k_t jets with $R = 0.6$.

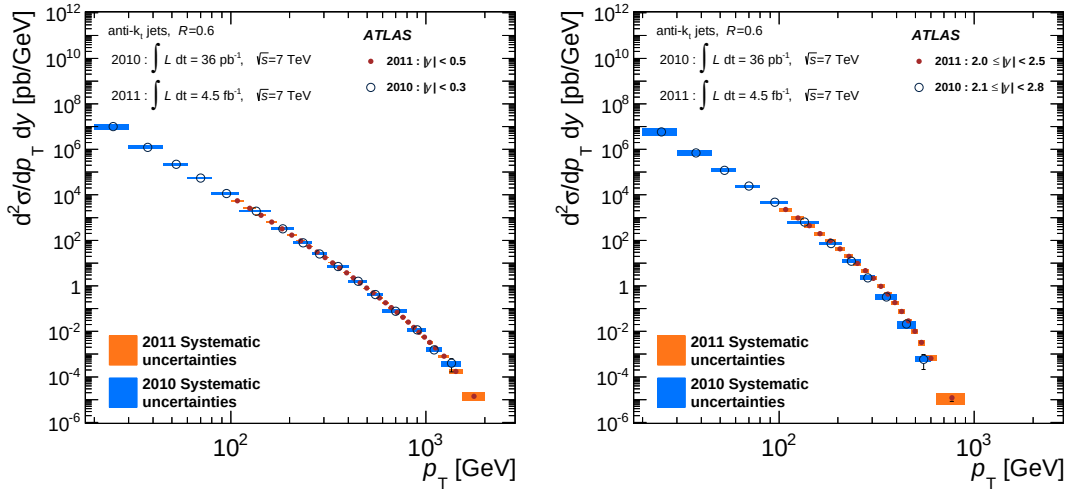

(a) (b)

Figure 4.42: The inclusive jet cross-section measured in pp-collisions at 7 TeV on the 2010/37 pb^{-1} (open circles) and the 2011/4.5 fb^{-1} (orange points) data samples. Two representative y-regions are shown for anti-k_t jets with $R = 0.6$.

Conclusion

The thesis has two main parts describing topics to which the author significantly contributed. Both of them are based on the same data sample recorded by the ATLAS experiment in pp-collisions at 7 TeV centre-of-mass energy in 2011. The integrated luminosity is 4.5 fb^{-1}.

The first part (Chap. 3) focuses on software correction of TileCal non-operational modules impact on the jet reconstruction. It compares the performance of two different TileCal bad channel corrections. The method used is based on p_{T} balance of the two leading-p_{T} jets in dijet events. It is a tag-and-probe in-situ technique where one jet is used to probe the problematic detector region; the other jet is used as a tag and it is required to be precisely reconstructed. One tested bad channel correction ($\text{BCH}_{\text{cor, cell}}$) uses the information from neighbour cells to estimate the energy contained in the bad cells. The other correction ($\text{BCH}_{\text{cor, jet}}$) is based on the knowledge of the jet shapes. Neither of the two corrections is ideal. $\text{BCH}_{\text{cor, cell}}$ underestimates (overestimates) the non-operational module impact if a jet axis points to the module (to the neighbour region of the module). The non-closure is about 10 %. $\text{BCH}_{\text{cor, jet}}$ overestimates the impact by $\sim$5 % if the jet axis points to the module. The MC reasonably describes all the observed effects. Due to the smaller non-closure of $\text{BCH}_{\text{cor, jet}}$, this correction is chosen for the inclusive jet cross-section measurement in the central region $|\eta| < 1.5$.

The second part (Chap. 4) of the thesis describes the author's contribution to the ATLAS inclusive jet cross-section measurement in pp-collisions at 7 TeV centre-of-mass energy. It describes the data sample, jet selection, MC and its comparison with data. The unfolding procedure is discussed together with its connection to the statistical uncertainty and binning. A lot of attention is paid to the systematic uncertainty, its sources, evaluation and shape. The robustness of the measurement against several effects is studied in detail. The Chap. 4 also briefly describes the evaluation of the theoretical predictions. They are based on NLO QCD calculation, NP corrections derived from MC and EW radiative corrections. An alternative approach uses POWHEG interfaced to PYTHIA with two tunes, AUET2B and Perugia 2011. Finally, the measured cross-section is presented for both the two jet collections, anti-k_{t}, $R = 0.4,\ 0.6$. The results substantially benefit from the precise jet energy calibration and from the large statistics of the data sample. They are compared to the theoretical predictions based on NLOJET++ evaluated using five different PDF sets. Most of the predictions describe data within uncertainty. The only PDF set that yields a significant disagreement with data is ABM 11. An interesting general tension is found between the measurements with $R = 0.4$ and $R = 0.6$ jets. In the low rapidity region, the theoretical predictions based on NLOJET++ seem to underestimate data in the case of $R = 0.6$ jets whereas no such effect is observed for the jets with $R = 0.4$. On the other hand, the predictions computed with POWHEG describe both the two jet spectra equally well.

Bibliography

[1] L. Evans and P. Bryant, *LHC Machine*, JINST **3** (2008) S08001.

[2] J. Hořejší, *Fundamentals Of Electroweak Theory*. Karolinum Press, 2003. http://books.google.cz/books?id=JGkFAQAACAAJ.

[3] J. Chýla, *Quarks, partons and Quantum Chromodynamics*. 2004. http://www-ucjf.troja.mff.cuni.cz/lecture_notes_cz.php.

[4] J. M. Campbell, J. Huston, and W. Stirling, *Hard Interactions of Quarks and Gluons: A Primer for LHC Physics*, Rept.Prog.Phys. **70** (2007) 89, arXiv:hep-ph/0611148 [hep-ph].

[5] F. Halzen and A. Martin, *Quarks and Leptons*. Wiley, 1984. http://books.google.cz/books/about/Quarks_and_leptons.html?id=zwDvAAAAMAAJ&redir_esc=y.

[6] ATLAS Collaboration, G. Aad et al., *Observation of a new particle in the search for the Standard Model Higgs boson with the ATLAS detector at the LHC*, Phys.Lett. **B716** (2012) 1–29, arXiv:1207.7214 [hep-ex].

[7] CMS Collaboration, S. Chatrchyan et al., *Observation of a new boson at a mass of 125 GeV with the CMS experiment at the LHC*, Phys.Lett. **B716** (2012) 30–61, arXiv:1207.7235 [hep-ex].

[8] M. Peskin and D. Schroeder, *An Introduction to Quantum Field Theory*. Perseus Books, 1995. http://www.amazon.com/Introduction-Quantum-Theory-Frontiers-Physics/dp/0201503972.

[9] M. Cacciari, G. P. Salam, and G. Soyez, *The Anti-k(t) jet clustering algorithm*, JHEP **0804** (2008) 063, arXiv:0802.1189 [hep-ph].

[10] S. D. Ellis and D. E. Soper, *Successive combination jet algorithm for hadron collisions*, Phys.Rev. **D48** (1993) 3160–3166, arXiv:hep-ph/9305266 [hep-ph].

[11] M. Dasgupta, L. Magnea, and G. P. Salam, *Non-perturbative QCD effects in jets at hadron colliders*, JHEP **0802** (2008) 055, arXiv:0712.3014 [hep-ph].

[12] G. Salam lectures on Jets at Hadron Colliders. http://indico.cern.ch/event/115079/.

[13] ATLAS Collaboration, G. Aad et al., *Improved luminosity determination in pp collisions at $\sqrt{s}$ = 7 TeV using the ATLAS detector at the LHC*, Eur.Phys.J. **C73** (2013) 2518, arXiv:1302.4393 [hep-ex].

[14] ATLAS Collaboration, G. Aad et al., *The ATLAS Experiment at the CERN Large Hadron Collider*, JINST **3** (2008) S08003.

[15] ATLAS Collaboration, G. Aad et al., *Observation and measurement of Higgs boson decays to WW^* with the ATLAS detector*, arXiv:1412.2641 [hep-ex].

[16] ATLAS Collaboration, G. Aad et al., *Evidence for the Higgs-boson Yukawa coupling to tau leptons with the ATLAS detector*, arXiv:1501.04943 [hep-ex].

[17] ATLAS Collaboration, G. Aad et al., *Search for the $b\bar{b}$ decay of the Standard Model Higgs boson in associated $(W/Z)H$ production with the ATLAS detector*, JHEP **1501** (2015) 069, arXiv:1409.6212 [hep-ex].

[18] ATLAS Collaboration, G. Aad et al., *Evidence for the spin-0 nature of the Higgs boson using ATLAS data*, Phys.Lett. **B726** (2013) 120–144, arXiv:1307.1432 [hep-ex].

[19] ATLAS Collaboration, *Study of the spin and parity of the Higgs boson in HVV decays with the ATLAS detector*, ATLAS-CONF-2015-008, 2015. http://cds.cern.ch/record/2002414.

[20] M. Drees, R. Godbole, and P. Roy, *Theory and Phenomenology of Sparticles*. World Scientific Publishing Company, 2005. http://www.amazon.com/Theory-Phenomenology-Sparticles-Four-Dimensional-Supersymmetry/dp/9812565310.

[21] I. Aitchison, *Supersymmetry in Particle Physics*. Cambridge University Press, 2007. http://www.cambridge.org/us/academic/subjects/physics/particle-physics-and-nuclear-physics/supersymmetry-particle-physics-elementary-introduction.

[22] ATLAS Collaboration, ATLAS Supersymmetry group public results. https://twiki.cern.ch/twiki/bin/view/AtlasPublic/SupersymmetryPublicResults.

[23] ATLAS Collaboration, ATLAS Exotics group public results. https://twiki.cern.ch/twiki/bin/view/AtlasPublic/ExoticsPublicResults.

[24] ATLAS Collaboration, G. Aad et al., *Observation of a Centrality-Dependent Dijet Asymmetry in Lead-Lead Collisions at $\sqrt{s_{NN}} = 2.77$ TeV with the ATLAS Detector at the LHC*, Phys.Rev.Lett. **105** (2010) 252303, arXiv:1011.6182 [hep-ex].

[25] ATLAS Collaboration, G. Aad et al., *Measurement of the centrality and pseudorapidity dependence of the integrated elliptic flow in lead-lead collisions at $\sqrt{s_{\rm NN}} = 2.76$ TeV with the ATLAS detector*, Eur.Phys.J. **C74** (2014) no. 8, 2982, arXiv:1405.3936 [hep-ex].

[26] ATLAS Collaboration, G. Aad et al., *Measurement of the centrality dependence of J/ψ yields and observation of Z production in lead-lead collisions with the ATLAS detector at the LHC*, Phys.Lett. **B697** (2011) 294–312, arXiv:1012.5419 [hep-ex].

[27] ATLAS Collaboration, G. Aad et al., *Measurement of inclusive jet charged-particle fragmentation functions in Pb+Pb collisions at* $\sqrt{s_{NN}} = 2.76$ *TeV with the ATLAS detector*, Phys.Lett. **B739** (2014) 320–342, arXiv:1406.2979 [hep-ex].

[28] ATLAS Collaboration, ATLAS public standalone plots. http://www.atlas.ch/photos/index.html.

[29] ATLAS Collaboration, *ATLAS liquid-argon calorimeter: Technical Design Report*, CERN-LHCC-96-041, 1996. http://cds.cern.ch/record/331061.

[30] ATLAS Collaboration, *ATLAS tile calorimeter: Technical Design Report*, CERN-LHCC-96-042, 1996. http://cds.cern.ch/record/331062.

[31] ATLAS Collaboration, G. Aad et al., *Readiness of the ATLAS Tile Calorimeter for LHC collisions*, Eur.Phys.J. **C70** (2010) 1193–1236, arXiv:1007.5423 [physics.ins-det].

[32] Fullana, E. and others, *Optimal Filtering in the ATLAS Hadronic Tile Calorimeter*, ATL-TILECAL-2005-001, ATL-COM-TILECAL-2005-001, CERN-ATL-TILECAL-2005-001, 2005. https://cds.cern.ch/record/816152.

[33] ATLAS Collaboration, G. Aad et al., *The ATLAS Simulation Infrastructure*, Eur.Phys.J. **C70** (2010) 823–874, arXiv:1005.4568 [physics.ins-det].

[34] GEANT4 Collaboration, S. Agostinelli et al., *GEANT4: A Simulation toolkit*, Nucl.Instrum.Meth. **A506** (2003) 250–303.

[35] T. Sjostrand, S. Mrenna, and P. Z. Skands, *PYTHIA 6.4 Physics and Manual*, JHEP **0605** (2006) 026, arXiv:hep-ph/0603175 [hep-ph].

[36] T. Sjostrand, S. Mrenna, and P. Z. Skands, *A Brief Introduction to PYTHIA 8.1*, Comput.Phys.Commun. **178** (2008) 852–867, arXiv:0710.3820 [hep-ph].

[37] M. Bahr, S. Gieseke, M. Gigg, D. Grellscheid, K. Hamilton, et al., *Herwig++ Physics and Manual*, Eur.Phys.J. **C58** (2008) 639–707, arXiv:0803.0883 [hep-ph].

[38] K. Arnold, L. d'Errico, S. Gieseke, D. Grellscheid, K. Hamilton, et al., *Herwig++ 2.6 Release Note*, arXiv:1205.4902 [hep-ph].

[39] S. Alioli, P. Nason, C. Oleari, and E. Re, *A general framework for implementing NLO calculations in shower Monte Carlo programs: the POWHEG BOX*, JHEP **1006** (2010) 043, arXiv:1002.2581 [hep-ph].

[40] S. Frixione, P. Nason, and C. Oleari, *Matching NLO QCD computations with Parton Shower simulations: the POWHEG method*, JHEP **0711** (2007) 070, arXiv:0709.2092 [hep-ph].

[41] P. Nason, *A New method for combining NLO QCD with shower Monte Carlo algorithms*, JHEP **0411** (2004) 040, arXiv:hep-ph/0409146 [hep-ph].

[42] ATLAS Collaboration, G. Aad et al., *Jet energy measurement and its systematic uncertainty in proton-proton collisions at $\sqrt{s} = 7$ TeV with the ATLAS detector*, Eur.Phys.J. **C75** (2015) no. 1, 17, arXiv:1406.0076 [hep-ex].

[43] Lampl, W. and others, *Calorimeter Clustering Algorithms: Description and Performance*, ATL-LARG-PUB-2008-002, ATL-COM-LARG-2008-003, 2008. http://cds.cern.ch/record/1099735.

[44] ATLAS Collaboration, G. Aad et al., *Jet energy measurement with the ATLAS detector in proton-proton collisions at $\sqrt{s} = 7$ TeV*, Eur.Phys.J. **C73** (2013) 2304, arXiv:1112.6426 [hep-ex].

[45] Barillari, T. and others, *Local Hadronic Calibration*, ATL-LARG-PUB-2009-001-2, ATL-COM-LARG-2008-006, 2008. http://cds.cern.ch/record/1112035.

[46] M. Cacciari, G. P. Salam, and G. Soyez, *FastJet User Manual*, Eur.Phys.J. **C72** (2012) 1896, arXiv:1111.6097 [hep-ph].

[47] ATLAS Collaboration, 2011 jet energy resolution twiki, 2012. https://twiki.cern.ch/twiki/bin/view/AtlasPublic/JetEtmissApproved2013Jer2011.

[48] ATLAS Collaboration, G. Aad et al., *Study of Jet Shapes in Inclusive Jet Production in pp Collisions at $\sqrt{s} = 7$ TeV using the ATLAS Detector*, Phys.Rev. **D83** (2011) 052003, arXiv:1101.0070 [hep-ex].

[49] ATLAS Collaboration, *Data-Quality Requirements and Event Cleaning for Jets and Missing Transverse Energy Reconstruction with the ATLAS Detector in Proton-Proton Collisions at a Center-of-Mass Energy of sqrts = 7 TeV*, ATLAS-CONF-2010-038, ATLAS-COM-CONF-2010-038, 2010. http://cds.cern.ch/record/1277678.

[50] ATLAS Collaboration, *Selection of jets produced in proton-proton collisions with the ATLAS detector using 2011 data*, ATLAS-CONF-2012-020, ATLAS-COM-CONF-2012-018, 2012. http://cds.cern.ch/record/1430034.

[51] P. Z. Skands, *Tuning Monte Carlo Generators: The Perugia Tunes*, Phys.Rev. **D82** (2010) 074018, arXiv:1005.3457 [hep-ph].

[52] CTEQ Collaboration Collaboration, H. Lai et al., *Global QCD analysis of parton structure of the nucleon: CTEQ5 parton distributions*, Eur.Phys.J. **C12** (2000) 375–392, arXiv:hep-ph/9903282 [hep-ph].

[53] T. Sjostrand and P. Z. Skands, *Transverse-momentum-ordered showers and interleaved multiple interactions*, Eur.Phys.J. **C39** (2005) 129–154, arXiv:hep-ph/0408302 [hep-ph].

[54] ALICE Collaboration, B. Abelev et al., *Measurement of the inclusive differential jet cross section in pp collisions at* $\sqrt{s} = 2.76$ *TeV*, Phys.Lett. **B722** (2013) 262–272, arXiv:1301.3475 [nucl-ex].

[55] CMS Collaboration, S. Chatrchyan et al., *Measurements of differential jet cross sections in proton-proton collisions at* $\sqrt{s} = 7$ *TeV with the CMS detector*, Phys.Rev. **D87** (2013) no. 11, 112002, arXiv:1212.6660 [hep-ex].

[56] CMS Collaboration, *Measurement of the double-differential inclusive jet cross section at sqrt(s) = 8 TeV with the CMS detector*, CMS-PAS-SMP-12-012, 2013. https://cdsweb.cern.ch/record/1547589.

[57] ATLAS Collaboration, G. Aad et al., *Measurement of inclusive jet and dijet production in pp collisions at* $\sqrt{s} = 7$ *TeV using the ATLAS detector*, Phys.Rev. **D86** (2012) 014022, arXiv:1112.6297 [hep-ex].

[58] ATLAS Collaboration, G. Aad et al., *Measurement of the inclusive jet cross section in pp collisions at sqrt(s)=2.76 TeV and comparison to the inclusive jet cross section at sqrt(s)=7 TeV using the ATLAS detector*, Eur.Phys.J. **C73** (2013) 2509, arXiv:1304.4739 [hep-ex].

[59] ATLAS Collaboration, G. Aad et al., *Measurement of the inclusive jet cross-section in proton-proton collisions at* $\sqrt{s} = 7$ *TeV using 4.5* fb^{-1} *of data with the ATLAS detector*, JHEP **1502** (2015) 153, arXiv:1410.8857 [hep-ex].

[60] Z. Nagy, *Next-to-leading order calculation of three jet observables in hadron hadron collision*, Phys.Rev. **D68** (2003) 094002, arXiv:hep-ph/0307268 [hep-ph].

[61] T. Carli, D. Clements, A. Cooper-Sarkar, C. Gwenlan, G. P. Salam, et al., *A posteriori inclusion of parton density functions in NLO QCD final-state calculations at hadron colliders: The APPLGRID Project*, Eur.Phys.J. **C66** (2010) 503–524, arXiv:0911.2985 [hep-ph].

[62] H.-L. Lai, M. Guzzi, J. Huston, Z. Li, P. M. Nadolsky, et al., *New parton distributions for collider physics*, Phys.Rev. **D82** (2010) 074024, arXiv:1007.2241 [hep-ph].

[63] A. Martin, W. Stirling, R. Thorne, and G. Watt, *Parton distributions for the LHC*, Eur.Phys.J. **C63** (2009) 189–285, arXiv:0901.0002 [hep-ph].

[64] R. D. Ball, L. Del Debbio, S. Forte, A. Guffanti, J. I. Latorre, et al., *A first unbiased global NLO determination of parton distributions and their uncertainties*, Nucl.Phys. **B838** (2010) 136–206, arXiv:1002.4407 [hep-ph].

[65] S. Forte, E. Laenen, P. Nason, and J. Rojo, *Heavy quarks in deep-inelastic scattering*, Nucl.Phys. **B834** (2010) 116–162, arXiv:1001.2312 [hep-ph].

[66] S. Alekhin, J. Blumlein, and S. Moch, *Parton Distribution Functions and Benchmark Cross Sections at NNLO*, Phys.Rev. **D86** (2012) 054009, arXiv:1202.2281 [hep-ph].

[67] H1 and ZEUS Collaboration, *HERAPDF 1.5*, H1prelim-10-142, ZEUS-prel-10-018. http://www.desy.de/h1zeus/combined_results/index.php?do=proton_structure.

[68] S. Dittmaier, A. Huss, and C. Speckner, *Weak radiative corrections to dijet production at hadron colliders*, JHEP **1211** (2012) 095, arXiv:1210.0438 [hep-ph].

[69] M. Botje, J. Butterworth, A. Cooper-Sarkar, A. de Roeck, J. Feltesse, et al., *The PDF4LHC Working Group Interim Recommendations*, arXiv:1101.0538 [hep-ph].

[70] ATLAS Collaboration, *ATLAS tunes of PYTHIA 6 and PYTHIA 8 for MC11*, ATL-PHYS-PUB-2011-009, 2011. http://cdsweb.cern.ch/record/1363300.

[71] R. Corke and T. Sjostrand, *Interleaved Parton Showers and Tuning Prospects*, JHEP **1103** (2011) 032, arXiv:1011.1759 [hep-ph].

[72] ATLAS Collaboration, *Summary of ATLAS Pythia 8 tunes*, ATL-PHYS-PUB-2012-003, ATL-COM-PHYS-2012-738, 2012. http://cds.cern.ch/record/1474107.

[73] S. Gieseke, C. Rohr, and A. Siodmok, *Colour reconnections in Herwig++*, Eur.Phys.J. **C72** (2012) 2225, arXiv:1206.0041 [hep-ph].

[74] ATLAS informal jet physics meeting, 10.4.2015. https://indico.cern.ch/event/384140/.

[75] Pythia 6.428 update notes. https://www.hepforge.org/archive/pythia6/update_notes-6.4.28.txt.

[76] P. Nason and C. Oleari, *Generation cuts and Born suppression in POWHEG*, arXiv:1303.3922 [hep-ph].

[77] S. Alioli, K. Hamilton, P. Nason, C. Oleari, and E. Re, *Jet pair production in POWHEG*, JHEP **1104** (2011) 081, arXiv:1012.3380 [hep-ph].

[78] A. Hocker and V. Kartvelishvili, *SVD approach to data unfolding*, Nucl.Instrum.Meth. **A372** (1996) 469–481, arXiv:hep-ph/9509307 [hep-ph].

[79] G. D'Agostini, *A Multidimensional unfolding method based on Bayes' theorem*, Nucl.Instrum.Meth. **A362** (1995) 487–498.

[80] G. D'Agostini, *Improved Iterative Bayesian unfolding*, arXiv:1010.0632 [physics.data-an].

[81] B. Malaescu, *An Iterative, dynamically stabilized method of data unfolding*, arXiv:0907.3791 [physics.data-an].

[82] Malaescu, B., *An Iterative, Dynamically Stabilized (IDS) Method of Data Unfolding*, Proceedings of PHYSTAT2011, CERN Yellow Report 2011-006, 2011. arXiv:1106.3107 [physics.data-an], https://cdsweb.cern.ch/record/1306523.

[83] ATLAS Collaboration, *Practical considerations for unfolding*, ATL-COM-PHYS-2014-277, 2014. https://cds.cern.ch/record/1694351?ln=en.

[84] T. Hastie, R. Tibshirani, and J. Friedman, *The Elements of Statistical Learning*. Springer, 2001. http://statweb.stanford.edu/~tibs/ElemStatLearn/.

[85] ATLAS Collaboration, G. Aad et al., *Jet energy resolution in proton-proton collisions at $\sqrt{s} = 7$ TeV recorded in 2010 with the ATLAS detector*, Eur. Phys. J. **C 73** (2013) 2306, arXiv:1210.6210 [hep-ex].

[86] Baker, S. and others, *Measurement of inclusive jet and dijet production in pp collisions at $\sqrt{s}$=7 TeV using the ATLAS detector*, ATL-COM-PHYS-2011-738, 2011. https://cds.cern.ch/record/1360174.

[87] Begel, M. and others, *Azimuthal Decorrelations in Dijet Events at sqrts = 7 TeV*, ATL-PHYS-INT-2010-110, 2010. https://cds.cern.ch/record/1290956.

[88] Carli, T. and others, *Measurement of inclusive jet production in pp collisions at $\sqrt{s} = 7$ TeV using the ATLAS detector (Supporting Documentation)*, ATL-COM-PHYS-2013-1390, 2013. https://cds.cern.ch/record/1605468.

[89] Boelaert, N. and others, *Measurement of high mass dijet production in pp collisions at $\sqrt{s} = 7$ TeV using the ATLAS detector (Supporting Documentation)*, ATL-COM-PHYS-2012-1250, 2012. https://cds.cern.ch/record/1473882.

List of Tables

List of Abbreviations

ADC analog-to-digital converter. 23

DAQ Data Acquisition. 25

digitizer digitizer board. 23

EB extended barrel. 23, 41

EF event filter. 24, 25

EM electromagnetic. 18, 20–22, 27, 28, 34–36, 42, 53, 82, 83

EW electroweak. 48, 50, 85, 86, 93

FCal Forward calorimeter. 20, 22, 23

FEB front-end board. 21, 39, 40, 53

FSR final state radiation. 36

HEC Hadronic End-Caps. 20, 22

HEP High-Energy Physics. 19

HG high-gain. 23

HV High Voltage. 23, 39

ID inner detector. 18, 19, 36

IDS Iterative, dynamically stabilized (method of data unfolding). 55, 56, 58–63

IF interface. 24, 39

IR infrared. 7

ISR initial state radiation. 36–39

ITC Intermediate Tile Calorimeter. 23

JAR jet angular resolution. 63, 72, 74

JER jet energy resolution. 28, 63, 68, 69, 71, 72, 74–77

JES jet energy scale. 28, 31, 32, 63–71, 75–77

KLN Kinoshita-Lee-Nauenberg. 13

L1 level 1 (trigger). 24, 25

L2 level 2 (trigger). 24, 25

LAr liquid argon. 21, 39, 40, 53, 57, 58, 67, 73, 74

LB long barrel. 23, 41

LCW local cluster weighting. 27, 28, 30, 42, 43

LG low-gain. 23

LHC Large Hadron Collider. 3, 47, 84

LL leading-logarithm. 11, 50

LO leading-order. 8, 36, 48, 50

lumiblock luminosity block. 17, 26, 78

LVPS Low Voltage Power Supply. 23, 33, 39

MC Monte Carlo. 25, 26, 29–32, 34, 36–40, 42, 44, 45, 48, 50, 53–56, 58–62, 65, 68, 69, 71–76, 78–81, 83, 93, 103, 109, 110

NLO next-to-leading-order. 8, 9, 47, 48, 50, 85, 86, 93

NNLL next-to-next-to-leading logarithm. 12, 85

NP non-perturbative. 48–52, 93

NP nuisance parameter. 65

PDF parton distribution function. 3, 5, 10–12, 47, 48, 50, 51, 85, 86, 89, 93

PMT photomultiplier tube. 23

pQCD perturbative quantum chromodynamics. 5

QCD quantum chromodynamics. 1, 3, 5–12, 14, 50, 85, 86, 93

RMS root mean square. 65

ROB Read-Out Buffer. 24

ROD Read-Out Driver. 24

RoI Region of Interest. 25

ROL Read-Out Link. 24

SCT semiconductor tracker. 19, 20

SM Standard Model. 3, 5, 18

SVD Singular Value Decomposition. 55, 60, 61

TileCal Tile Calorimeter. 20, 21, 23, 33–35, 39–41, 43–45, 53, 76, 78, 79, 82, 93, 103, 109, 110

TM transfer matrix. 56–59, 61, 69, 71, 72, 74, 80, 81

topocluster topological cluster. 1, 27–29, 34, 42–45, 47, 72

TRT transition radiation tracker. 19, 20

UE Underlying Event. 5, 13, 16, 29, 36, 48, 50

UV ultraviolet. 1, 7, 8

A. Closer look at the TileCal module LBA11

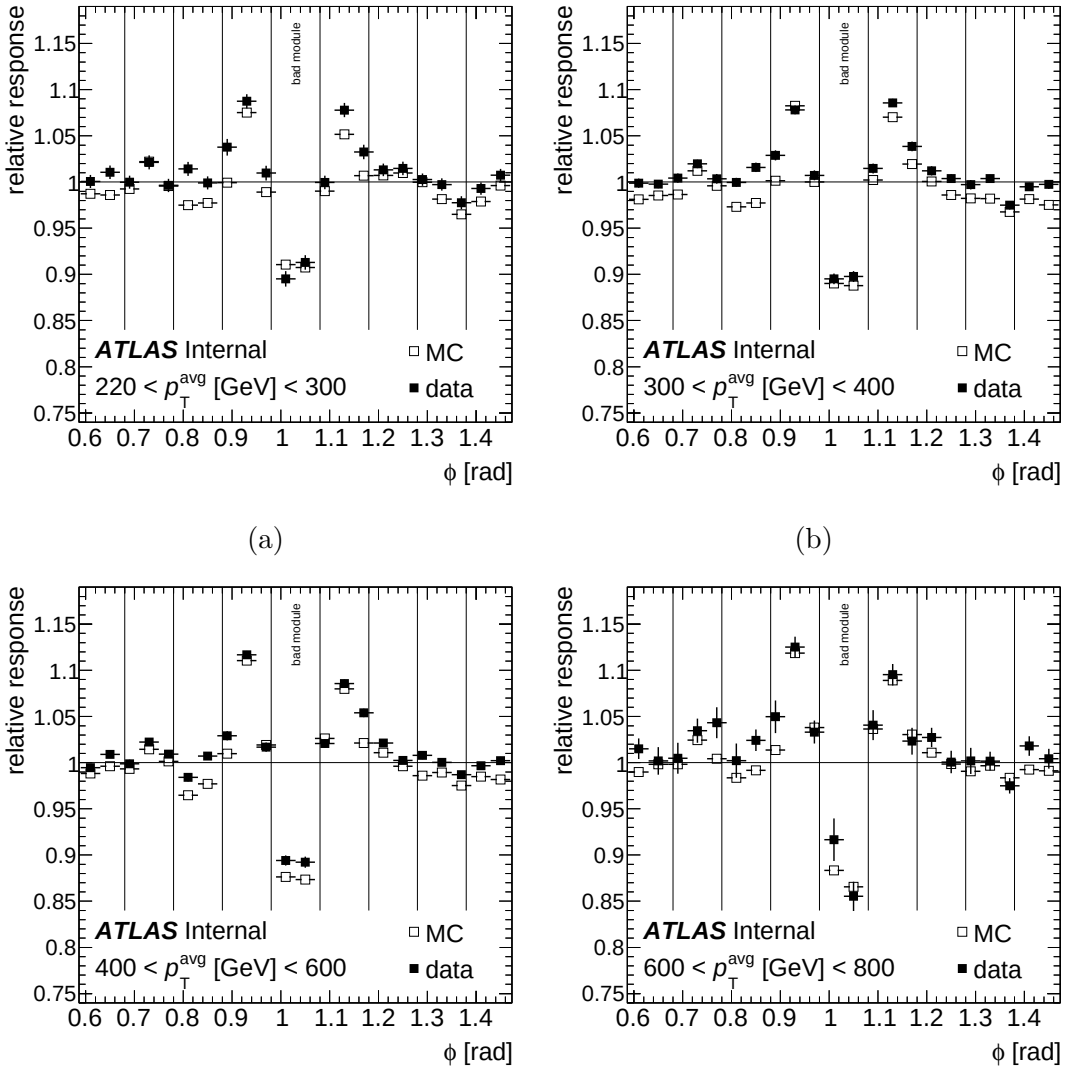

Figure A.1: The relative jet p_{T} response measured in dijet events with one jet falling into an operational calorimeter region and the other jet probing the vicinity of one chosen non-operational TileCal module. $\mathrm{BCH}_{\mathrm{cor,\,cell}}$ is used to correct the probe jet energy. Four different $p_{\mathrm{T}}^{\mathrm{avg}}$ bins are shown for both MC and data. The vertical lines represent the TileCal module edges. Jets are calibrated with the EM+JES scheme.

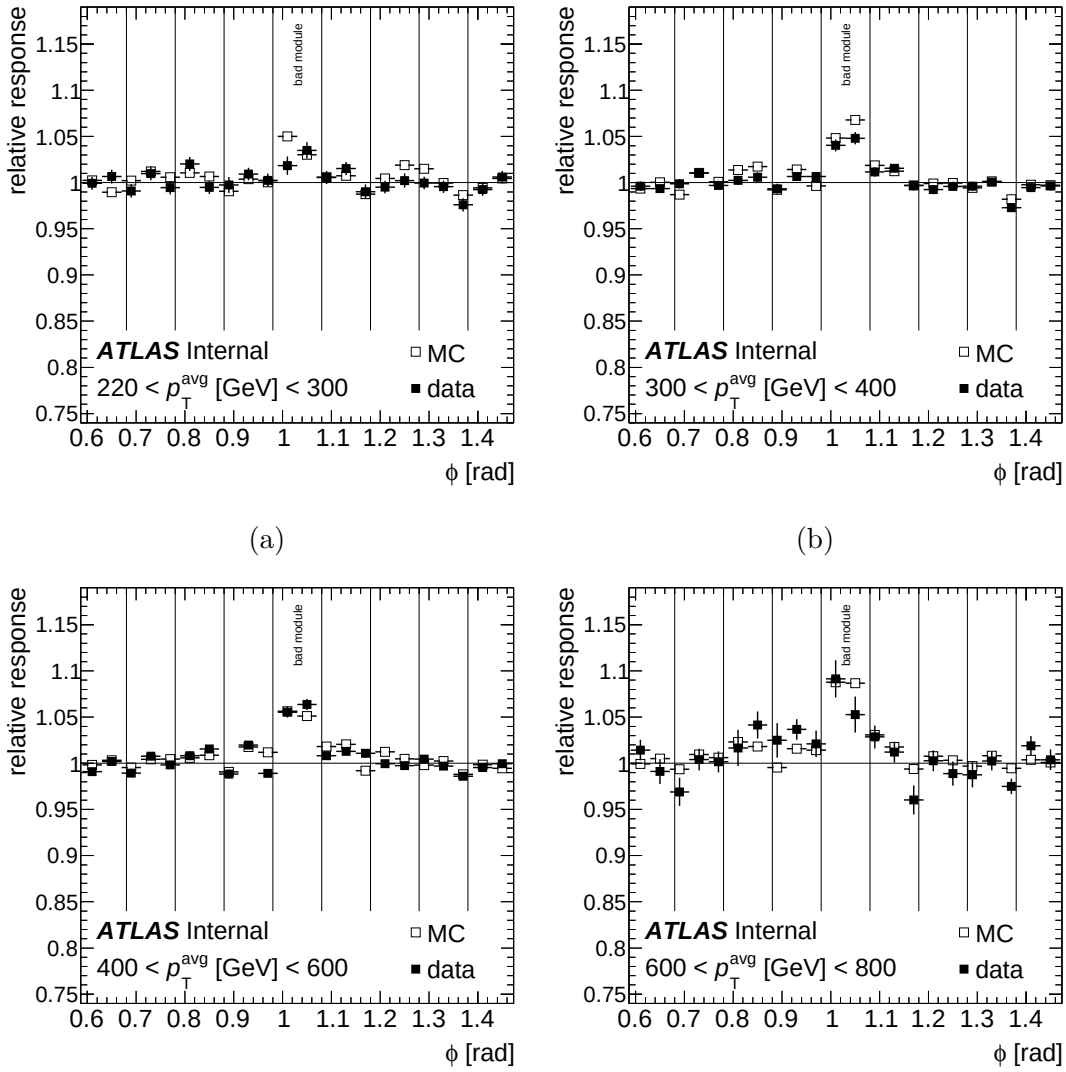

Figure A.2: The relative jet p_{T} response measured in dijet events with one jet falling into an operational calorimeter region and the other jet probing the vicinity of one chosen non-operational TileCal module. $\mathrm{BCH}_{\mathrm{cor,\,jet}}$ is used to correct the probe jet energy. Four different $p_{\mathrm{T}}^{\mathrm{avg}}$ bins are shown for both MC and data. The vertical lines represent the TileCal module edges. Jets are calibrated with the EM+JES scheme.